Density functional theory study of $LaMnO_3$ and its competing oxides: an insight into a prospective alkaline fuel cell cathode

Ehsan Aleem Ahmad
Department of Chemistry
Imperial College London

A thesis submitted for the degree of
Doctor of Philosophy

October 2013

Declaration of Originality

I hereby declare that this thesis is a presentation of my original research work and has not been submitted previously for a degree qualification or any other academic qualification at this University or any other institution of higher education. Wherever contributions of others are involved, every effort is made to indicate this, with due reference to literature and acknowledgements of collaborative research and discussions. The research work presented in this thesis was conducted under the guidance of Professor Nicholas M. Harrison and Professor Anthony Kucernak, both at the Imperial College London, London.

Ehsan Aleem Ahmad
October 2013

Declaration of Copyright

Abstract

$LaMnO_3$ is an inexpensive alternative to precious metals (e.g. platinum) as a catalyst for the oxygen reduction reaction (ORR) in alkaline fuel cells (AFCs). In fact, recent studies have shown that among a range of non-noble metal catalysts, $LaMnO_3$ provides the highest catalytic activity. However, further development of this catalyst is limited by the fact that very little is known about $LaMnO_3$ in the AFC environment. While it has been established that the bulk phase possesses an orthorhombic structure, it has not been possible to determine the structure of the surfaces or the sites active towards the ORR. In this work, therefore, periodic hybrid-exchange (B3LYP) density functional calculations are performed in order to understand the origins of the catalytic activity of $LaMnO_3$. The long term goal is to suggest strategies for optimising the activity of $LaMnO_3$ through control of its crystallite morphology.

Initially, the phase stability of $LaMnO_3$ with respect to its competing (La, Mn) oxides is determined by accurate calculation of the Gibbs formation energies of each compound (1.6% mean error). The accuracy achieved is higher than in previous literature, validating the methodology adopted and the reliability of the chemical potentials determined to limit the stability of the bulk and surfaces of $LaMnO_3$. Having determined the ground state of each Mn oxide it was possible to simulate electron energy-loss spectroscopy (EELS) for Mn in different valence states and local environments. The simulated EELS demonstrated that it is possible to identify its oxidation state and local coordination (i.e. the surface structure) on $LaMnO_3$ surface terminations, based on the shift and shape of predicted L_3 edges, which correlate well with measured EEL spectra.

Calculations of the low-index, stoichiometric and non-polar surfaces of $LaMnO_3$ were then performed in order to predict the equilibrium crystal morphology. For each low energy surface the adsorption sites were also identified. The energetics of the surfaces are rationalised in terms of the cleavage of Jahn-Teller distorted Mn-O bonds, the compensation of undercoordination for ions in the terminating layer and relaxation

effects.

Finally the adsorption sites identified are investigated by adsorption of molecular O_2. The binding energies, adsorbate structure and charge transfer are analysed to predict the reactivity of each site. Results indicate that Jahn-Teller distortion and the coordination of Mn sites modulate the binding strength of O_2.

The main results presented are the crystallite morphology, the identification of surface reaction sites and the chemical characterisation of those sites. This is a theoretical characterisation of the $LaMnO_3$ catalyst providing detailed atomistic information that has not been possible to deduce from experiment.

Acknowledgements

First and foremost I would like to thank my supervisors, Prof. Nicholas Harrison and Prof. Anthony Kucernak, for providing me with the opportunity to study for a PhD. They gave me flexibility and freedom in my studies but were always there for guidance and support when needed. I owe gratitude to Dr. Giuseppe Mallia for his mentoring, patience and friendship over the past four years. I would also like to thank Dr. Leandro Liborio and Dr. Denis Kramer for many fruitful discussions on *ab initio* thermodynamics, and Dr. Vaso Tileli for providing her expertise on electron energy-loss spectroscopy.

A special thanks goes to my colleagues and friends in Prof. Harrison's theory group; Romi, Monica, Fred, Ross and Ruth, for the many chats, scientific discussions and fun over lunch and coffee. I would also like to mention other friends in the Thomas Young Centre and outside of academia; Michele for training with me, Jing and Leo for the laughs, Evgeniy for being a joker and the table tennis, Luke for the football, Sophie for her patience, and Luca, Basmah and Jazz for being good neighbours. The last four years in London went by so quickly having you all around.

Finally, my gratitude goes to my family, especially my mother, for their love, care and patience.

My thanks also goes to the EPSRC and STFC for funding my PhD and I would like to acknowledge that this work made use of the high performance computing facilities of Imperial College London and - via membership of the UK's HPC Materials Chemistry Consortium funded by EPSRC (EP/F067496) - of HECToR, the UK's national high-performance computing service, which is provided by UoE HPCx Ltd at the University of Edinburgh, Cray Inc and NAG Ltd, and funded by the Office of Science and Technology through EPSRC's High End Computing Programme.

List of Publications

- E. A. Ahmad, L. Liborio, D. Kramer, G. Mallia, A. R. Kucernak, and N. M. Harrison, Thermodynamic stability of $LaMnO_3$ and its competing oxides: A hybrid density functional study of an alkaline fuel cell catalyst, *Phys. Rev. B* **84** 085137 2011.

- E. A. Ahmad, G. Mallia, D. Kramer, V. Tileli, A. R. Kucernak, and N. M. Harrison, Comment on "2D Atomic Mapping of Oxidation States in Transition Metal Oxides by Scanning Transmission Electron Microscopy and Electron Energy-Loss Spectroscopy", *Phys. Rev. Lett.* **108** 259701 2012.

- E. A. Ahmad, G. Mallia, D. Kramer, A. R. Kucernak, and N. M. Harrison, The stability of $LaMnO_3$ surfaces: a hybrid exchange density functional theory study of an alkaline fuel cell catalyst, *J. Mater. Chem. A* **1** 37 2013

- E. A. Ahmad, G. Mallia, D. Kramer, A. R. Kucernak, and N. M. Harrison, O_2 adsorption on orthorhombic $LaMnO_3$: a hybrid exchange density functional study of an alkaline fuel cell catalyst *In Preparation*

Contents

List of Figures

List of Tables

1

Introduction

In recent years, there has been a growing interest in the use of perovskites for application in fuel cells, particularly in solid oxide fuel cells (SOFCs) [1], where they have been implemented as anode, cathode [2] and electrolyte [3] materials due to their catalytic and ion conducting properties. Some of the latest work has involved exploring their use as cathode catalysts in alkaline fuel cells (AFCs) [4–7], where high activity has been reported for the oxygen reduction reaction (ORR).

Perovskites are a highly flexible class of materials, which express varying degrees of catalytic activity depending on the compositional atoms and the degree to which they are substituted. The range of activity from various perovskites can be found in recent studies [6, 7]. Understanding how the compositional (and resulting structural) changes of perovskites are correlated to catalytic activity is one of the key long term objectives of the current work; using theoretical modelling and simulations the properties of perovskites are to be calculated and, in conjunction with experiments, a method of screening for the catalytic properties of perovskites is pursued alongside an understanding of the structural features required to obtain them. Thus, as an outcome of this research, it is not unreasonable to expect that the development of AFC catalysts can be accelerated by establishing a route for catalytic material design via computational analysis.

In this chapter, the context for catalyst development in AFCs is introduced and a short review of literature relating to the materials concerned is given. This begins with the motivations for the use of perovskites in fuel cells, followed by a discussion of their application in AFCs and an overview of the methods by which they can be synthesised and characterised. A short review of the properties of the perovskite studied in this work is also provided, along with its competing oxides. Lastly, a plan for the research

programme will be briefly outlined.

1.1 Background

A major concern of the international community is the provision of energy to a demand that is always increasing, under the constraints of a limited fossil fuel supply. The development of energy generation methods that are not limited by fuel supply has, therefore, been widely investigated for many years. The urgency of such research has further increased since the environmental issues associated with fossil fuel combustion (global warming, ocean acidification, smog, low air quality) have become well recognised [8, 9].

One solution to this energy challenge is the hydrogen powered fuel cell. This solution operates on a potentially limitless supply of fuel through, for example, solar water splitting, while only producing water as a by-product of the electrochemical reaction that generates electricity (Fig. 1.1) [10].

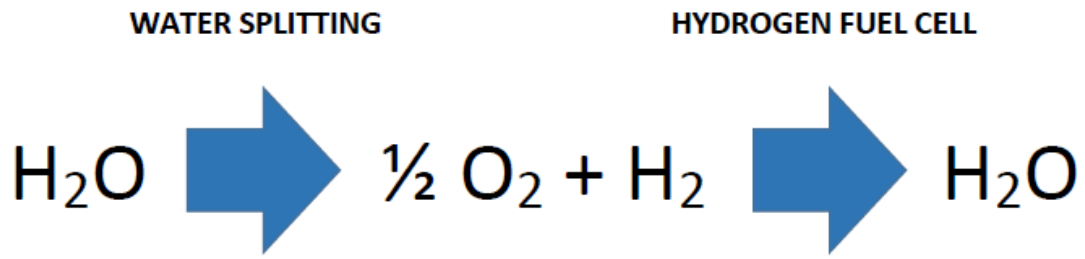

Figure 1.1: The water splitting and hydrogen fuel cell reactions.

Hydrogen fuel cells can be used for a variety of applications, but perhaps their biggest role is in vehicles, which currently use fossil fuels via the internal combustion engine. Commercialisation of fuel cells for application in the automotive industry, however, faces a big obstacle; the high cost of Pt that is used to catalyse the fuel cell reaction [11]. In order to overcome this, the focus of most research in this field has centered on how to retain high performance in the fuel cell while reducing the loading of Pt [11].

The fuel cell that is typically adopted for automotive applications is known as the polymer electrolyte membrane fuel cell (PEMFC). An alternative approach to reducing the catalyst cost, which has gained traction only in the last few years, involves the use of alkaline fuel cells (AFCs). These fuel cells, which also use hydrogen fuel, are able

to operate at reasonable performance levels without the use of expensive noble metal catalysts (such as Pt) [6]. This is attributed to their alkaline electrolyte, which makes the reduction of oxygen on the cathode for the fuel cell reaction (Fig. 1.1), more facile than in the acidic environment of a conventional automotive fuel cell (PEMFC).

A range of noble metal alternatives that are active catalysts for the cathode side oxygen reduction reaction (ORR) in the AFC environment are known as perovskites [6, 7]. For many years perovskites have been the focus of research in different type of fuel cell, the solid oxide fuel cell (SOFC), which they are more commonly associated with. Although both types of fuel cell are capable of converting hydrogen and oxygen gas into water to give electricity, the processes occur slightly differently due to the nature of the electrolytes and the considerably different operating temperatures. SOFCs operate in the range of 600-1000 °C, while modern AFCs generally operate at much lower temperatures; a range of 25-70°C is common [2, 6].

It is due to the elevated operating temperature of SOFCs that the use of perovskites has been so successful in the past, as at these temperatures various perovskites become highly active towards the fuel cell reactions. SOFCs are actually able to generate electricity from several types of fuel, such as hydrogen, methane and many other hydrocarbons. This fuel source diversity is made possible due to the high operating temperature, which provides better catalytic conditions and tolerance for poisoning from contaminants and waste products [3].

In addition to the operating conditions of the SOFC, the characteristics of the electrolyte used are also quite different from an AFC. The electrolyte must be a material able to conduct oxygen anions (O^{2-}) in order to carry the charge for the fuel cell reaction, while also being an electrical insulator so that the system does not short circuit. The SOFC reaction proceeds when oxygen anions are formed at the cathode (oxygen molecules gain electrons), before being transported through the electrolyte to the anode, where they react with hydrogen and release electrons to form water. As in all fuel cells, the electrons are routed through an external circuit to generate electricity. The SOFC reactions are summarised by Eqs. 1.1 - 1.3.

$$\text{SOFC Cathode} : \frac{1}{2}O_2 + 2e^- \rightarrow O^{2-} \tag{1.1}$$

$$\text{SOFC Anode} : H_2 + O^{2-} \rightarrow H_2O + 2e^- \tag{1.2}$$

$$\text{Overall SOFC reaction} : H_2 + \frac{1}{2}O_2 \rightarrow H_2O \tag{1.3}$$

Perovskites generally do not show significant catalytic activity for the fuel cell ORR at lower temperatures, however, in the alkaline environment of the AFC electrolyte, their activity can be competitive with conventional noble metal catalysts [6]. AFCs have a different structure to SOFCs, which is illustrated in Fig. 1.2.

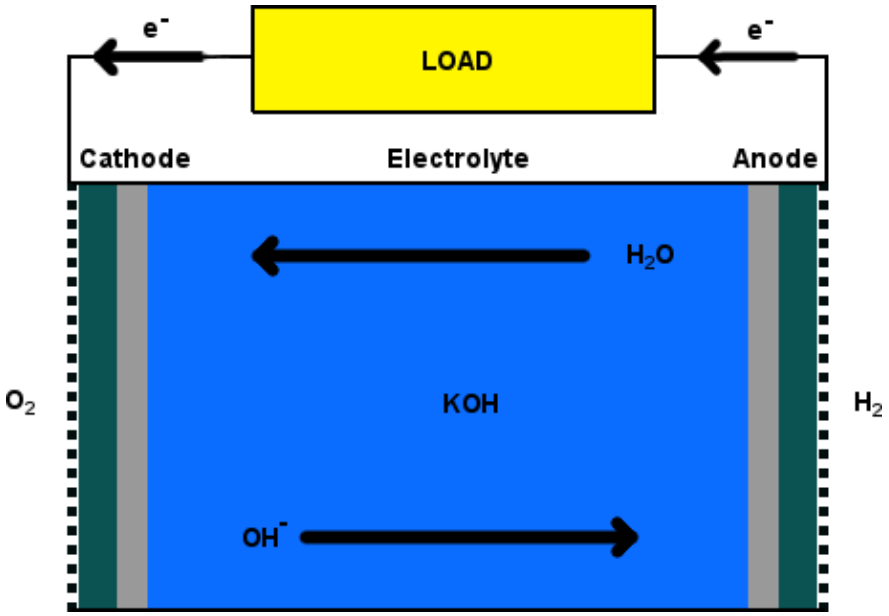

Figure 1.2: Schematic of an alkaline fuel cell.

The electrolyte for this type of fuel cell is typically an aqueous alkaline solution such as potassium hydroxide (KOH) that is retained in a porous matrix. With the growing interest in AFCs in recent years, various hydroxide (OH^-) conducting solid polymer electrolytes have also been developed, which allow for the construction of more compact fuel cells [12–14].

The AFC electrodes are a composite structure made up of a backing layer, gas diffusion layer and a catalyst layer (Fig. 1.3). The composite structure of the AFC electrode must allow for high permeability of reactant gases to the active portion of the catalyst layer, while also remaining robust, electrically conductive and resistant to corrosion. With regards to the study of perovskite catalysts in this work, we are mainly concerned with the active portion of the catalyst layer, i.e. the active layer.

This layer, isolated in Fig. 1.4, exists in the boundary between the electrolyte and cathode (or anode) and is commonly made up of catalyst particles that are supported by larger particles of carbon black. The primary function of the carbon particles is to provide an electrical pathway for the current but they can also aid catalytic activ-

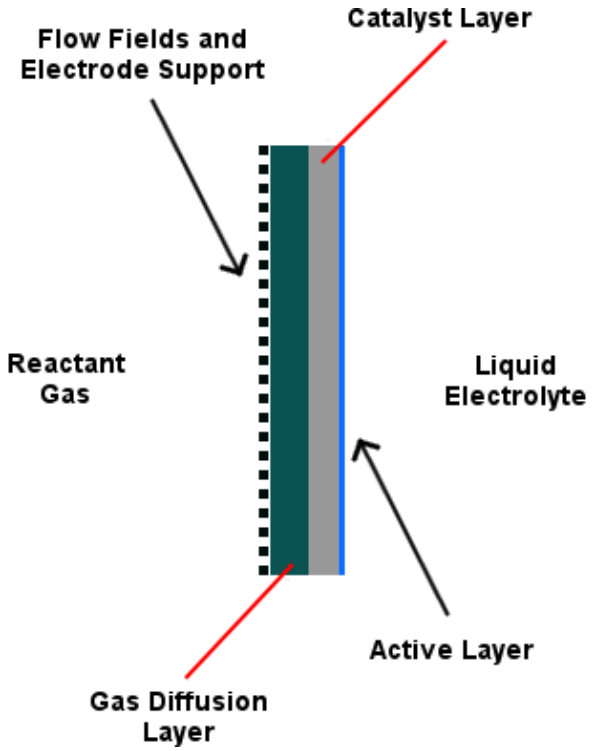

Figure 1.3: A typical composite electrode for an alkaline fuel cell.

ity. The mixture of particles can also be partially enclosed by polytetrafluoroethylene (PTFE) for binding and hydrophobicity [6]. The most crucial function of this layer is to provide a region, known as the three phase boundary, where the gaseous reactants, solid catalyst/support and ions in the aqueous electrolyte can meet in order for the fuel cell reactions to take place. A detailed example of the type of three phase boundaries that exist in AFCs is presented in Fig. 1.4.

Contrary to the O^{2-} anions of the SOFC, the AFC uses the aqueous OH^{-} ions in its alkaline electrolyte to carry charge. These ions move to the anode in order react with H_2 to form H_2O and release electrons. The electrons are directed through an external circuit (generating electricity) towards the cathode where they combine with O_2 and H_2O to reform OH^{-} ions and complete the electrochemical reaction. These AFC reactions are summarised by Eqs. 1.4 - 1.6.

$$\text{AFC Cathode} : O_2 + 2H_2O + 4e^{-} \rightarrow 4OH^{-} \tag{1.4}$$

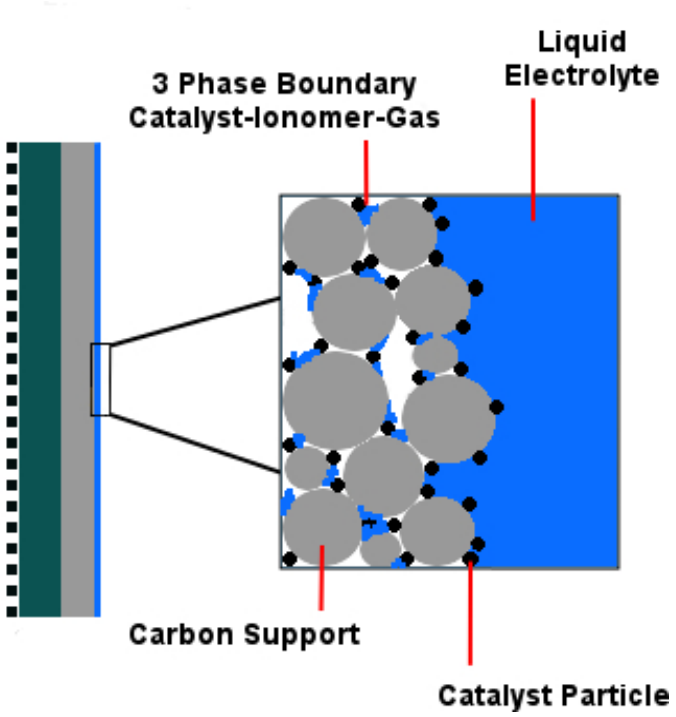

Figure 1.4: Detailed view of the active layer of an AFC electrode.

$$\text{AFC Anode} : 2H_2 + 4OH^- \rightarrow 4H_2O + 4e^- \tag{1.5}$$

$$\text{Overall AFC reaction} : O_2 + 2H_2 \rightarrow 2H_2O \tag{1.6}$$

Although the generic reactions that occur in the AFC system are well understood, there is not as much certainty with regards to reaction mechanism. Knowledge of the mechanism by which the ORR takes place is essential when investigating catalysts, as it allows us to evaluate them with respect to their binding of the various reactants and intermediates. In the past there have been two types of reaction pathways proposed for the ORR in alkaline media. The direct 4-electron pathway and the peroxide pathway. The direct pathway proceeds by the direct reduction of O_2 into OH^-, as demonstrated previously in Eq. 1.4. The peroxide pathway, on the other hand, involves the initial formation of hydroxide and peroxide (Eq. 1.7), followed by an additional step to form more hydroxide (Eq. 1.8) [15].

$$\text{Peroxide pathway} : O_2 + H_2O + 2e^- \rightarrow HO_2^- + OH^- \tag{1.7}$$

$$HO_2^- + H_2O + 2e^- \rightarrow 3OH^- \tag{1.8}$$

More recently, an ORR mechanism taking into account the binding of adsorbate species on a perovskite in the alkaline environment has also been proposed. This pathway is similar to the peroxide pathway but is divided into four steps, as shown in Fig. 1.5 [7]. The first and last steps are claimed to be rate-limiting, where the the binding strength of the transition metal to the intermediates determines if those steps will proceed or not.

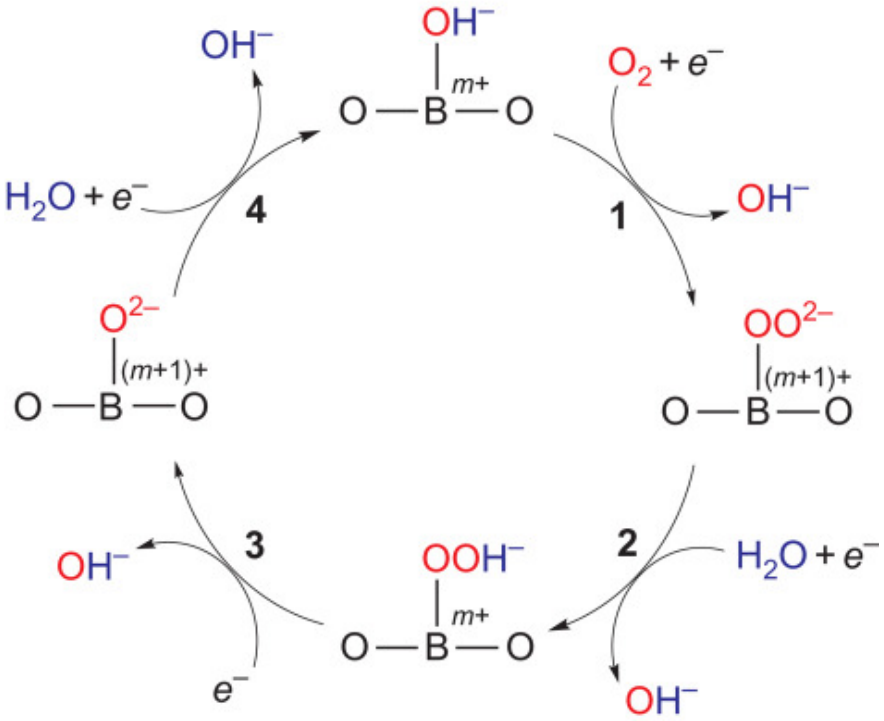

Figure 1.5: Steps of the ORR mechanism on a perovskite transition metal cation site: **1.** displacement of hydroxide **2.** formation of a peroxide **3.** formation of surface oxide and **4.** regeneration of the surface hydroxide [7]*.

*Reprinted from *Nature Chemistry*, **3**, J. Suntivich, H. A. Gasteiger, N. Yabuuchi, H. Nakanishi, J. B. Goodenough, and Y. Shao-Horn, Design principles for oxygen-reduction activity on perovskite oxide catalysts for fuel cells and metalair batteries, 546–550, Copyright 2011, with permission from Nature Publishing Group.

In addition to studies of the reaction mechanism, there have been some efforts to rationalise why the kinetics of the ORR are facile in the alkaline environment [6]. It is proposed that the peroxide intermediates form preferentially in the alkaline environment, and also desorb more readily [6]. In terms of the thermodynamics, it has been shown that a lower overpotential is needed to facilitate the peroxide pathway at high pH, which could explain why perovskite catalysts are active in this environment. On the contrary, at low pH (such as the environment of a polymer electrolyte fuel cell (PEMFC)) the higher overpotential means that stronger catalytic interaction is required [16].

Although there have been several investigations into the mechanisms of the ORR, not many of these studied the role of the support (e.g. carbon black as shown in Fig. 1.4), while it has been observed that the performance of AFCs can vary depending on the type of support material, indicating that it has an important role to play [17]. More importantly, there has been very little characterisation of the reaction sites on AFC perovskite catalysts. Understanding the nature of the catalyst surface is crucial to define the activity of AFCs, since the surface contains the sites on which reactants will adsorb.

This gap in surface knowledge is a major factor that limits the performance of non-noble metal catalysts. Knowledge of the surface is difficult to obtain since the morphology of the catalysts in these studies is not well defined; they are typically polycrystalline powders. Fine characterisation of AFC catalysis on such powders is very difficult, where the fundamental reaction steps occur on unknown facets at unknown reaction sites. The reliability of predictive modelling based on *ab initio* quantum theory, on the other hand, means that the catalyst-reactant system can be characterised theoretically at the atomic scale in order to provide an understanding of the mechanics behind AFC catalysis. It is, therefore, the focus of this work to investigate and understand the nature of the perovskite catalyst and its surfaces using computational techniques, ultimately working towards being able to manipulate perovskite crystallite morphology to maximise catalytic activity.

1.2 Perovskites

Perovskites can be generalised as compounds that have the structure ABO_3, where A is usually a large cation, B is a smaller cation and O_3 are oxygen anions. This allows for a fairly large range of compositions to exist and each variation has profound effects on the properties that are exhibited. These properties can include superconductivity,

ionic conductivity, colossal magnetoresistance and catalytic activity to name just a few [2, 18–20].

In order to synthesise perovskites there are a multitude of techniques available, such as combustion, sol-gel, hydrothermal, co-precipitation and solid-state reactions [21]. Generally, the route taken to obtain the perovskites can also affect their microstructure, as has been shown in recent work when $La_{0.7}Sr_{0.3}MnO_3$ (LSM) nano-powders were synthesised by three different methods (combustion, citrate and solid-state) and sintered at 1100°C to produce porous pellets. The samples synthesised by combustion and citrate methods presented smaller particle sizes and higher porosity after sintering than those derived from solid-state synthesis [22]. Another example of this has been given in work showing that $La_{0.6}Sr_{0.4}Co_{0.2}Fe_{0.8}O_{3-\delta}$ powders synthesised by an ethylene diamine tetra acetic acid (EDTA)-citrate, sol-gel and a low-temperature auto-combustion process all produced a perovskite structure, but the auto-combusted sample showed greater oxygen non-stoichiometry resulting in different catalytic properties [23].

For the characterisation of perovskites there are also a large number of techniques available. Auger electron spectroscopy (AES), X-ray photoelectron spectroscopy (XPS) X-ray diffraction (XRD), neutron diffraction, scanning electron microscopy (SEM) and transmission electron microscopy (TEM) are commonly used to obtain structural information [24,25]. Electrochemical characterisation (with regards to fuel cell applications) is carried out by techniques such as Electrochemical Impedance Spectroscopy (EIS), Cyclic Voltammetry and Current-Voltage measurements, which allow us to evaluate not only the perovskite material but its performance characteristics in the complete fuel cell system [26]. Density functional theory (DFT) [27] is a modern computational method that can be used to understand how the behaviour of the material on the macro-scale corresponds to its atomic and nano-scale features. With regards to this work, where the important details of a process such as the ORR on perovskite particles is sought, it can allow for an accurate study of the surface and its interactions with reactant gases.

An important consideration for this work is that the use of computational methods for the study of perovskite catalysts enables the identification of their stable surfaces [28]. Subsequently, the structural features of the stable surfaces can be investigated in detail, in order to identify reaction sites or characteristics that lead to high catalytic activity. Furthermore, since it is ideal to maximise the most active surfaces when synthesising a catalyst, it is desirable to use computational methods to determine the environmental conditions necessary to stabilise the active surfaces. In fact, it has been demonstrated that such a method is viable for metal oxides. For instance, a thermodynamic treatment applied to DFT calculations of $LiCoO_2$ [29] demonstrates

that tailoring of the surface morphology to suit requirements is possible with an understanding of the phase diagram of the surfaces in chemical potential space. Using the information provided by phase diagrams, the authors were able to identify that a synthesis route which provided a reducing environment would maximise surfaces that enhance catalytic activity. As an end-goal of this investigation, it would therefore be ideal to adapt this methodology for a perovskite surface that is identified to be the most catalytically active.

1.3 $LaMnO_3$

In this work, the decision to study the perovskite, $LaMnO_3$, was initially guided by evidence in a review of alkaline fuel cell cathodes, which indicates that the catalytic activity of $LaMnO_3$ is among the highest of non-noble metal catalysts [6]. Although the use of perovskites-type oxides as oxygen reduction reaction (ORR) catalysts was first explored in 1970 [30], until the last decade, this class of material had not been studied for alkaline fuel cell (AFC) applications. In fact, the study on which the performance of $LaMnO_3$ was reviewed was only carried out in 2004, and was the first to identify $LaMnO_3$ as a viable ORR catalyst for alkaline fuel cells (AFCs) [4]. Since then, a systematic study of the variation in catalytic activity with the *d*-electron occupancy of various perovskite oxides has demonstrated that $LaMnO_3$ is one of the most active perovskite catalysts for the ORR reaction [7]. It is claimed that this is because $LaMnO_3$ possesses an ideal *d*-electron occupancy (d^4), with neither too weak nor too strong O_2 interactions [7].

In addition to being an optimal material for the ORR, there is a further advantage in studying $LaMnO_3$, since it provides us with a starting material for which to establish a model system. A system such as this is highly valuable since in the future it can be easily modified via doping to compare with many other commonly used perovskites such as $La_{1-x}Sr_xMnO_3$ or $La_{1-x}Ca_xMnO_3$, allowing us to study the atomic scale origins of any change in properties from the parent compound.

The structure of $LaMnO_3$ is like that of many perovskite compounds which have a cubic unit cell consisting of the formula unit ABO_3 (as described earlier); the small cation B is located at the origin; the three oxygen anions are along the x, y and z directions at fractional coordinates $\pm 1/2$, and the larger cation A in dodecahedral interstices in the sites with fractional coordinates $\pm 1/2$, $\pm 1/2$, $\pm 1/2$. Stoichiometric $LaMnO_3$, however, is observed in the orthorhombic structure (as presented in Fig. 1.6) below 750K, when studied by thermal analysis and neutron diffraction [31]. Above

750K the structure becomes cubic until 1010K, where it transitions to the trigonal (rhombohedral) structure [31].

Evidence for the trigonal phases also exists at lower temperatures, however, reports indicate that the earlier onset of the cubic and trigonal transitions is due to an increase in percentage of Mn^{4+} ions [31]. The onset of the transitions is directly affected by the quantity of Mn^{4+} ions; the trigonal transition is observed at 873K for 2% Mn^{4+} ions and at room temperature when greater than 20% [31, 32]. The percentage of Mn^{4+} ions is commonly increased by hole doping of $LaMnO_3$ by A site substitution with lower oxidation state cations ($La_{1-x}Ca_xMnO_3$) and synthesizing samples with excess O ($LaMnO_{3+\delta}$) or La vacancies [32]

The stability of the orthorhombic phase in the lower temperature ranges is largely attributed to the Jahn-Teller distortion of the MnO_6 octahedra and the relaxation of internal stresses by cooperative octahedra rotations, as described by the orbital ordering effect [31,33,34]. Since the orthorhombic structure of stoichiometric $LaMnO_3$ is thermodynamically stable at low temperature, and therefore, also within the operating temperature of AFCs, it is the ideal phase to study in this work.

1.3.1 Review of Experiments

The earliest significant experimental work on $LaMnO_3$ and its related compounds can be traced back to the 1950's, when notable discoveries of its magnetic, electronic and structural properties were first made [25, 35]. These initial neutron diffraction experiments revealed that $LaMnO_3$ was an A-type antiferromagnetic (AAF) insulator, which is antiferromagnetically coupled in the **b** (or y) direction while ferromagnetically coupled in the **a** and **c** (or x and z) directions [25].

$LaMnO_3$ was later determined to be just one among a group of transition metal oxides that are insulators which become metallic upon doping. This doping also often resulted in a range of electrical, thermal and magnetic behaviors within the material, the degrees of which are dependent on the dopant materials and the percentage of doping. The large negative magnetoresistance observed in certain compositions has been studied in detail and become commonly known as colossal magneto resistance (CMR) [36, 37].

Despite these initial discoveries, such perovskite materials have shown only limited technological developments beyond their use in magnetic sensors and switches. Future prospects are largely hindered by the fact that synthesis is expensive while the advantages of CMR devices over conventional devices do not convince industry to invest

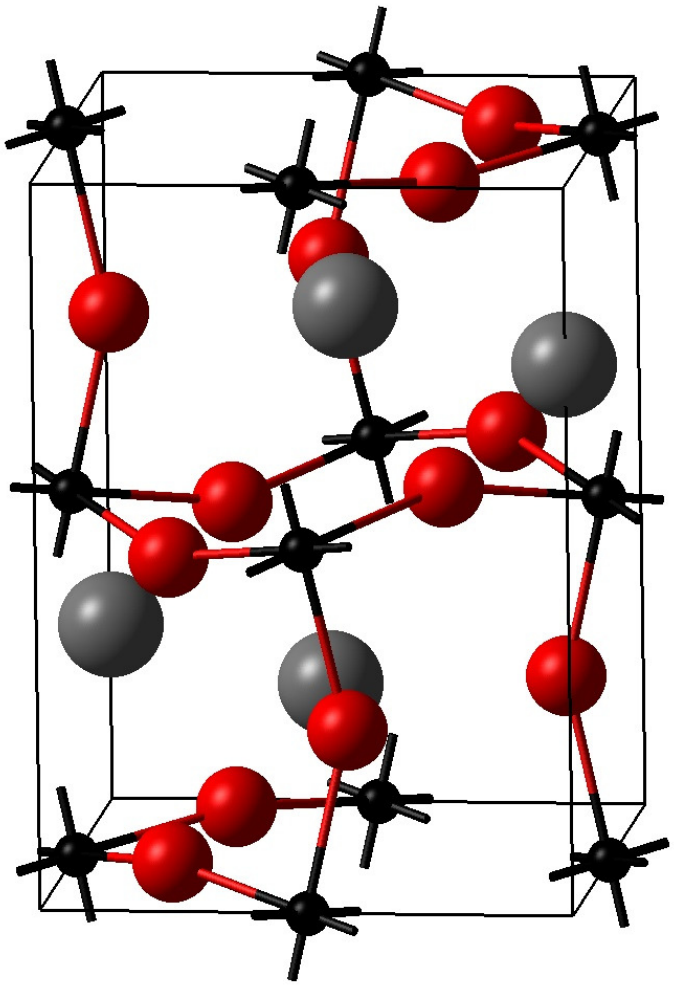

Figure 1.6: A unit cell (four formula units) of the orthorhombic structure of $LaMnO_3$. The grey (large), red (medium) and black (small) spheres represent La, O and Mn ions respectively.

significantly [37].

On the fuel cell front, however, there has been an increasing application. Particularly as the materials for electrodes, ionic conductors and catalysts in SOFCs [1–3]. The range of techniques and the number of studies of $LaMnO_3$ has also greatly increased; X-ray [33, 38–42] and neutron diffraction [31, 33], scanning [41, 42] and transmission electron microscopy [41], electron paramagnetic resonance [40], thermogravimetry (TG) [31, 38, 41, 43], differential thermal analysis (DTA) [31, 42], differential scan-

ning [38, 39, 41] and alternating current calorimetry [39] have all been implemented.

As indicated by the latter techniques above, there have already been several experimental efforts to obtain thermodynamic data using a number of different methods and at a range of temperatures. The thermodynamics of $LaMnO_3$ are an invaluable source of information that give us a powerful benchmarking tool for our simulations and also allow us produce constructs such as phase diagrams, which can indicate the conditions needed for the existence of phases that interest us (this will be elaborated in Sec. 3.2). The heat capacity of $LaMnO_3$ has been determined using semi-adiabatic calorimetry, differential scanning calorimetry (DSC) and alternating current calorimetry [39, 44]. Further analysis of the thermodynamic properties has been carried out by using thermogravimetric methods. Kitayama in particular has employed a technique where the partial pressure of O_2 is varied while recording the weight change of the system [43]. Using this method allowed for the identification of stable phases, as well as the construction of a phase diagram at 1100°C as a function of the partial pressure of oxygen.

While there is a sufficient quantity of thermodynamic data to evaluate simulations of $LaMnO_3$, there is a concern regarding the consistency and accuracy of the data. In this respect there has been an attempt at refining the thermodynamic data for $LaMnO_3$ by Jacob and Attaluri [45]. They have used a calorimetric method to obtain new data while also sourcing data from literature in order to compile a consistent set of thermodynamic properties of $LaMnO_3$. In the process of their work it becomes clear that the oxygen chemical potentials vary widely in literature, most likely due to the range of conditions and the variety of methods applied.

In order to produce more accurate results, Jacob and Attaluri determine the oxygen chemical potential using their own solid-state cell, which also incorporates a buffer electrode that prevents polarisation of the working electrode (this is caused by electrochemical transport of oxygen through the electrolyte). The values they present are in fairly good agreement with previous literature and their final set of data for the thermodynamics of $LaMnO_3$ is used as the reference for $LaMnO_3$ as presented in Ch. 3 (which is sourced and derived mainly from their own work and from Pankratz for the reactants (La, Mn, O_2) reference data [46]).

The inherent properties of $LaMnO_3$ have been fairly well characterised by experiment over the years, but as mentioned earlier, only in the last decade has there been significant advancement in its application for AFCs. In addition to the study claiming that activity of such perovskites was based on *d*-electron occupancy of the transition metal [7], the same authors also demonstrated a procedure with which the electrocat-

alytic activity of powdered oxide catalysts could be measured using a thin film rotating disk electrode [47]. A more recent study uses the same method but applies it to a larger range of perovskites, confirming both the methodology and the hypothesis relating to *d*-electron occupancy [48]. It is interesting to note here that within the range of perovskites there are three common phases: cubic, orthorhombic and trigonal. In the most catalytically active perovskite compounds the trigonal phase prevails. In the case of $LaMnO_3$ in particular, which is tested in both phases, it is the trigonal phase that is more active. The trigonal phase in this case was obtained by subjecting $LaMnO_3$ to a heat treatment in air at 800^oC to give $LaMnO_{3+\delta}$, where $\delta \approx 0.11$ [7]. The higher activity of this phase of $LaMnO_3$ might suggest that it is better to investigate, however, since this system is non-stoichiometric, it is difficult to simulate the exact periodicity of oxygen excess in order to match simulations to experiment. The difference in activity between the orthorhombic and trigonal phases within $LaMnO_3$ is actually not too high so there is no handicap in studying the orthorhombic structure for the overall objectives of this work.

The catalytic system of an AFC, as was discussed earlier, also includes a carbon powder on which the perovskite catalyst powder is impregnated. The role of this carbon powder for the ORR has been investigated recently [49]. The evidence from this study suggests that the mechanism of the ORR can work in conjuction with the carbon powder, which reduces O_2 to H_2O_2. The perovskite catalyst is then responsible for reduction or disproportionation of H_2O_2. Attempting to catalyse the ORR without either the perovskite or the carbon leads to a significant reduction in activity, suggesting that the presence of both components allows for a special reaction route that is not normally favourable.

When considering the details of the reaction processes that have been discussed, it is important to consider the surfaces on which they take place. With this in mind it is useful to know what properties the surfaces hold, and how those properties can affect the reactions that take place in an alkaline fuel cell. For this purpose, literature relating to experimental work on the pristine surfaces of $LaMnO_3$ single crystals or thin films would be the most useful. This is because models of surfaces usually represent idealised and clean surfaces, as it is computationally very difficult to study systems that contain periodic defects and possess non-stoichiometry. It is also a more useful approach to first study a simple system so that prominent features can be easily identified before complicating the system and inducing additional effects. Unfortunately, there has not been much experimental work on specific, pristine $LaMnO_3$ surfaces, but there are still some studies of the surface that provide useful insights towards understanding its

general behaviour.

The adsorption of CO_2 on the $LaMnO_3$ surface has been studied by Hammami *et al.* This is useful as CO_2 plays a large role in alkaline fuel cell operation in that it negatively affects ionic conductivity of the electrolyte and has also been shown to degrade the cathode performance on certain electrodes [50–52]. Experimental measurements of adsorption isotherms were made by Hammami *et al.* and combined with modelling to analyse the surface interactions. An interesting finding with regards to the poisoning of $LaMnO_3$ by CO_2 is that the adsorption of CO_2 was negatively affected by the prior adsorption and desorption of O_2, as evident from the adsorption isotherms in Fig. 1.7. This data suggests that competitive adsorption between CO_2 and O_2 exists (i.e. a portion of the active sites are sensitive to both molecules) and, therefore, it is expected that pre-adsorption of CO_2 on the $LaMnO_3$ surface inhibits the ORR on the cathode by the blockage of active O_2 adsorption sites.

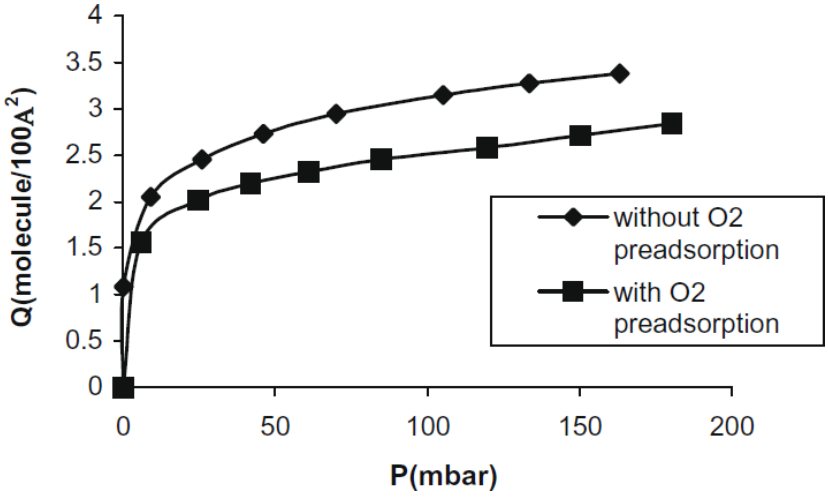

Figure 1.7: Isotherms for adsorbed CO_2 on a surface with and without pre-adsorbed O_2 [52].†

Contrary to these findings, there is also literature regarding a similar perovskite, $LaCoO_3$, where CO_2 and O_2 adsorption was found to be non-competitive. The authors of this study conclude that CO_2 adsorbed on the surface O^{2-} ions while O_2 adsorbs on the surface metal ions [53]. It is inferred, then, that the adsorption of these gases is likely to be strongly dependant on the structure (and phase) of the perovskite substrate. However, there is simply not enough experimental data to make a definite conclusion.

†Reprinted from Surface Science, **35**, M. Sato, M. Ohta, and M. Sakaguchi, Combined experimental and theoretical investigation of the CO2adsorption on $LaMnO_{3+y}$ perovskite oxide, 945 – 950, Copyright (2009), with permission from Elsevier.

This matter is further hindered by the fact that most of the data available is from high temperature studies that relate to SOFC conditions rather than AFC conditions.

In another surface study, the reactivity of various perovskite powder catalysts was investigated with respect to the structural characteristics of the surface region, evaluated by high-resolution transmission electron microscopy (HRTEM), Raman spectroscopy and various electrochemical techniques [54]. In this work the activity of the oxygen evolution reaction (OER), was measured, which, although not the same as the ORR, does also occur in alkaline media and shares many of the same reaction species [54, 55] It was found that the surface regions of certain powders (such as $Ba_{0.5}Sr_{0.5}Co_{0.8}Fe_{0.2}O_{3-\delta}$) that had close proximity between the O $2p$-band centre and Fermi level, degraded and underwent amorphisation after only a few cycles of water oxidation (where any p-band centre higher -2.2 eV relative to the Fermi level is considered close). For the surfaces of materials such as $LaMnO_3$, which have lower p-band centres, the surfaces remained perfectly crystalline. The authors claim this phenomenon is due to the Fermi level pinning of the O $2p$-band when it is close, which allows the simultaneous redox of oxygen and metal ions, causing rapid amorphisation.

In the last year, in what is the only literature that could be found of a well characterised surface facet of $LaMnO_3$, the surface of a (001) oriented $LaMnO_3$ film was studied. The prepared surface is perhaps the closest in mirroring the clean surfaces modelled in computational studies. In this work, the film and its surface were characterised using XAS, XPS, AFM and various electrochemical techniques [56]. The activity was found to be comparable to that of a $LaMnO_3$ powder catalyst, suggesting that the (001) surface is activity dominant. It is also demonstrated here that the Mn^{3+} is the most active valence state for the ORR, in accordance with the e_g filling model [7, 56]. From a theoretical point of view these results are particularly valuable since they can be directly compared to any computational studies of the (001) surface and rationalised at the atomic level.

Despite the promising results for the (001) surface, it is noted in this work that the film, which is grown on Nb-doped $SrTiO_3$ (NSTO) substrate, is only as active as the powder catalyst at a thickness of 10nm. In thinner films it is found that activity decreases, which the authors claim to be a result of electron rich substrate increasing the extent of e_g occupancy in the thinner $LaMnO_3$ films. Additionally, it is also important to note that the $LaMnO_3$ films grown on NSTO adopt a pseudo-cubic geometry, which is different to that observed in the powder catalyst. These structural differences are likely to be a source of variability between powder activity and thin films, and also highlight the importance of the catalyst support (and charge transfer), which is often

ignored when evaluating catalytic activity for AFCs. These variations must also be considered in the model systems, which, if based on the bulk compound are also likely to possess a different structure than that observed in the films.

1.3.2 Review of Computations

A short review of the efficacy of various computational techniques in simulating materials such as $LaMnO_3$ will be provided in Sec. 2.5 in order to justify the method adopted in this work. In this section, therefore, I will only briefly cover some of the early literature relating to computational work on bulk $LaMnO_3$ and focus more on the recent studies of the $LaMnO_3$ surface.

The early computational studies of $LaMnO_3$ used variations of the local spin density approximation (LSDA) and verified the experimentally observed magnetic ordering of the ground state [57–59]. These studies, however, presented a picture of the band structure that was not consistent with the data from photoemission spectra; the energy level calculated for the O $2p$ band is lower than the Mn $3d$ band, while the reverse is true for the experiment [60]. This situation was improved through the use of Hartree-Fock (HF) methods, which were able to correctly describe band levels relative to experiment [60–62]. Following these studies, further improvements to the calculated properties were made using hybrid density functional theory and in particular the B3LYP functional. The value of the band gap, magnetic coupling constants and the nature of the O and Mn states using hybrid functionals were found to be much more consistent with experiment [63].

In recent years the focus of computational studies on $LaMnO_3$ has shifted from the general understanding of the bulk material properties towards insight into how the material is catalytically active in SOFCs. However, since this type of fuel cell operates at very high temperatures, these studies generally focus on the cubic structure of $LaMnO_3$. In one instance both the cubic and orthorhombic phases are considered [28]. In this same work the merits of DFT using the hybrid Becke, three-parameter, Perdew-Wang (B3PW) functional with a linear combination of atomic orbitals (LCAO) basis set and the generalised gradient approximation (GGA) plane wave basis set approach are also compared [28]. These methods are found to be agreement that the orthorhombic structure has a ground state which is AAF, also in alignment with the experimental findings [25]. The hybrid B3PW method, however, allowed for more accurate calculation of the experimentally observable magnetic coupling constants. This is explained by the inclusion of Fock exchange in the hybrid functional, without which they are

overestimated, as observed for the GGA method [28]. Similar behaviour is seen in the band gaps for the orthorhombic phase, which are in agreement with experiment using the hybrid method, but on this occasion are underestimated using the GGA method. These findings are also supported by results in previous studies that use non-hybrid methods, and are in agreement with the conclusions made in a review of the commonly adopted hybrid functionals [64–66]. The comparative study also contains some investigation of various terminations at the (001) and (110) surface. It is reported that the (001) surface is lower in energy than the (110) surface. This was also found to be the case in a previous study of the cubic phase [67]. However, the methodology with which the surface models are generated in the comparative study is not clear, and will be analysed further when compared to the surface studies carried out in this work (see Ch. 5).

In the previous section it was noted that there are not many experimental studies of the $LaMnO_3$ surface, on the computational side, however, there are several reports. In particular, Piskunov, Kotomin, Mastrikov and co-workers have reported several computational studies of the surfaces of $LaMnO_3$ and its related perovskites [68–71]. The majority of this work involves density functional theory (DFT) plane-wave calculations (using VASP code), but there are also some studies using optimised LCAO calculations with Gaussian functions (using CRYSTAL code), such as the work discussed earlier [28, 72]. The consensus from these works is that the MnO_2 terminated (001) surface is the most stable, for both cubic and orthorhombic phase (where the orthorhombic space group setting (*Pbnm* is adopted). The calculations also indicate that certain surfaces are sensitive to environmental conditions and adsorbed species, which can lead to alternate surfaces possessing the lowest energy. For instance, the (110) surface is predicted to only become dominant at low oxygen pressures [70, 71].

There are a number of surface studies in which the adsorption of O_2 on $LaMnO_3$ is studied [70, 73, 74], although focusing mainly on the high temperature (cubic) surface for SOFC applications. These studies conclude that O_2 is most likely to adsorb on the Mn sites, and that dissociative adsorption is more favourable than molecular adsorption; this is contrary to what is observed on the isomorphic material $SrTiO_3$, where calculations show that adsorbing O (dissociated) ions prefer the bridge position between Ti and O ions [70]. A mechanism is proposed for the adsorption, dissociation and diffusion of O_2 on cubic $LaMnO_3$ surfaces, in which the adsorbed O_2 passes through superoxide (O_2^-) and peroxide ($O_2{}^{2-}$) states before dissociating into O ions that are incorporated into the lattice [73].

The adsorption of O_2 on the orthorhombic phase of $LaMnO_3$ has only recently

been investigated [75]. In fact, this particular study explores the ORR kinetics on the surface towards fuel cell applications, where a range of molecular species are involved. Generalised gradient approximations (GGA and GGA+U) and the screened hybrid Heyd-Scuseria-Ernzerhof (HSE06) approach are used to determine the order of reactivity between $LaMnO_3$, $LaCrO_3$ and $LaFeO_3$, which is found to decrease in that order for only the HSE06 method. This is in agreement with the optimal e_g filling model suggested by Suntivich*et al.* [7]. However, a shortcoming of this study is that it only considers one particular surface (site), the (001) transition metal termination. It is certainly possible that adsorption on other surfaces could give very different kinetics, thereby altering the order of reactivity. It is also found that the order of reactivity from the GGA methods does not agree with the experiment, perhaps indicating that the hybrid technique is more reliable for such studies [7, 75].

In addition to the e_g filling model developed experimentally, the reactivity of $LaMnO_3$ and similar perovskites towards the ORR has been evaluated using plane wave GGA DFT in a study searching for descriptors with which better catalysts can be identified [76]. This particular study is focused on the high temperature SOFC applications so is not directly applicable to the AFC ORR, but the descriptor identified may give some hints for future studies of the low temperature processes. The main findings reported are that the O p-band centre, the bulk O vacancy formation energy and surface O binding energy to the transition metal cation show correlation to ORR activity in the SOFC. From among these descriptors the p-band centre (measured relative to the Fermi energy) is the most useful, since it can be identified easily as a bulk property without complex surface analysis/calculations.

Further analysis of ORR descriptors in another study emphasis the importance of the adsorption (binding) energy of reaction intermediates which bind through O atoms [77]. This is because the adsorption energy directly affects the reactions steps in which surface to O bonds are formed or broken, so it should neither be too strong nor too weak. It is further claimed that the filling of t_{2g} or e_g states (as discussed earlier) is a good descriptor since it influences the forming of occupied bonding and antibonding O states [77]. The strength of the surface to O bond is dependant on these states, since completely unoccupied antibonding O states give strong binding energies, while completely occupied antibonding O states give weak binding energies.

It is interesting to note that no study could be found that relates the impact of J-T distortion on the ORR. The J-T effect is reported in one study of the orthorhombic $LaMnO_3$ surface [78], in which DFT calculations are carried out to detail the structural distortion. They mainly report the % displacement of the surface atoms in the relaxed

surface, with respect its unrelaxed geometry when cut from the optimised bulk. However, their study was limited to the (001) surface only. No comprehensive/systematic study of the range of surfaces and terminations that are possible with orthorhombic $LaMnO_3$ could be found in the literature.

Finally, it is necessary to point out that for the analysis of surfaces in literature it is crucial to note the exact crystal structure of the material being modelled. From among the studies that consider the orthorhombic structure of $LaMnO_3$ there are actually two symmetry variations (space group settings). The standard space group setting is *Pnma* (No. 62) while the *Pbnm* setting has also been adopted [67, 71]. In the latter case the set of lattice vectors **abc** of the *Pnma* setting are transformed into **cab**, i.e. the (101) surface of the *Pnma* setting corresponds to (110) of the *Pbnm* setting [79,80]. In this work the standard setting will be adopted so care must be taken when making comparisons between studies to ensure that equivalent structures are being evaluated.

1.4 Competing Oxides

In order to explore the catalytic properties of $LaMnO_3$ and exploit it for AFC applications, it is useful to study its thermodynamics. Having an understanding of the thermodynamics of $LaMnO_3$ allows for the particular environmental conditions required, during synthesis, for the stabilisation of crystal facets (surfaces) preferred for high catalytic activity to be determined. These conditions can be obtained through construction of a phase diagram of the surfaces of $LaMnO_3$. However, before the stability of $LaMnO_3$ surfaces can be explored, it is necessary to establish the thermodynamic stability of bulk $LaMnO_3$, since the potentials which limit bulk stability also apply to the surface. The thermodynamic stability of bulk $LaMnO_3$ is established by the chemical potentials of the elements in La-Mn-O system. This system also allows for the existence of other compounds made up of La, Mn and O, which define multiple phase separation boundaries that delimit the region of $LaMnO_3$ stability. It is therefore necessary, as part of a study into $LaMnO_3$, to also explore the stability of the competing compounds in this system. Doing so will not only provide a phase diagram for the stability of compounds in the La-Mn-O system, but the accuracy with which the properties of various compounds are calculated will reflect the accuracy of our computational method. For instance, if the properties of the series of Mn oxides that exist in this system are accurately predicted, then the methodology adopted is validated for the study of the $LaMnO_3$ surfaces, as we have accounted for various oxidation states and coordination environments for Mn.

Before discussing the Mn oxides in detail it is worth briefly mentioning La_2O_3, which, although may not be as relevant with regards to the $LaMnO_3$ surface, must still be properly simulated in order to construct the bulk phase diagram. La_2O_3 can be used to synthesise $LaMnO_3$ and has many applications including catalysis [81]. La_2O_3 generally adopts a trigonal (hexagonal) structure, except at very high temperatures where the cubic phase is formed [82]. The oxidation state of La can be either +2 or +3, the latter being far more stable. As a result of the +3 oxidation state, La_2O_3 is non-magnetic, although it has been reported that doping with nitrogen can induce magnetism [83]. In this investigation, both phases of La_2O_3 will be simulated in order to evaluate which is more stable. Similarly, it is necessary to determine the most stable phase of each Mn oxide for construction of an accurate phase diagram.

The Mn oxides are a variety of compounds with a highly diverse range of properties and applications that can change depending on the oxidation state of Mn, the number of coordinating O atoms and the resulting structures adopted. MnO (II) is the oxide which contains the lowest oxidation state of Mn from among the more common oxides, which include Mn_3O_4 (II/III) Mn_2O_3 (III) MnO_2(IV). It has a cubic structure of the NaCl rock salt type, where Mn and O are octahedrally coordinated to each other (Fig. 1.8 a), and exists in an antiferromagnetic (AFM) configuration characterised by a paramagnetic (PM) to AFM transition when the temperature drops below 118 K. The antiferromagnetism is known to be of G-type, where the spins are ferromagnetically aligned only in the (111) plane [84].

In nature the stoichiometry of MnO can vary to a great degree, which is also the case for Mn_3O_4, a far more complex compound in which Mn occurs in two different oxidation states, and where a spinel structure is adopted (Fig. 1.8 b). This structure is made up of a cubic close packed (CCP) oxide anions where Mn^{3+} and Mn^{2+} respectively occupy octahedral and tetrahedral sites and a split of 2:1 between the Mn sites balances the 8- charge of the anions in the unit cell. The spinel generally exists in a tetragonally deformed state at temperatures below 1433 K, above which it adopts the perfect cubic spinel form [85]. Mn_3O_4 is paramagnetic at room temperature but at lower temperatures the structure becomes very complex (spins are canted), with magnetic phase transitions upon dropping below 42 K, and again at 39 K and 33 K [85]. The transition at 42 K is cited as the Curie temperature (T_c), i.e. the temperature below which the long range magnetic ordering of the Ferrimagnetic (FiM) type manifests itself. The transitions that occur below this temperature then vary the long range ordering of the Mn^{3+} ions [85–87].

Mn_2O_3 is somewhat unconventional amongst the transition metal oxides in that it

has not been reported to take up the corundum (Al_2O_3) structure, instead it has long been considered to have a cubic structure of the bixbyite type (IA3). The majority of research in Mn_2O_3 does not relate any other possibilities; however, in 1967 Norrestam demonstrated that the structure could belong to an orthorhombic space group at low temperatures [88] (Fig. 1.8c). Subsequently two reports confirmed this finding and also related evidence of a phase transition around 302-308 K, above which Mn_2O_3 becomes cubic [89, 90]. Despite this there has been little further investigation of the orthorhombic structure. The orthorhombic structure is made up of a lattice of strongly Jahn-Teller distorted octahedral Mn(III) sites, while the remaining Mn(III) sites are heavily distorted planar sites (Fig. 1.8 C). With regards to magnetism there is some debate; earlier reports indicate AFM transitions at 80-90 K and 25 K; however, a recent report has indicated ferromagnetism at temperatures below 45 K [91, 92].

MnO_2 is probably the most structurally complex Mn oxide and is able to exist in a variety of polymorphs. Among these there are two which are more common in nature, one of which is its rutile form (pyrolusite). For this structure the Mn cations are octahedrally coordinated by 6 O anions, each of which is coordinated by 3 Mn cations in a trigonal planar geometry (Fig. 1.8 d). The other is its orthorhombic form (ramsdellite) which has the same cation octahedral sites as the rutile form but only half of the anion trigonal planar sites, the remainder are pyramidal sites. This difference is expressed in the bulk material for the orthorhombic structure by the presence of chains of paired edge sharing octahedra as opposed to the single octahedra chains in rutile [93]. A third form of MnO_2, known as nsutite, is considered valuable in battery applications because of its use in dry-cell batteries as cathodic material. This form consists of intergrown ramsdellite and pyrolusite, which can change in composition depending on where the mineral was sourced or how it is synthesised, often leading to varying degrees of battery performance [94].

The rutile form of MnO_2 has long been considered to have unconventional magnetism with a screw type ordering. This was first reported by Yoshimori who described the magnetic structure as consisting of spins screwing along the four-fold crystalline axis [95]. The orthorhombic form on the other hand is believed to be antiferromagnetic at low temperatures, though details of this could not be found in literature [96].

1.4.1 Review of Experiments

The Mn oxides have been studied throughly in the past and there are various experimental results detailing their properties. In this work the main concern are the properties

a) MnO

b) Mn_3O_4

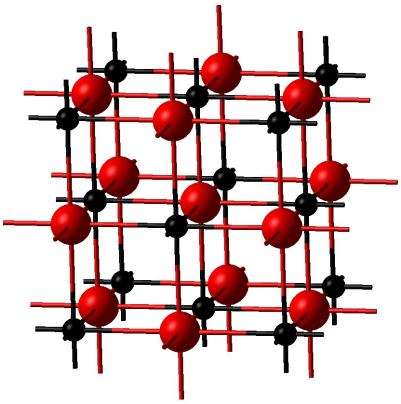

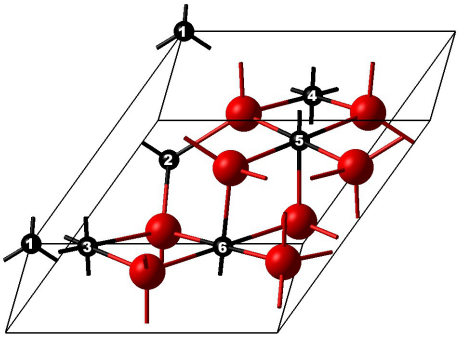

c) Mn_2O_3

d) MnO_2

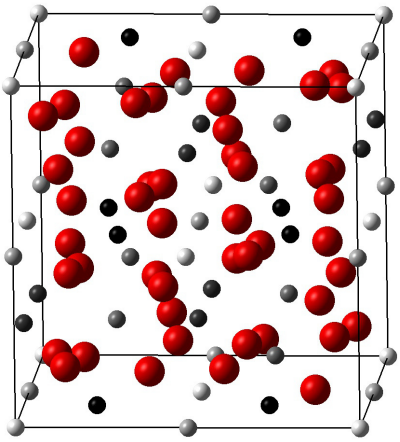

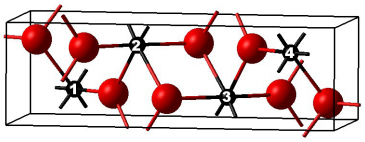

Figure 1.8: The structures of the Mn oxides in their ground states. Medium red and small black spheres correspond to the O and Mn atoms respectively. In the case of Mn_3O_4 and MnO_2, the labelling of the Mn atoms is linked to the assignment of spin in Tables 3.2 and 3.3. For Mn_2O_3, symmetry irreducible Mn atoms are given in gray scale color without Mn-O bonds for clarity.

related to catalysis, therefore, an exhaustive review is not carried out here. The thermodynamics of the Mn oxides are also one of the areas that are important for this work as they are connected to the stability of $LaMnO_3$. In fact, as discussed earlier, a phase diagram for $LaMnO_3$ that details the regions where it can exist cannot be constructed without consideration of the regions where the competing oxides are able to exist. The thermodynamic analysis of these oxides is documented in early literature [46] and the basic data such as the enthalpy, entropy and standard Gibbs energy of formation is

Table 1.1: Thermochemical data for Mn oxides, La_2O_3, and $LaMnO_3$ $\Delta_f H^o$ is the enthalpy of formation, $\Delta_f G^o$ is the Gibbs free energy of formation, S^o is the entropy and C_p is the specific heat capacity at constant pressure, in all of which ^{o} indicates standard temperature and pressure [45, 99, 100].

Compound	$\Delta_f H^o$ **kJ/mol**	$\Delta_f G^o$ **kJ/mol**	S^o **J/mol K**	C_p **J/mol K**
MnO	-385.2	-362.9	59.7	45.4
Mn_3O_4	-1387.8	-1283.2	155.6	139.7
Mn_2O_3	-959.0	-881.1	110.5	107.7
MnO_2	-520.0	-465.1	53.1	54.1
La_2O_3	-1793.7	-1705.8	127.3	108.8
$LaMnO_3$	-1437.99	-1354.62	116.68	102.65

available from many sources that list thermochemical data [97–99]. Typically these would have been obtained by using calorimetry to determine the heat capacity, which can then used to calculate the listed data. The relevant thermochemical data for the competing oxides is given in table 1.1, where phases and stoichiometry are consistent with the ground states determined in Ch. 3.

With this data alone it is difficult to say much about the thermodynamics of the Mn oxides, however, work carried out by Fritsch and Navrotsky in 1996 [100] gives some insight. Here previous studies were reviewed and combined with their own experiments to give a thorough analysis of the thermodynamic properties of the Mn oxides. One of the more useful parts of this work is an analysis of the energetic trends of the oxides by a comparison of the enthalpies of oxidation per mole of Mn. The results show that spinel Mn_3O_4 and bixbyite Mn_2O_3 (these structures are presented in Fig. 1.8) are significantly more stable than the other oxides, which could be attributed to the stabilising effects of the strong Jahn-Teller distortions due to the Mn^{3+} (d^4 high spin) valence state [100].

With regards to the application of these materials as catalysts, there have been several studies over the years that show evidence of activity for both supported and unsupported Mn oxides [101]. All of the Mn oxides show good catalytic activity for the oxidation reaction of CO, where all the oxides except MnO are able to oxidise CO even in O rich atmosphere [102, 103]. As it might be expected for the relatively O deficient MnO and Mn_3O_4, an ability to gain weight in an O rich atmosphere was also exhibited. This can be attributed to reduction of O and is an important consideration when analysing the material suitable for the ORR in AFCs [102, 103].

A more recent study of the oxidation of CO further supports that MnO, MnO_2 and Mn_2O_3 are all capable of catalysing the reaction, adding that the activity for MnO is the lowest while the activity for Mn_2O_3 is highest. The mechanism for MnO_2 and Mn_2O_3 was attributed to the Langmuir-Hinshelwood mechanism where an interaction

between adsorbed CO and O begins the oxidation of CO, while for MnO it was thought that adsorbed CO reacts with O on the MnO lattice as in the Mars-van-Krevelen mechanism [104]. The activity of the Mn oxides appears to be somewhat generic and a similar trend of activity is also seen for the decomposition of NO_2, where Mn_2O_3 and Mn_3O_4 are noted to be the most active and stable Mn oxides, with Mn_2O_3 proving to be the better [105, 106].

With regards to the application of these catalysts in AFCs, there have been some reports investigating the catalytic properties of Mn oxides for the ORR. In one case the ORR is investigated for an Mn_xO_y air electrode in order to reveal the mechanism of the reaction [107], while in another study, the ORR is investigated in a KOH electrolyte for Mn oxide catalysts dispersed on carbon powder [108]. In the latter study the reaction was investigated to show that the highest activity can be expected for MnO_2/C and Mn_3O_4/C. This is related to the fact that the composition Mn oxide electrodes can be a mixture of the various oxides, as determined by X-ray Absorption Near Edge Structure (XANES). The MnO_2/C and Mn_3O_4/C electrodes were found to have the highest MnO_2 content, while MnO/C had the lowest and Mn_2O_3/C was not studied. On the materials that had high MnO_2 content (MnO_2/C and Mn_3O_4/C) the highest activity was seen, therefore indicating that MnO_2 was a key factor for the reaction pathway. The authors of the study propose that the reaction proceeds by a reduction of Mn^{4+} (the valence state of Mn in MnO_2) to Mn^{3+}, followed by the rate determining electron transfer of Mn^{3+} to adsorbed O. This regenerates Mn^{4+} and advances a 2-electron mechanism to produce OH^- and HO_2^-, the latter of which also undergoes a disproportionation reaction to give O_2 and OH^- [108].

1.4.2 Review of Computations

Despite the long history of experimental work on the Mn oxides, there has been relatively little focus on the theoretical side. A detailed *ab initio* study of the electronic, structural, elastic and vibrational structure of MnO was first carried out in 1994 [109]. The calculations used in the study were based on the Hartree-Fock (HF) LCAO method and the properties calculated were found to be in good agreement with available experimental data. The failure of standard DFT methods to accurately describe the properties of Mn containing systems may be part of the reason why there has been relatively little computational work on these oxides. It is known from experimental studies that Mn oxides have quite a complex correlation between structure and magnetism and have oxidation states that commonly vary between II and IV, which makes

them difficult to describe with some of the commonly adopted computational methods. The conflict between the calculated properties of Mn oxides using different functionals for DFT is presented in recent studies by Franchini *et al.* [110, 111]. In this instance, when using the Perdew-Burke-Ernzerhof (PBE) functional, DFT calculations of Mn_3O_4 indicate metallic behaviour, while semiconducting behaviour is exhibited with PBE0 (a hybrid version of PBE) and HSE03 calculations. Similar differences are also seen for the other Mn oxides and it appears that the use of hybrid functionals (such as PBE0, HSE03 or B3LYP) provides a much better description of their properties. From the results presented in the work of Franchini *et al.* it is apparent that for the study of formation energies, hybrid functionals can also consistently provide much more accurate and unbiased results than standard DFT functionals.

In the case where the $+U$ correction (also discussed in Sec. 2.5) is added to account for self-interaction errors in the functionals, the results show an overall improvement with a choice of 4 eV for U. However, the method of adding a U correction reduces the predictive power of DFT since different values of U are ideal for compounds that exhibit different exchange and correlation interactions, while the addition of an "ad hoc" U parameter means the method is no longer a first principles technique. A further consideration is the fact that the $LaMnO_3$ surfaces may exhibit a range of valence states and coordination environments depending on the Mn-O bond cleavage, making an ideal U value difficult to isolate.

Since the hybrid methods provide a consistent treatment of exchange and correlation effects and give generally accurate formation energies, it would appear that these methods are the best option when treating Mn oxides. Considering these findings it is difficult to not be sceptical about the results of studies that have neglected the use of hybrid functionals, but, as pointed out by Franchini *et al.*, with certain corrections the properties can be reasonable. Additionally, with certain properties, such as the density of states, there can be minimal differences in the description of the macroscopic behaviour of the compounds (i.e. whether they are insulating) [111].

In recent years there have been some computational studies of individual Mn oxides, with several reports on MnO that tend to accurately reproduce the electronic properties observed experimentally [110, 112, 113]. The other oxides have not been investigated to the same extent, but, there has recently been a study focusing on the structure and stability of MnO_2 using the GGA approximation to DFT [114]. Here the authors claim that the pyrolusite phase is the ground state in stoichiometric MnO_2, though not for the ferromagnetic spin arrangement. They also claim that the ramsdellite form is stabilised by Ruetschi defects which introduce disorder into the material.

Notable theoretical work on Mn_3O_4 could only be found in recent years, perhaps due to the complexity of the compound. The electronic properties of Zn doped and pure Mn_3O_4 have also been studied using GGA DFT calculations, showing a transition from the ferrimagnetic ground state to ferromagnetic upon doping [115]. With regards to catalysis, the interaction between CO and the Mn_3O_4 (001) surface has been investigated by DFT to show that the tetrahedrally coordinated Mn is a favoured adsorbtion site [116].

For Mn_2O_3, only a couple of theoretical studies could be found. The work by Franchini *et al.* analysed its formation energy and the structural, magnetic and electronic properties for the orthorhombic geometry [111]. The magnetic structure of the orthorhombic phase has subsequently been studied using a combination of DFT $+U$ and neutron diffraction [117]. The results from both of the methods reported in this work suggest that the ground state is antiferromagnetically ordered along a principal axis with secondary ordering in an orthogonal axis [117].

1.5 Outline

1.5.1 Objectives

In this work the main objective is to develop an understanding of $LaMnO_3$, so that it can be optimised for its application as an alkaline fuel cell catalyst. Since there has not been much progress in studying the surfaces of this material by experiment, there is very little understanding of the sites at which the AFC ORR occurs. It is, therefore, necessary to use simulations with which we can model the surfaces of $LaMnO_3$ and explore the reaction sites. However, this is not a simple task that can be easily completed in the limited time available for this work. In order to make measurable progress, it is useful to split the overall aim into smaller objectives that, if achieved, are still valuable for the understanding $LaMnO_3$ independently.

Phase Stability and Thermodynamics

As a starting point, the stable structure of bulk $LaMnO_3$ in the AFC environment will need to established. Furthermore, since we are interested in the stabilising the catalyst surfaces at which the ORR can occur and manipulating its crystal morphology to maximise those surfaces, it will be necessary to carry out a thermodynamic study of all the competing phases in the La-Mn-O system. The thermodynamics of the bulk phases will not only provide the groundwork on which the surface thermodynamics can

be explored, but also indicate the accuracy of our simulations.

Identifying a Surface Descriptor

In addition to characterising the structure of $LaMnO_3$, it will also be very useful to be able to provide a property or marker relating any surfaces studied, so that they can be easily identified by experiment. This could be achieved by associating changes in density of states (DOS) to the range of Mn valences that are possible in different Mn oxides (or $LaMnO_3$ surfaces). The changes in DOS should correlate with what is observed when Mn valence changes in experimental spectroscopy (EELS, XPS) of Mn oxides, providing a route for surface identification.

Surface Stability

As evident from the review of literature, there has not been any systematic evaluation of the range of surfaces available on the orthorhombic phase of $LaMnO_3$ by computational methods. Therefore, it will be useful to establish which surfaces are formed and to determine the mechanisms by which they are stabilised. This will allow us to characterise the range of adsorption sites typically available for the various reactants and intermediates of the ORR.

Reaction Site Characterisation

In order to determine the actual sites that are active to the ORR in an AFC, it will be necessary to characterise the reactivity of any sites that are identified. This can be achieved by adsorption of the molecular species that are present in ORR, and determining if the energy of binding is ideal for reactivity. Furthermore, if the structural characteristics or vibrational frequencies of the adsorbed molecules are determined, it is also possible to determine the presence of these sites and adsorbed species on actual $LaMnO_3$ crystallites by experimental techniques.

1.5.2 Thesis Structure

Following this introduction, Ch. 2 will discuss the techniques that will be used in this work and their theoretical background, as well as providing the computational details of the calculations performed. In Ch. 3 the ground states and thermodynamics of the compounds in the La-Mn-O system are studied, leading to a phase diagram demonstrating the stability regions of the competing oxides. Chapter 4 explores the

possibility of mapping the oxidation states of Mn by correlating the signals observed in electron energy-loss spectra to unoccupied density of states. The structure and stability of the low-index, non-polar and stoichiometric surfaces of $LaMnO_3$ is determined in Ch. 5, with insight into the effects of Jahn-Teller distortion and coordination loss of surface Mn ions. In Ch. 6 the available Mn adsorption sites of the surfaces studied in the previous chapter are evaluated by the adsorption of O_2 molecules. The adsorption modes and binding energies are characterised, predicting the activity of the available sites and their corresponding surfaces. Lastly, Ch. 7 summarises the main outcomes of this work and its impact in the field of perovskite AFC ORR catalysts.

2

Theoretical Background and Techniques

In this chapter the background of the quantum mechanical simulations used for this Thesis will be detailed. Firstly the electronic structure methods that form the basis of our calculations are discussed, followed by an explanation of the processes by which these calculations are carried out. Finally, the procedure of geometry optimisation is described and the computational details are presented.

2.1 Electronic Structure Methods

The aim of this section is to briefly discuss the theories and methods developed over the years that are currently implemented in quantum mechanical (QM) simulation. The most fundamental equation in the field of quantum mechanics is arguably the *Schrödinger equation*. By solving it, we aim to obtain all of the possible information relating to the system it is applied to. In reality though, solving it analytically is impossible except for the most trivial of systems due to the complexity of many-body interactions.

The time independent non-relativistic Schrödinger equation, which describes a many-body system, is written as:

$$\hat{H}\Psi = E\Psi \tag{2.1}$$

where $\hat{H}$ is the Hamiltonian operator, Ψ is the many-body wavefunction that depends on the spatial coordinates of the electrons and nuclei, while E is the energy of

the system. The Hamiltonian operator is made up of the sum of the kinetic (T) and potential (V) operators of the system:

$$\hat{H} = \hat{T} + \hat{V} \tag{2.2}$$

Since the analytical solution of the Schrödinger equation is impossible for most systems, a number of simplifications are made to allow a solution. When these are applied to a system consisting of a collection of atoms, their ground state energy is readily obtained. To begin with, lets us consider the *Born-Oppenheimer Approximation*. This approximation comes about when we consider that the forces between the particles in a system of interacting electrons and nuclei are of a similar magnitude due to their charge. Taking this point, if we assume that at equilibrium their momenta are also similar, then it follows that the velocity of the nuclei must be very low by consideration of their significantly larger mass. This leads to the following assumption which defines the Born-Oppenheimer Approximation [118]:

- since the nuclear motion is so much slower than the electron motion, the nuclei are seen as fixed by the electrons.

This essentially allows us to separate the electronic motion and nuclear motion and write the total wavefunction as the product of electronic wavefunction Ψ_e (which is a function of only the electronic coordinates but has a parametric dependence on the nuclear coordinates) and the nuclear wavefunction Ψ_n (which is a function of only the nuclear coordinates) [118]:

$$\Psi = \Psi_e \Psi_n \tag{2.3}$$

A core component of many quantum mechanical codes that determine the ground state of a system is *the variational theorem*, which approximates a solution to the Schrödinger equation. When calculating the total energy for a state that is specified by a particular Ψ, we look for the expectation value of the Hamiltonian, defined by:

$$E[\Psi] = \int \Psi^* \hat{H} \Psi d\mathbf{r} \equiv \left\langle \Psi \left| \hat{H} \right| \Psi \right\rangle \tag{2.4}$$

where the E[Ψ] indicates that the energy is a $functional$ of the wavefunction (it is a number that depends on the form of the function, i.e. the form of Ψ). According to the variational theorem, the energy corresponding to a trial wavefunction Ψ_t can never be lower in value than the true ground state energy E_0, which is the expectation value

of the Hamiltonian calculated using the true ground state wavefunction Ψ_0 represented by the formula:

$$E[\Psi_t] \geq E_0 \tag{2.5}$$

This allows us to search for a solution to the ground state energy (E_0) by searching all possible wavefunctions and identifying the wavefunction (Ψ_0) that minimises the total energy.

These concepts greatly simplified the problem of solving the Schrödinger equation and, eventually, *Hartree-Fock Theory* was developed and became one of the first methods to try to find a solution for Ψ, the many-body wavefunction. It is now known as the starting point for a number of better approximations, which today are able to accurately predict chemical properties of systems, though with a computational cost that scales sharply with an increasing number of electrons.

Hartree-Fock theory takes an initial guess at the wavefunction using an ansatz for the structure of Ψ, assuming it to be an antisymmetric product of wavefunctions (ϕ_i, or orbitals) that depend on the coordinates of a single electron, essentially simplifying the many-body problem into a number of coupled single-body equations:

$$\Psi_{HF} = \frac{1}{\sqrt{N!}} det[\phi_1\phi_2\phi_3...\phi_N] \tag{2.6}$$

where *det* indicates a matrix determinant. Historically, the Hartree-Fock theory implements the Slater determinant in Eq. 2.6 as an improvement over the Hartree product. By using such a method, the wavefunction automatically becomes zero when two electrons of the same spin state occupy the same orbital, thereby automatically satisfying the Pauli exclusion principle.

By substitution of the ansatz (Eq. 2.6) into the Schrödinger equation, an expression for the Hartree-Fock energy, E_{HF}, is obtained (here it is defined using atomic units):

$$\begin{aligned} E_{HF} = &\int \phi_i^*(\mathbf{r}) \left(-\frac{1}{2}\sum_i^N \nabla_i^2 + V_{ext} \right) \phi_i(\mathbf{r}) d\mathbf{r} + \\ &+ \frac{1}{2}\sum_{i,j}^N \int \frac{\phi_i^*(\mathbf{r}_1)\phi_i(\mathbf{r}_1)\phi_j^*(\mathbf{r}_2)\phi_j(\mathbf{r}_2)}{\mathbf{r}_1 - \mathbf{r}_2} d\mathbf{r}_1 d\mathbf{r}_2 + \\ &- \frac{1}{2}\sum_{i,j}^N \int \frac{\phi_i^*(\mathbf{r}_1)\phi_j(\mathbf{r}_1)\phi_i(\mathbf{r}_2)\phi_j^*(\mathbf{r}_2)}{\mathbf{r}_1 - \mathbf{r}_2} d\mathbf{r}_1 d\mathbf{r}_2 \end{aligned} \tag{2.7}$$

where the second term corresponds to the classical Coulomb energy and the third term is the exchange energy [119]. The final aspect of Hartree-Fock theory to consider is its iterative nature. By applying the variational theorem to the Hartree-Fock energy under the constraint that the orbitals are orthonormal, the ground state orbitals are obtained, i.e. a new set of orbitals are produced each time the energy is calculated using the Hartree-Fock equations, until the orbitals are self-consistent. The application of this procedure is what leads to Hartree-Fock theory to be considered a self-consistent field (SCF) method.

The Hartree-Fock equations, which are the outcome of the preceeding steps, ultimately describe the electrons under the influence of a mean field potential made up of the classical Coulomb potential and non-local exchange potential:

$$\left[-\frac{1}{2}\nabla^2 + v_{ext}(\mathbf{r}) + \int \frac{\rho(\mathbf{r}')}{|\mathbf{r}-\mathbf{r}'|}d\mathbf{r}'\right]\phi_i(\mathbf{r}) + \int v_x(\mathbf{r},\mathbf{r}')\phi_i(\mathbf{r}')d\mathbf{r}' = \epsilon_i\phi_i(\mathbf{r}) \tag{2.8}$$

where the non-local exchange potential, v_x, is such that:

$$\int v_x(\mathbf{r},\mathbf{r}')\phi_i(\mathbf{r}')d\mathbf{r}' = -\sum_i^N \int \frac{\phi_j(\mathbf{r})\phi_j^*(\mathbf{r}')}{|\mathbf{r}-\mathbf{r}'|}\phi_i(\mathbf{r}')d\mathbf{r}' \tag{2.9}$$

In general, the Hartree-Fock method provides a good description of materials that have well localised electrons, but gives somewhat unsatisfactory results in systems that have a small or no band gap, such as semi-conductors and metals. The neglect in describing instantaneous interactions (correlation effects) between electrons leaves the picture of chemical bond formation incomplete, and is crucial for an accurate evaluation of the molecular energies and properties of the system. The energy associated with these electron correlation effects is defined as the difference between the exact non-relativistic energy of system and the Hartree-Fock energy [120]. The absence of electron correlation has since been addressed in the development of more advanced methods such as Coupled Cluster (CC) and Møller-Plesset (MP) theory, which are amongst the most accurate and commonly used techniques in modern day computational chemistry, being able to accurately predict chemical properties. However, with incorporation of electron correlation, the complexity of the calculations is increased with the computational cost rising by the number of electrons in the system to the power of 7 (for the most accurate versions - CCSD(T) and MP4). As a result these techniques often become too costly for anything larger than medium sized molecules, rendering them useless for many systems of current interest. In order to overcome this, recent variations of MP

theory take advantage of shorter range treatments of correlation, as implemented in the CRYSCOR code [121, 122].

An alternative method of studying large systems with a lower cost is through the application of density functional theory (DFT). The shortcomings of the Hartree-Fock theory arise from the assumption that the many-electron wavefunction should be expressed in terms of many single-electron wavefunctions. In 1964, Hohenberg and Kohn suggested that to solve the many-electron wavefunction with many single-electron wavefunctions was too inefficient, instead, the electron density (ρ) should be the fundamental variable that is used to calculate the ground state energy [123]. This would mean that then all of the ground state properties of the system are functionals of the ground state electron density. A statement that is dependent on the first Hohenberg-Kohn theorem which says:

- the electron density determines the external potential.

This statement indicates that the electron density must also uniquely determine the Hamiltonian operator, since the Hamiltonian operator is calculated from the external potential and the total number of electrons, which is simply the integration of the electron density over all space. The proof of this theorem has been given by Hohenberg and Kohn, and also Levy in 1979 [124], but is explained most intuitively using an argument put forward by the spectroscopist E. B. Wilson during a 1965 meeting, where he observed:

1. the charge density has a cusp that defines the position of the nuclei,
2. the heights of the cusps define the sizes of the nuclear charges.

Thus establishing that the energy is indeed a functional of the charge density ($E[\rho]$). In order to apply this theorem to a system and find a ground state from an initial guess, we still need to apply a variational theorem. This is defined by application of the second Hohenberg and Kohn theorem:

- For any positive definite trial density, ρ_t, such that $\int \rho_t(\mathbf{r})d\mathbf{r} = N$ then $E[\rho_t] \geq E_0$

which is proved simply by the fact that the trial density is used to determine a unique trial Hamiltonian and thus trial wavefunction, Ψ_t. If we consider the variational theorem for the Schrödinger equation (Eqs. 2.4 and 2.5), then it readily follows that:

$$E[\Psi_t] = \left\langle \Psi_t | \hat{H} | \Psi_t \right\rangle \geq E_0 \equiv E[\rho_t] \geq E_0 \tag{2.10}$$

and therefore allowing us to apply a SCF method. However, this argument also restricts the use of DFT to ground state studies. The theorems together lead to the fundamental statement of DFT [119]:

$$\delta \left[E[\rho] - \mu(\int \rho(\mathbf{r}) d\mathbf{r} - N) \right] = 0 \tag{2.11}$$

where the minimum of $E[\rho]$ corresponds to the electronic ground state energy constrained by the chemical potential, μ. The energy functional $E[\rho]$ can be separated into the terms:

$$E[\rho] = T[\rho] + V_{ext}[\rho] + V_{ee}[\rho] \tag{2.12}$$

related to the operators of the Schrödinger equation in Eq. 2.2), where $T[\rho]$ is the kinetic energy, $V_{ext}[\rho]$ is the interaction with the external potential (this is considered to be the potential from the atomic nuclei and any external field applied to the system as a whole) and V_{ee} is the interaction between electrons. The external potential term is easily determined but the kinetic and electron-electron terms are not known. In order to use this energy functional to minimise the energy, Kohn and Sham [125] made approximations for the unknown terms by introducing a system of N non-interacting electrons to be described by a single determinant wavefunction in N orbitals ϕ_i (called Kohn-Sham orbitals), in which the kinetic energy ($T_s[\rho]$, where the subscript s indicates this is the kinetic energy for a system with non-interacting electrons) and electron density are easily calculable, and the electron density is the same as in the un-approximated system. The energy functional is therefore re-written as a Kohn-Sham expression:

$$E[\rho] = T_s[\rho] + V_{ext}[\rho] + V_H[\rho] + E_{xc}[\rho] \tag{2.13}$$

where $V_H[\rho]$ is the Hartree energy and $E_{xc}[\rho]$ is the *exchange-correlation functional*. The exchange and correlation functional is essentially the sum of the error produced when using the non-interacting kinetic energy and applying classical treatment of the electron-electron interaction (Hartree energy). It can be defined as:

$$E_{xc}[\rho] = (T[\rho] - T_s[\rho]) + (V_{ee}[\rho] - V_H[\rho]) \tag{2.14}$$

The exchange-correlation functional is therefore the only unknown in the calculation of the DFT energy and a precise description of the functional becomes the most important factor in influencing the accuracy of DFT calculations, such that various DFT methods are commonly separated by the type of approximation for the exchange-

correlation functional.

The exchange-correlation energy can be split into two different parts, both of which emerge as a result of the behaviour of electrons in the quantum mechanical system. The exchange term is related to the energy that is classically described by the Coulomb equation, for the repulsion of electrons avoiding each other due to their electric charges. However, if we consider this repulsion with regards to the Pauli exclusion principle, which states that no two identical electrons can occupy the same quantum state simultaneously and therefore indicates that the total wavefunction must change sign (be antisymmetric) if any two electrons are interchanged, then we can assign a quantum mechanical correction for the exchange energy. The correlation term, on the other hand, is purely related to the effect where electrons avoid each other due to their normal motion, an energy which is calculated by wave mechanics methods [126].

The description of the functional for the exchange-correlation energy is crucial in accurately describing a system in DFT, yet, explicitly defining the form of the functional is very difficult with the exception of special cases such as a uniform electron gas. In hope of approximating the functional accurately, the properties that are exhibited by the exact functional are commonly used as guides. From these, one of the most important is that the exchange energy and the Coulomb energy should exactly cancel in a one-electron system, which gives a zero correlation energy (i.e. there are no self-interaction contributions to the energy). This can seem to be quite a simple and obvious rule, but the fact is that none of the commonly used approximations have this property.

One of the first types of approximations that was developed for DFT was the local density approximation (LDA) [125]. In this case the density is treated locally as a uniform electron gas (Jellium) for which electron-electron interaction are approximated using the classical Hartree potential. This allows the total energy to be easily computed, and subsequently the dependence of the kinetic and exchange energy on the density of the electron gas is readily extracted and expressed terms of local functions of the density [118, 119, 127, 128]. It followed that then for a inhomogeneous system the functional could be approximated as an integral over a local function of the charge density, suggesting an approximation that the local exchange-correlation energy per electron could be a function of the local charge density:

$$E_{xc}[\rho] \approx \int \rho(\mathbf{r})\varepsilon_{xc}(\rho(\mathbf{r}))d\mathbf{r} \tag{2.15}$$

where we take $\varepsilon_{xc}(\rho)$ to be the exchange and correlation energy density of Jellium ρ.

The LDA has proven to be particularly useful in the development of DFT and has been able to provide accurate descriptions of various properties such as structural parameters, vibrational frequencies, elastic moduli and phase stability for a number of materials. The properties of metallic systems in particular are described very well as their delocalised electron system is similar to that of the Jellium. Part of the reason that the LDA performs so well despite its somewhat poor representation of exchange and correlation energies for inhomogeneous systems is due to a systematic self-cancellation of errors. The exchange energy is generally underestimated by $\sim 10\%$ while the correlation energy is overestimated by about a factor of 2, which cancels itself out. Additionally, the fact that the electron-electron interaction in the Coulomb operator is dependent on only the spherical average of the exchange hole, which is represented quite well in the LDA (and ensuring a normalisation to -1) further explains the good performance. [119]

The LDA generally runs into the most difficulty when describing the binding energies in various systems, the local exchange potential does not consider the electronic redistribution in bonds and often the bond strengths are overestimated. In addition, the band gaps for systems described by the LDA are usually underestimated, which is exacerbated in systems that are strongly dependent on electron correlation effects. Naturally, any improvement to the LDA must take into account the fact that the density varies in the local energy expression of inhomogeneous systems. This can be implemented by adapting the functional to depend on not only the electron density but also its gradient ($\nabla\rho$). These adaptations of the LDA are commonly known as Generalised Gradient Approximations (GGAs) and have the form:

$$E_{xc} \approx \int \rho(r)\varepsilon_{xc}(\rho, |\nabla\rho|)d\mathbf{r} \tag{2.16}$$

Additionally, the GGA functionals have been modified further to include information on the local kinetic energy density (τ) or the Laplacian of the spin density ($\nabla^2\rho$) and are named meta-GGAs. These improvements have altogether resulted in an better description of the bonding and binding energies of molecules than before; however, the problem with self-interaction in heavily localised systems such as ionic solids still remains [129–131]

Thus, one of the most significant advancements in the approximation to exchange-correlation could be the development of hybrid exchange functionals. These implement the adiabatic connection approach, in which the functional depends on the variation of the density-density correlation function with the coupling constant λ [132]. At $\lambda = 0$ the non-interacting system is equal to the Hartree-Fock ansatz and moving up to $\lambda = 1$,

it becomes the equivalent to fully-interacting systems of LDA and GGA functionals. Therefore, by approximating the exchange-correlation energy as a weighted sum of the coupling constant end points, we are able to obtain a hybrid of the Hartree-Fock and DFT exchange functionals, i.e.:

$$E_{xc} \approx aE_{Fock} + bE_{xc}^{\mathrm{GGA}} \tag{2.17}$$

where a and b are coefficients that can be assigned optimally depending on the requirement of the system. One method of assigning these coefficients is by a fit to observed experimental data. A particularly useful functional developed by Becke implemented such a method by using the atomisation energies, ionisation potentials, proton affinities and the total atomic energies for a set of small molecules to fit three coefficients [133]. The resulting exchange-correlation approximation they proposed was:

$$E_{xc} = E_{xc}^{\mathrm{LSDA}} + a(E_x^{exact} - E_x^{\mathrm{LSDA}}) + b\Delta E_x^{\mathrm{B88}} + c\Delta E_c^{\mathrm{PW91}} \tag{2.18}$$

where a, b, and c are the fitted coefficients, $\Delta E_x^{\mathrm{B88}}$ is Becke's 1988 gradient correction for exchange, and $\Delta E_c^{\mathrm{PW91}}$ is Perdew and Wang's gradient correction for correlation. The superscript LSDA simply refers to the local spin density approximation, which substitutes the density in the LDA with the density of a spin polarised inhomogeneous electron gas. This type of hybrid functional led to now widely used B3LYP (Becke, three-parameter, Lee-Yang-Parr) functional, which is identical to Eq. 2.18 except for the update of gradient correction for correlation with the Lee-Yang-Parr version [129].

The B3LYP hybrid correlation-exchange functional has proven to be very accurate in reproducing binding energies, geometries and vibrational frequencies for a broad range of molecules and solid-state materials, with a significant improvement over previous approximations [130]. The incorporation of a $\sim 20\%$ Fock exchange is the main factor behind the improvement, since it compensates for some of the self-interaction error. Additionally, the combination of non-local and semi-local exchange potentials increases the range of materials that can be described effectively since more levels of electron localisation can be described. There are however some areas where functionals such as B3LYP, which have coefficients fitted in order to give good agreement with experimental data, might encounter problems. This could occur when systems which do not resemble those used to fit the coefficients are modelled, i.e the fitting data is usually taken from molecular systems and therefore when modelling periodic systems such as crystals the results may not be so good [126]. In these cases functionals that implement free parameters (non empirical methods) to fulfill the requirements of the ex-

act exchange-correlation functional might perform better. Amazingly though, B3LYP works well in very large range of systems, and it is often the heavily parameterised GGA and meta-GGAs that are less transferable [65].

2.2 The Periodic Model

When studying crystalline systems, the use of DFT under periodic boundary conditions is convenient. Crystalline systems can be described as an infinite repetition of a *unit cell* in three dimensions, i.e. an indefinitely extended lattice of periodically repeating points. The real crystal will of course terminate with a surface; however, at the macroscopic scale the ratio of atoms at the surface to those in the bulk is minute and for a neutral surface the perturbation that they cause only affects a few surface layers, meaning that a macroscopic crystal largely exhibits properties of the bulk rather than the surface. This justifies the periodic model of an infinite crystal when the study only concerns the bulk properties (ignoring surface effects). However, periodicity is also seen when studying polymers (one dimensional) and surfaces (two dimensions), systems for which the periodic boundary conditions must be restricted to one or two dimensions of the unit cell.

The unit cell for all of these systems can be defined using the vectors $\mathbf{a}_1$, $\mathbf{a}_2$ and $\mathbf{a}_3$ and the angles α, β and γ, which classify the unit cells into the seven lattice systems: Cubic, Hexagonal, Tetragonal, Rhombohedral, Orthorhombic, Monoclinic and Triclinic. These unit cells differ in their relative lengths, vectors and angles, and are occupied by atoms in various positions inside the cells (corners, sides, centre and face). The occupancy of a unit cell by atoms results in additional classification of the unit cells into a total of 14 possible *Bravais lattice* types. The periodic systems that are used for our QM calculations can be generated from Bravais lattices such as these by a translation of the unit cell by lattice vectors $\mathbf{t}$. This of course also encompasses more complicated lattices that are classified by any of the 230 space groups generated by all the possible symmetry operations.

The (direct) lattice of the periodic system will inherently have a reciprocal lattice, which has the vectors $\mathbf{b}_1$, $\mathbf{b}_2$ and $\mathbf{b}_3$ that obey the orthogonality rule with respect to the direct lattice:

$$\mathbf{a}_i.\mathbf{b}_j = 2\pi\delta_{ij} \tag{2.19}$$

This means that the reciprocal lattice vectors are orthogonal to the direct lattice

vectors when the indices are unequal (δ_{ij} is 1 if i equals j and 0 when i is different from j) and that all reciprocal lattice vectors are normalised to 2π . The reciprocal lattice points can be expressed similarly to how vectors $\mathbf{r}$ describe points in the direct lattice, using the vectors $\mathbf{k}$ (i.e $\mathbf{k}$ points). The primitive cell (the minimum or fundamental cell with respect to translational symmetry) made up from such vectors in the reciprocal space is known as the *first Brillouin zone* [134]. The vector $\mathbf{k}$ is often referred to as a wave vector since it has units of inverse length. In fact it is linked to momentum and energy when we describe a free particle using a plane wave of the form $e^{i\mathbf{k}.\mathbf{r}}$, which gives the momentum as k and the kinetic energy as $\frac{1}{2}k^2$. The importance of this description of the primitive cell in reciprocal space stems from the Bloch wave description of waves in a periodic medium, in which it is apparent that the solutions can be determined by their behaviour in a single Brillouin zone.

As an example, consider that in order to be able to solve the Schrödinger equation for a periodic system, we must adapt our description of the system so that we do not have to carry out calculations for the infinite number of atoms. If we begin by considering that nuclei of such a system are arranged periodically, then there simply must be a periodic charge density (ρ) that is associated with them, and can be written (in one dimension) as:

$$\rho(x + na) = \rho(x) \tag{2.20}$$

where n is an integer and a indicates the distance between repeated nuclei. Since the charge densities repeated along the periodic lattice system are all equivalent, and the charge density is simply the square of the wavefunction, it is easy to transcribe Eq. 2.20 as:

$$|\psi(x + na)|^2 = |\psi(x)|^2 \tag{2.21}$$

and when $n = 1$,

$$\psi(x + a) = e^{ika}\psi(x) \tag{2.22}$$

where ψ represents the crystalline orbital, and the complex phase factor e^{ika} is used to relate the wave function value at equivalent positions in neighbouring cells [135]. This formula is often expressed in three dimensions as:

$$\psi(\mathbf{r} + \mathbf{t}) = e^{i\mathbf{k}\cdot\mathbf{t}}\psi(\mathbf{r}) \tag{2.23}$$

and is called the *Bloch theorem*, where the complex phase factor involves the lattice vector $\mathbf{t}$ and a vector in the reciprocal space [126]. This theorem can also be re-written for the nth band in a unit cell using a wave-like part and a cell-periodic part (φ), more commonly known as the *Bloch function*:

$$\psi_{n,k}(\mathbf{r}) = e^{i\mathbf{k}\cdot\mathbf{r}}\varphi_n(\mathbf{r}) \tag{2.24}$$

The introduction of the Bloch function ultimately allows us to exploit the translational symmetry of the periodic system so that the problem, which initially required us to solve the Shrödinger equation for an infinite system, is now one where we must only solve it for the electrons in a single unit cell at an infinite number of $\mathbf{k}$ points in the Brillouin zone. In fact, it is not even necessary to solve this problem at an infinite number of $\mathbf{k}$ points, an approximate solution using a finite number of equally spaced $\mathbf{k}$ points (since the eigenvectors are continuous in k space) is actually sufficiently accurate to solve the critical matrix equation of DFT:

$$\mathbf{FC} = \mathbf{SCE} \tag{2.25}$$

where $\mathbf{F}$ is the Hamiltonian matrix, $\mathbf{C}$ and $\mathbf{E}$ are the eigenvector and eigenvalue matrices to be determined and $\mathbf{S}$ is the overlap matrix (the procedure for solving this is detailed in the following section). In order to account for the introduction of a Bloch function basis set, the equation takes the form:

$$\mathbf{F^kC^k} = \mathbf{S^kC^kE^k} \tag{2.26}$$

where the size of the matrices is equal to the number of atomic orbitals (Bloch functions) in the basis and the eigenvector or coefficient matrix $\mathbf{C^k}$ is constrained by the orthonormalisation condition ($\mathbf{I}$ is the identity matrix) [134]:

$$\mathbf{C^kS^kC^{\dagger k}} = \mathbf{I} \tag{2.27}$$

In order to distribute $\mathbf{k}$ points in the Brillouin zone, it is necessary to use a scheme, such as that suggested by Pack and Monkhorst [136, 137]. In this scheme the $\mathbf{k}$ points are allocated on a grid that has a size according to the "shrinking factor" $\mathbf{IS}$. The $\mathbf{IS}$ determines the number of equidistant $\mathbf{k}$ points to be taken along each direction inside one reciprocal lattice unit cell so that the total number of points is equal to $\mathbf{IS}^n$, where n is the order of periodicity. Other schemes also exist but, in general, the provision of a larger number of $\mathbf{k}$ points for reciprocal space integration allows for higher accuracy

in the solution to Eq. 2.29 and the calculation of the properties of the system.

2.3 The CRYSTAL Program

For this work, the simulations of $LaMnO_3$ and its related oxides are carried out using the CRYSTAL09 program [138]. The periodic model and several other processes, which will be described here, are implemented in CRYSTAL09 in order to determine the total energy of a system and its various properties.

The operation of the program can be separated into certain specific parts which are run in sequence. The following are the main steps for the calculations of a periodic system [134, 138]:

- Define an input deck which contains all of the necessary structural information of the system, the basis set to be used and the computational parameters.

- Form the basis of Bloch functions as linear combinations of the local basis of the atomic orbitals and evaluate the overlap matrix ($\mathbf{S^R}$) in the local basis set (real space):

$$\mathbf{S}^{\mathbf{R}}_{\mu\nu} = \int \psi_\mu(\mathbf{r})\psi_\nu(\mathbf{r}-\mathbf{g})d\mathbf{r} \tag{2.28}$$

  The indices μ and ν specify the two AO (ψ) and $\mathbf{g}$ is the direct lattice vector labelling the cell where the ν-th AO is centered while AO μ is always centered in the 0-cell.

- Evaluate the Fock (or Kohn-Sham) matrix in real space ($\mathbf{F^R}$) in the local basis set:

$$\mathbf{F}^{\mathbf{R}}_{\mu\nu} = \int \psi_\mu(\mathbf{r})\hat{F}(\mathbf{r})\psi_\nu(\mathbf{r}-\mathbf{g})d\mathbf{r} \tag{2.29}$$

  The average value of the Fock operator can be calculated as a sum of the contributions from the kinetic energy terms $\mathbf{T}^{\mathbf{R}}_{\mu\nu}$, electron-nuclear interactions $\mathbf{Z}^{\mathbf{R}}_{\mu\nu}$ and electron-electron Coulomb $\mathbf{C}^{\mathbf{R}}_{\mu\nu}$ and exchange $\mathbf{X}^{\mathbf{R}}_{\mu\nu}$ interactions:

$$\mathbf{F}^{\mathbf{R}}_{\mu\nu} = \mathbf{T}^{\mathbf{R}}_{\mu\nu} + \mathbf{Z}^{\mathbf{R}}_{\mu\nu} + \mathbf{C}^{\mathbf{R}}_{\mu\nu} + \mathbf{X}^{\mathbf{R}}_{\mu\nu} \tag{2.30}$$

- Represent the $\mathbf{S^R}$ and $\mathbf{F^R}$ matrices in the Bloch function basis set at every $\mathbf{k}$ point in the reciprocal space by Fourier transformation, then diagonalise to obtain the eigenvalues and eigenvectors, and solve the matrix equation (Eq. 2.29).

- Determine the Fermi energy (the highest occupied state in the system inside the first Brillouin zone) and build a new density matrix in the direct space $\mathbf{P}^{\mathbf{R}}_{\mu\nu}$:

$$\mathbf{P}^{\mathbf{R}}_{\mu\nu} = \frac{1}{V_{BZ}} \sum_j \int_{BZ} c^*_{\mu j}(\mathbf{k}) c_{\nu j}(\mathbf{k}) \theta(\varepsilon_F - \varepsilon_j(\mathbf{k})) e^{i\mathbf{k}.\mathbf{R}} d\mathbf{k} \tag{2.31}$$

  where the sum over $\mathbf{k}$ points is an integral over the first Brillouin zone with a volume V_{BZ}. The integration is limited to states with energy below the Fermi energy ε_F and a Heaviside step function θ excludes the eigenvectors relative to empty states from the sum. ε_j is the j-th eigenvalue and $c_{\mu j}$ refers to the μ-th component of the j-th eigenvector.

- Determine the total energy of the system (per cell) E_{tot} and reconstruct $\mathbf{F^R}$ matrix, repeating the steps that follow in an iterative cycle until self-consistency is achieved (known as the self consistent field calculation, SCF). In CRYSTAL09 this is determined by the difference in the total energy between cycles reaching the threshold specified in the input deck.

$$E_{tot} = \frac{1}{2} \sum_{\mu,\nu} \sum_{\mathbf{R}} \mathbf{P}^{\mathbf{R}}_{\mu\nu} \mathbf{H}^{\mathbf{R}}_{\mu\nu} \tag{2.32}$$

- Finally the converged wavefunction from the completed SCF procedure can be used to calculate various properties such as the density of states, band structure and charge densities.

The convergence of the SCF as described in the steps above can be accelerated through the use of certain schemes that are implemented in CRYSTAL09. A relatively simple scheme is linear mixing, where the Fock/Kohn-Sham matrix is updated at each iteration by adding a part (m) of the input matrix of the n-th cycle to that of the $n+1$-th cycle, in order to improve the guess of $\mathbf{F}^{in}_{n+1}$

$$\mathrm{F}^{in}_{n+1} = (1-m)\mathrm{F}^{out}_n + m\mathrm{F}^{in}_n \tag{2.33}$$

The amount of mixing, m, is set at the beginning of the calculation and depends on type of system being studied. Anderson and Broyden mixing schemes, which are

also available in CRYSTAL09, use more complex quadratic or higher-order mixing schemes in order to increase the numerical stability and can further reduce the number SCF cycles required to converge the calculations. However, when using the various mixing schemes it is essential to use the appropriate amount of mixing in order to avoid constraining the total energy of the system.

2.4 Geometry Optimisation

In order to determine the equilibrium or stable geometry of the systems we are studying it is necessary to perform a geometry optimisation where the structure with the lowest total energy is sought. This is done by exploring the total energy minima along the potential energy surface (PES), often a very computationally expensive task, the complexity of which is reduced by starting the optimisation with good initial guess of the geometry. The minima are typically determined using first and second derivatives, where the first derivatives find the stationary points on the PES and the second derivatives allow us to characterise them [139].

There are a number of techniques available that enable us to solve this complex multidimensional minimisation problem, which involves the optimisation of a large number of degrees of freedom [140]. From among these the most straightforward is known as the *Steepest Descent* method, where the system is driven towards the minimum of the energy function $E(x)$, by progressing downwards along the gradient calculated at each point. In basic terms the direction being searched $\mathbf{d}$ is simply the negative direction of the gradient $\mathbf{g}$, where $\mathbf{g}_\mathrm{i} = \frac{\delta E}{\delta \mathrm{x}_i}$ and the step size is either fixed or dependant on the magnitude of the gradient. This method will always reach a minimum but the convergence can be very slow.

Another technique which is only slightly more complex is known as the *Conjugant Gradient* method. This converges to the minimum faster and works by searching along a direction at step n that is a mixture of the current gradient and the previous search directions $\mathbf{d}_{n-1}$:

$$\mathbf{d}_n = -\mathbf{g}_n + \beta_n \mathbf{d}_{n-1} \tag{2.34}$$

where β is a coefficient that determines the level of mixing. Simply put this technique makes use of the gradient history to determine a better direction for the next step.

While the methods mentioned above function quite well, they can be very slow in

non-linear systems. Most modern atomistic simulation software packages implement a version of the *Newton-Raphson* method [141]. This method will converge to the nearest stationary point with a very low number of steps, but can be quite expensive in terms of computation.

The speed of this method arises due to its calculation of the Hessian (the second derivative matrix), $\mathbf{H}_{ij} = \frac{\delta^2 E}{\delta x_i \delta x_j}$, which allows it to predict the distance to the stationary point from the current geometry, and also the nature of the stationary point upon arrival. The minimum can be verified when all of the eigenvalues obtained from diagonalisation of the Hessian are real and positive (i.e. a positive definite Hessian), otherwise the stationary point with N amount of negative eigenvalues is an N-th order transition state.

In practice, the region around any given point of the PES is expressed in terms of a Taylor expansion:

$$E(\mathbf{x}_{n+1}) = E(\mathbf{x}_n) + \mathbf{g}_n(\mathbf{x}_{n+1} - \mathbf{x}_n) + \frac{1}{2}\mathbf{H}_n(\mathbf{x}_{n+1} - \mathbf{x}_n)^2 \tag{2.35}$$

where $\mathbf{x}_n$, $\mathbf{g}_n$ and $\mathbf{H}_n$ are the coordinate vector, gradient vector and Hessian matrix for the reference point n. Differentiating this expansion with respect to the i-th coordinate of $\mathbf{x}_{n+1}$, and incorporating the condition that for any stationary point the gradient $\mathbf{g} = 0$ we obtain:

$$0 = \mathbf{g}_n + \mathbf{H}_n(\mathbf{x}_{n+1} - \mathbf{x}_n) \tag{2.36}$$

which can be rearranged to:

$$\mathbf{x}_{n+1} = \mathbf{x}_n - (\mathbf{H}_n)^{-1}\mathbf{g}_n \tag{2.37}$$

giving a formula that allows for the determination of stationary points. Generally if we start from an arbitrary structure with coordinates $\mathbf{x}_n$ and compute its gradient vector $\mathbf{g}$ and Hessian matrix $\mathbf{H}$, we would be able to select a new geometry $\mathbf{x}_{n+1}$ which, according to Eq. 2.36 and Eq. 2.37, should be a stationary point as long as $E(\mathbf{x})$ is a quadratic function such as when the potential energy surface is harmonic. This is due to the truncation of the Taylor expansion (Eq. 2.35) at the second order term.

However, if it is not quadratic, then Eq. 2.36 is only an approximation and $\mathbf{g}_{n+1}$ is not necessarily 0. In this case $\mathbf{g}_{n+1}$ is still likely to be less than $\mathbf{g}$ and through successive iterations of the above process the gradient should become so small that the differences between the structures at point $k + n$ and $k + n + 1$ are chemically insignificant (a

threshold we can define in our CRYSTAL09 software) and we can consider the geometry to be converged.

The only real drawback of Newton-Raphson methods is that it is only able to find local minima and that the construction and inversion of the Hessian matrix can be very expensive. In order to reduce the cost there are some methods to approximate the Hessian using the gradient history and therefore not compute the expensive analytic Hessian at every step. In CRYSTAL09 the Broyden-Fletcher-Goldfarb-Shanno (BFGS) algorithm is used, which can reduce the cost to that of the steepest descent method **??**.

2.5 Computational Methods Applied to $LaMnO_3$

As discussed in the previous section, a variety of methods have been developed for the modelling of a range of systems. From among these methods, there are many which are specialised towards the study of a particular set of systems, while at the same time those methods can be highly inaccurate for any other system. For this work it is, therefore, crucial to choose a method that is suitable for the study of orthorhombic $LaMnO_3$ in its ground state.

$LaMnO_3$ could be considered a *strongly correlated material* since the properties it exhibits are due to strong electron-electron interactions. As a consequence, any simulation of $LaMnO_3$ must include electron correlation to be able to reproduce its properties accurately. In particular, the ground state of $LaMnO_3$ has an AAF orthorhombic orbitally-ordered structure, where the Mn-O octahedra are J-T distorted (see Sec. 1.3.1). Furthermore, the structural parameters and electronic properties simulated should also be in quantitative agreement.

In order to ensure the accuracy of our computational methods, it is desirable to make a comparison against results from experiment. However, the comparison of properties that are calculated with those observed experimentally is limited by the fact that simulations will typically study an 'ideal' model of a system, whereas in reality the crystal structure from which experimental data is obtained may contain defects and impurities that are not easily defined and vary with each sample. This is further complicated by the fact that certain electronic properties, such as the band gap, are not measured directly but are approximated. The end result is that we can not reliably estimate the level of accuracy provided by each method, since we do not know if the data obtained from our simulations is directly comparable to the data obtained from actual systems. In this case the best scenario is to assess the accuracy of each method for systems that are 1) similar to that which we wish to investigate and 2) we know are

comparable to the simulations.

As discussed in the previous chapter, the electronic structure of $LaMnO_3$ has been studied in the past with a variety of methods. The band structure has been calculated using the LDA, but the results indicate that the insulating cubic phase is a conductor and the predicted band gap for the orthorhombic phase is too small [59]. These results are not too surprising though since in many narrow band systems the LDA fails to predict the electronic ground state properly [142, 143].

Use of the GGA of the exchange-correlation should improve the description of the electronic properties of $LaMnO_3$, however, evidence from previous work indicates some of the discrepancies of the LDA are inherited [144]. Recently the LDA/GGA $+U$ method has been used to study $LaMnO_3$ [145]. This approach typically improves on the predicted band gaps and lattice constants of many systems similar to $LaMnO_3$, by addressing the on-site Coulomb interactions in the localised orbitals (i.e the Mn $3d$ orbitals) with an additional Hubbard U, leading to partial compensation of the self-interaction error [146,147]. Although this method significantly improves the description of $LaMnO_3$, it is not ideal since the energetics are highly dependant on the choice of an optimal U, which is not consistent for the range of systems investigated in this work [111, 145]. GGA $+U$ also incorrectly predicts the reactivity of $LaMnO_3$ surfaces, which are likely to contain varying valence states of Mn, each requiring a different choice of U [75].

There has also been growing interest in the use of hybrid functional methods that typically use a combination of exact nonlocal HF exchange and a standard exchange-correlation functional. The study of a series of Mn oxides using the hybrid PBE0 and HSE functionals predicts structural parameters that yield volumes within 1% of experimental values. This is in contrast to the $+U$ methods discussed earlier which overestimate these by up to 7%. Another hybrid functional, B3LYP, has been used extensively in recent years, and has shown in a number of studies that it reliably reproduces the properties of various strongly correlated materials, particularly for transition metal oxides [63, 65, 148–154]. In particular, for $LaMnO_3$, the B3LYP functional has been shown to provide a reasonable estimate of the band gap and the nature of the states near the Fermi energy, where both the Mn $3d$ and O $2p$ states show similar contributions [63]. This prediction of the density of states is in line with the picture of the Mn-O chemical bond in which both the ionic and covalent (orbital mixing between metal and ligand) contributions are considered.

In summary, the hybrid functionals have been able to predict the properties of strongly correlated materials with the greatest accuracy. From among these methods,

the B3LYP functional is a suitable choice to study $LaMnO_3$ as there have been a sufficient quantity of studies showing that it is possible to obtain accurate data on the electronic structure of transition metal oxides. Furthermore, demonstrating the flexibility to study such a range of systems indicates it is also suitable for the study of $LaMnO_3$ surfaces, where the changes in Mn valence can be challenging for other methods.

2.6 Computational Details

All calculations have been performed using the CRYSTAL09 [138] code, based on the expansion of the crystalline orbitals as a linear combination of a local basis set (BS) consisting of atom centred Gaussian orbitals. The Mn and O ions are described by a triple valence all-electron BS: an 86-411d(41) contraction (one *s*, four *sp*, and two *d* shells) and an 8-411d(1) contraction (one *s*, three *sp*, and one *d* shells), respectively; the most diffuse *sp*(*d*) exponents are α^{Mn}=0.4986(0.249) and α^{O}= 0.1843(0.6) Bohr^{-2} [155]. The La basis set includes a pseudopotential to describe the core electrons, while the valence part consists of a 411p(411)d(311) contraction scheme (with three *s*, three *p* and three *d* shells); the most diffuse exponent is α^{La}=0.15 Bohr^{-2} for each *s*,*p* and *d* [63]. Full details of the basis sets used can be found in appendix A.

Electron exchange and correlation are approximated using the B3LYP hybrid-exchange functional, which, as noted above, is expected to be more reliable than the local density approximation (LDA) or generalised gradient approximation (GGA) approaches in this system [65, 148, 156]. The exchange and correlation potentials and energy functional are integrated numerically on an atom centred grid of points. The integration over radial and angular coordinates is performed using Gauss-Legendre and Lebedev schemes, respectively. A pruned grid consisting of 99 radial points and 5 sub-intervals with (146, 302, 590, 1454, 590) angular points has been used for all calculations (see the XXLGRID option in CRYSTAL09 [138]). This grid converges the integrated charge density to an accuracy of about 10^{-6} electrons per unit cell. The Coulomb and exchange series are summed directly and truncated using overlap criteria with thresholds of 10^{-7}, 10^{-7}, 10^{-7}, 10^{-7} and 10^{-14} as described previously [138,157]. Reciprocal space sampling was performed on a Pack-Monkhorst net with a shrinking factor of IS=8. The self consistent field procedure was converged up to a tolerance in the total energy of $\Delta E = 10^{-7} E_h$ per unit cell.

The cell parameters and internal coordinates have been determined by minimization of the total energy within an iterative procedure based on the total energy gradient

calculated analytically with respect to the nuclear coordinates. Convergence was determined from the root-mean-square (rms) and the absolute value of the largest component of the forces. The thresholds for the maximum and the rms forces (the maximum and the rms atomic displacements) have been set to 0.00045 and 0.00030 (0.00180 and 0.0012) in atomic units. Geometry optimization was halted when all four conditions were satisfied simultaneously.

3

The Thermodynamic Stability of $LaMnO_3$ and its Competing Oxides

3.1 Introduction

In Ch. 1 it is pointed out that, in order to reliably study the stability of $LaMnO_3$ surfaces, it is essential to establish the thermodynamic stability of the bulk (and also its competing oxides). This is not only necessary to define the chemical potential ranges for which surface stability needs to also to verify the accuracy of our computational methods with respect to available experimental data. The initial part of this work is, therefore, concerned with providing a reliable and accurate methodology with which the thermodynamic stability of $LaMnO_3$ can be established.

In recent literature there has been some effort to understand the thermodynamics of the bulk and surface of orthorhombic $LaMnO_3$, but a systematic and comprehensive study of the thermodynamics of $LaMnO_3$ and its competing oxides using DFT with the hybrid B3LYP functional has yet to be carried out [68, 70, 71]. In such works, the stability of competing oxides is visualised by the construction of a phase diagram that defines regions of chemical potential space where compounds can exist. These regions of stability are essentially defined by the Gibbs formation energies of the compounds, which can be calculated using DFT (this is discussed in detail in the following sections).

In the previous thermodynamic studies of $LaMnO_3$ and the competing Mn oxides, calculations of the Gibbs formation energies are affected by a significant error relative to experiment: the mean error ranges from 7 to 22% [71, 111]. This is due to the unique

energetics of these compounds that are characterised by a strong interplay between geometry and electronic structure; they require an accurate treatment of exchange and correlation for the description of electron localisation, which is is lacking in the GGA-type functionals adopted in previous work. This treatment is especially important in order to obtain a consistent set of formation as energies, as Mn adopts different valence states within its series of oxides, resulting in different fillings of the Mn d-band and therefore large variations in the on-site correlation.

In addition to the inaccuracy of certain functionals for the energetics of correlated systems, the imprecise calculation of Gibbs formation energies can also be attributed to the methodology adopted to calculate the chemical potentials of Mn and O. For instance, the standard GGA functional is not suitable for the calculation of the O potential since elemental O, which must be modelled to obtain the potential, is molecular and has well localised electrons that GGA cannot properly describe [119].

In this chapter, therefore, the first concern will be to devise a methodology that can accurately determine these chemical potentials. Subsequently, an investigation into the ground states of the competing oxides with regards to their geometry and magnetic state will be performed in order to ensure that the Gibbs formation energies calculated are for systems that are representative of those observed experimentally. After making these careful preparations a precise phase diagram will be constructed from the Gibbs formation energies of the various competing oxides in order to define their regions of stability. The results will be compared to previous literature and experimental data in order to evaluate the quality of our methods, after which the progress made in this chapter will be summarised. The computational details for the calculations carried out in this chapter are already provided in Sec. 2.6.

3.2 *Ab Initio* Thermodynamics

In this section, the methodology used to construct the phase diagram is described. This relies on the calculation of the Gibbs formation energies ΔG_f^0 of all of the involved compounds, which in turn requires the determination of the standard chemical potentials of the elements μ^0. The methods for calculating both of these are discussed below

3.2.1 Standard chemical potentials

We will generally neglect entropic and volumetric work contributions to the Gibbs energy and approximate G with the total energy E at 0 K as given by DFT. This is well

justified for solids in the temperature and pressure range of interest, because the entropic contribution is mainly vibrational and the volume of solids is nearly independent of pressure and temperature. Hence, these terms are small and tend to cancel [158]. The reference state for oxygen, however, is the gaseous dimer and needs further consideration. The Gibbs energy of an (ideal) gas contains significant translational and rotational entropy as well as volumetric work.

The following expression (which is derived below) for the oxygen chemical potential as a function of of p_{O_2} and T reflects this [159]:

$$\mu_{O_2}(p_{O_2}, T) = E_0 + (\mu^0_{O_2} - E_0)\frac{T}{T^0} - \frac{5k_B}{2}T\ln\left(\frac{T}{T^0}\right) + k_B T \ln\left(\frac{p_{O_2}}{p^0_{O_2}}\right) \tag{3.1}$$

This expression contains two unknown quantities: E_0, the energy per O_2 molecule at 0K and $\mu^0_{O_2}$, the chemical potential of an O_2 molecule at standard conditions (where superscript 0 indicates standard conditions: $T^0 = 298.15$K and $p^0_{O_2} = 1$bar). E_0 can be reliably calculated using the B3LYP functional with DFT as outlined in Ch. 2, while $\mu^0_{O_2}$ is normally estimated using experimental data. Since we need $\mu^0_{O_2}$ rather than $\mu_{O_2}(p_{O_2}, T)$ to calculate the Gibbs formation energies, it is useful to adapt this expression for this purpose. This can be achieved by a derivation that involves a combination of the above expression with the Shomate equation, described in detail in the following sections.

Derivation from classical thermodynamics

Before introducing the Shomate equation, it is useful to explain the origin of the expression for the chemical potential of the oxygen, $\mu_{O_2}(p_{O_2}, T)$, for a particular oxygen pressure and temperature (Eq. 3.1). This involves a manipulation of the standard thermodynamic relation for perfect gases and the Gibbs-Helmholtz relation, as demonstrated previously by Johnston and coworkers [159]. The derivation begins with the standard thermodynamic relation for O_2:

$$\left.\frac{\partial \mu_{O_2}}{\partial p}\right|_T = \frac{k_B T}{p} \tag{3.2}$$

this is integrated from $p^0_{O_2} = 1$ atm up to a pressure p_{O_2} with a constant temperature T in order to obtain the expression:

$$\mu_{O_2}(p_{O_2}, T) = \mu_{O_2}(p^0_{O_2}, T) + k_B T ln\left(\frac{p_{O_2}}{p^0_{O_2}}\right) \tag{3.3}$$

to which we can apply the Gibbs-Helmholtz relation in order to derive temperature dependence:

$$\frac{\partial}{\partial T}\left(\frac{\mu_{O_2}}{T}\right)_p = -\frac{H}{T^2} \tag{3.4}$$

where H is the enthalpy per oxygen molecule. If we assume that we are dealing with a classical ideal gas, we can also express H in terms of T since:

$$H = E_0 + C_p T \tag{3.5}$$

where E_0 is the energy per molecule at 0 K and C_p is the specific heat capacity per molecule at constant pressure, equal to $\frac{5k_B}{2}$ for a diatomic gas composed of rigid dumbbells. If we then integrate Eq. 3.4 from T^0 to T we can finally obtain the expression in Eq. 3.1 for the chemical potential of oxygen, $\mu_{O_2}(p_{O_2}, T)$, for a particular oxygen pressure and temperature.

$$\mu_{O_2}(p_{O_2}, T) = E_0 + (\mu^0_{O_2} - E_0)\frac{T}{T^0} - \frac{5k_B}{2} T \ln\left(\frac{T}{T^0}\right) + k_B T \ln\left(\frac{p_{O_2}}{p^0_{O_2}}\right) \tag{3.1}$$

Derivation from the Shomate equation

The Shomate equations, which are a polynomial fit to observed thermodynamic quantities (and are justified empirically), define the standard enthalpy H^0 and standard entropy S^0 as [160]:

$$H^0(t) = H^0 + At + B\frac{t^2}{2} + C\frac{t^3}{3} + D\frac{t^4}{4} - \frac{E}{t} + F - H \tag{3.6}$$

$$S^0(t) = A\ln(t) + Bt + C\frac{t^2}{2} + D\frac{t^3}{3} - \frac{E}{2t^2} + G \tag{3.7}$$

where t = T/1000 and the coefficients A-G are given in Table 3.1. If we consider that the standard Gibbs energy is given by the relationship:

$$G^0(t) = H^0(t) - tS^0(t) \tag{3.8}$$

then we are able to obtain an expression for $\mu_{O_2}(p_{O_2}, T)$:

$$G^0(t) = H^0 + At + B\frac{t^2}{2} + C\frac{t^3}{3} + D\frac{t^4}{4} - \frac{E}{t} + F - H - t(A\ln(t) + Bt + C\frac{t^2}{2} + D\frac{t^3}{3} - \frac{E}{2t^2} + G) \tag{3.9}$$

$$G^0(t) = H^0 + A(t - t\ln(t)) + B(\frac{t^2}{2} - t^2) + C(\frac{t^3}{3} - \frac{t^2}{2}t) + D(\frac{t^4}{4} - \frac{t^3}{3}t) - E(\frac{1}{t} - \frac{1}{2t^2}t) + F - Gt - H \tag{3.10}$$

$$G^0(t) = H^0 + A(t - t\ln(t)) - B\frac{t^2}{2} - C\frac{t^3}{6} - D\frac{t^4}{12} - E\frac{1}{2t} + F - Gt - H \tag{3.11}$$

The quantity H^0 is an unknown and can be written as $G^0 + t^0S^0$ by exploiting the relation $G^0 = H^0 - t^0S^0$, giving us:

$$G^0(t) = G^0 + t^0S^0 + A(t - t\ln(t)) - B\frac{t^2}{2} - C\frac{t^3}{6} - D\frac{t^4}{12} - E\frac{1}{2t} + F - Gt - H \tag{3.12}$$

Finally, since the chemical potential of the system is equal to the Gibbs free energy per formula unit, we can convert the above equation into the form:

$$\mu^0_{O_2}(t) = \mu^0_{O_2} + t^0S^0 + A(t - t\ln(t)) - B\frac{t^2}{2} - C\frac{t^3}{6} - D\frac{t^4}{12} - E\frac{1}{2t} + F - Gt - H \tag{3.13}$$

which is more convenient as it shares the terms as Eq. 3.1.

Table 3.1: The parameters for the range 100 - 700 K [160] for O_2.

A	31.32234× 10^3	kJ/(mol K)
B	-20.23531× 10^6	kJ/(mol K^2)
C	57.86644× 10^9	kJ/(mol K^3)
D	-36.50624× 10^{12}	kJ/(mol K^4)
E	-0.007374× 10^{-3}	kJ K/mol
F	-8.903471	kJ/mol
G	246.7945	kJ/mol
H	0	kJ/mol

Calculation of O_2 chemical potential by Shomate method

As discussed earlier, we require the oxygen chemical potential at standard temperature and pressure, $\mu^0_{O_2}$ *. In order to overcome this problem an expression for the standard

* $\mu^0_{O_2} = \mu_{O_2}(p_{O_2} = p^0_{O_2}, T = T^0)$

potential is obtained by equating the derivatives of the formulas we have prepared in Eq. 3.1 and 3.13 (the Classical and Shomate expressions).

For Eq. 3.1, it follows that:

$$\left.\frac{\partial \mu_{O_2}(p_{O_2},T)}{\partial T}\right|_{p_{O_2}} = (\mu^0_{O_2} - E_0)\frac{1}{T^0} - \frac{5k_B}{2}\ln\left(\frac{T}{T^0}\right) - \frac{5k_B}{2} + k_B \ln\left(\frac{p_{O_2}}{p^0_{O_2}}\right) \tag{3.14}$$

and when the standard pressure is adopted this becomes:

$$\left.\frac{\partial \mu_{O_2}(p_{O_2},T)}{\partial T}\right|_{p_{O_2}=p^0_{O_2}} = (\mu^0_{O_2} - E_0)\frac{1}{T^0} - \frac{5k_B}{2}\ln\left(\frac{T}{T^0}\right) - \frac{5k_B}{2} \tag{3.15}$$

At the same time the first derivative of Eq. 3.13 is:

$$\frac{d\mu^0_{O_2}(t)}{dt} = +A(1 - \ln(t) - 1) - Bt - \frac{1}{2}Ct^2 - \frac{1}{3}Dt^3 + \frac{E}{2t^2} - G \tag{3.16}$$

$$= -A\ln(t) - Bt - \frac{1}{2}Ct^2 - \frac{1}{3}Dt^3 + \frac{E}{2t^2} - G \tag{3.17}$$

and in terms of T , since $t = \frac{T}{1000}$,

$$\frac{d\mu^0_{O_2}(T)}{dT} = \frac{d\mu^0_{O_2}(t)}{dt}\frac{dt}{dT} \tag{3.18}$$

Therefore, it can be written as:

$$\frac{d\mu^0_{O_2}(T)}{dT} = \frac{1}{1000}\left[-A\ln(t) - Bt - \frac{1}{2}Ct^2 - \frac{1}{3}Dt^3 + \frac{E}{2t^2} - G\right] \tag{3.19}$$

The quantity $\mu^0_{O_2}$ can finally be obtained by equating the derivatives of the Classical and Shomat equations (Eqs. 3.15 and 3.19):

$$\left.\frac{\partial \mu_{O_2}(p_{O_2},T)}{\partial T}\right|_{p_{O_2}=p^0_{O_2}} = \frac{d\mu^0_{O_2}(T)}{dT} \tag{3.20}$$

$$\mu^0_{O_2} = E_0 + T^0\left[\frac{5k_B}{2}\ln\left(\frac{T}{T^0}\right) + \frac{5k_B}{2} + \frac{1}{1000}\left(-A\ln(t) - Bt - \frac{1}{2}Ct^2 - \frac{1}{3}Dt^3 + \frac{E}{2t^2} - G\right)\right] \tag{3.21}$$

The Oxygen potential at standard temperature and pressure can therefore be calculated from Eq. 3.21 to give:

$$\mu^0_{O_2} = -4090.46eV$$

Oxide Method

The chemical potentials required for the phase diagrams can also be calculated by solving a system of simultaneous equations for the standard Gibbs energy of formation, ΔG^0_f, for the competing oxides and isolating the chemical potential required. For example, the procedure for the obtaining O_2 chemical potential is outlined below, where MnO and MnO_2 will be used for demonstration:

$$\Delta G^0_{f\mathrm{MnO}} = \mu^{bulk}_{\mathrm{MnO}} - \mu^{bulk}_{\mathrm{Mn}} - \frac{1}{2}\mu^0_{\mathrm{O_2}} \tag{3.22}$$

$$\Delta G^0_{f\mathrm{MnO_2}} = \mu^{bulk}_{\mathrm{MnO_2}} - \mu^{bulk}_{\mathrm{Mn}} - \mu^0_{\mathrm{O_2}} \tag{3.23}$$

These equations are combined such that the Mn chemical potential is eliminated. Equation 3.22 is simply subtracted from Eq. 3.23, which gives us:

$$\Delta G^0_{fMnO_2} - \Delta G^0_{fMnO} = \mu^{bulk}_{MnO_2} - \mu^{bulk}_{MnO} - \mu^0_{O_2} - -\frac{1}{2}\mu^0_{O_2} \tag{3.24}$$

$$\Delta G^0_{fMnO_2} - \Delta G^0_{fMnO} = \mu^{bulk}_{MnO_2} - \mu^{bulk}_{MnO} - \frac{1}{2}\mu^0_{O_2} \tag{3.25}$$

$$\frac{1}{2}\mu^0_{O_2} = \mu^{bulk}_{MnO_2} - \mu^{bulk}_{MnO} - \Delta G^0_{fMnO_2} + \Delta G^0_{fMnO} \tag{3.26}$$

This formula is now solvable as the ΔG^0_f energies are easily obtained from experimental data [99], while the chemical potential of the bulk oxides are equated to their internal DFT energies (this is a reasonable approximation for these oxides as discussed earlier). By eliminating the Mn chemical potential using this method, the O_2 chemical potential can be reliably calculated from easily obtainable experimental and simulated values.

Calculation of O_2 chemical potential by Oxide Method

In order to use the oxygen chemical potential obtained by this method for our phase diagram of the Mn oxides, it is necessary to average out the chemical potential obtained from the entire series of the manganese oxides and therefore every possible combination of their formulas for the standard Gibbs energy of formation of the oxides. The work

for this is trivial so the relevant simultaneous equations are listed in appendix B.6, and the averaged value of the oxygen chemical potential given by this method is:

$$\mu^0_{O_2} = -4090.19eV$$

which is in good agreement (+0.27 eV) with the oxygen chemical potential calculated using the Shomate method.

Calculation of La and Mn potentials by Oxide Method

The oxide method is actually preferred for the calculation of metallic reference states of La and Mn in this work due the use of the B3LYP functional. This functional contains exact Fock exchange, and therefore provides a poor approximation for metals. The general formula for the formation energies of these oxides is

$$\Delta G^0_{f\mathrm{M_xO_y}} = \mu^{bulk}_{\mathrm{M_xO_y}} - x\mu^0_{\mathrm{M}} - y\mu^0_{\mathrm{O}}, \tag{3.27}$$

where M and O are metal and oxygen in the oxide $\mathrm{M_xO_y}$, $\Delta G^0_{f\mathrm{M_xO_y}}$ is the standard Gibbs formation energy from experiment [99] and $\mu^{bulk}_{\mathrm{M_xO_y}}$ is the chemical potential (Gibbs energy) of the bulk oxide. Solving these formulae is very straightforward, for instance, μ^0_{La} can be obtained by simply introducing the value of $\mu^0_{\mathrm{O_2}}$ given by the Shomate method into the equation:

$$\Delta G^0_{f\mathrm{La_2O_3}} = \mu^{bulk}_{\mathrm{La_2O_3}} - 2\mu^0_{\mathrm{La}} - \frac{3}{2}\mu^0_{\mathrm{O_2}}, \tag{3.28}$$

where the potential for the bulk La_2O_3, $\mu^{bulk}_{\mathrm{La_2O_3}}$ can be equated to the ground state energy, as discussed previously [158].

In the case of the manganese oxides, the same approach can be applied; however, since there are several oxides, slightly different manganese chemical potentials arise. These values have to be averaged to provide a value to calculate the *ab initio* formation energies of the manganese oxides and $LaMnO_3$. A standard deviation of 0.10 eV in the set of values was obtained, indicating a good approximation of the energetics of the Mn oxides. A lower deviation is limited by the accuracy of the obtained ground states (i.e. the modelled Mn_3O_4 system does not consider non-collinear magnetism of an actual Mn_3O_4 crystal, see Sec. 3.3) and due to the fact that there is large difference in the valence states of manganese in its oxides. The standard deviation of the obtained Mn chemical potentials is, therefore, a good measure of the methods accuracy.

Using the oxide method, the calculated standard potential for La and averaged Mn

potential are:

$$\mu^0_{La} = -858.85eV$$

$$\mu^0_{Mn} = -31318.66eV$$

3.2.2 Phase Diagram

The region of chemical potential space where bulk $LaMnO_3$ is stable is defined by plotting the line of the equation for the formation of a bulk compound from its elements. For $LaMnO_3$ this equation is:

$$\mu_{La} + \mu_{Mn} + \frac{3}{2}\mu_{O_2} = \mu^{bulk}_{LaMnO_3} \tag{3.29}$$

When this line is plotted in chemical potential space (for the La-Mn-O system this is a three dimensional space with coordinates μ_{La}, μ_{Mn} and $\mu_{\mathrm{O_2}}$), it will have conditions defining the region in which the compound is stable. For instance, the quantities; μ^0_{La}, μ^0_{Mn} and $\mu^0_{\mathrm{O_2}}$ define the upper stability limits in terms of the chemical potentials μ_{La}, μ_{Mn} and $\mu_{\mathrm{O_2}}$ for any compound in the system.

Therefore it is true that:

$$\mu_i - \mu^0_i \leq 0, \tag{3.30}$$

where $i = \mathrm{La}, \mathrm{Mn}, \mathrm{O}$. Above these limits the compounds decompose into their constituent elements. These conditions can be used to introduce a change of variable $\Delta\mu_i = \mu_i - \mu^0_i$ to give

$$\Delta\mu_i \leq 0, \tag{3.31}$$

which is convenient for the construction of a phase diagram. For example, the equilibrium chemical potential of $LaMnO_3$ with respect to its elements, given by

$$\mu_{\mathrm{La}} + \mu_{\mathrm{Mn}} + \frac{3}{2}\mu_{\mathrm{O_2}} = \mu^{bulk}_{\mathrm{LaMnO_3}}, \tag{3.32}$$

can be expressed as

$$\Delta\mu_{\mathrm{La}} + \Delta\mu_{\mathrm{Mn}} + \frac{3}{2}\Delta\mu_{\mathrm{O_2}} = \Delta G^0_{f\mathrm{LaMnO_3}}, \tag{3.33}$$

by stoichiometrically subtracting μ^0_{La}, μ^0_{Mn} and $\mu^0_{\mathrm{O_2}}$ from both sides of Equation 3.32,

where the right hand side of this equation is replaced by the standard Gibbs energy of formation due to the relationship:

$$\Delta G^0_{f\mathrm{XY}} = \mu^{bulk}_{\mathrm{XY}} - \mu^0_{\mathrm{X}} - \mu^0_{\mathrm{Y}} \tag{3.34}$$

Finally, it is possible to introduce a lower limit for the chemical potentials due to the fact that the stoichiometrically weighted chemical potentials $\Delta\mu^0_{\mathrm{La}}$, $\Delta\mu^0_{\mathrm{Mn}}$ and $\Delta\mu^0_{\mathrm{O_2}}$ must sum to $\Delta G^0_{f\mathrm{LaMnO_3}}$. Hence, as has been pointed out previously [29], $\Delta\mu_i$ for each element is not allowed to become so negative (i.e., more negative than $\Delta G^0_{f\mathrm{LaMnO_3}}$) that the other elements break their upper limit $\Delta\mu_i \leq 0$. Therefore, in the case of $\mathrm{LaMnO_3}$, the lower limits for the chemical potentials μ_i are defined as

$$\Delta\mu_i \geq \frac{1}{x_i}\Delta G^0_{f\mathrm{LaMnO_3}}, \tag{3.35}$$

with x_i equal to the stoichiometric coefficient of i. When Eqs. 3.31 and 3.35 are combined, it follows that

$$\frac{1}{x_i}\Delta G^0_{f\mathrm{LaMnO_3}} \leq \Delta\mu_i \leq 0. \tag{3.36}$$

By considering Equation 3.33 and the limits that have been discussed, a region in the La-Mn-O chemical potential space can now be defined where $\mathrm{LaMnO_3}$ is stable with respect to the reference states. The competing phases, however, impose similar conditions and further limit the range of chemical potentials for which $\mathrm{LaMnO_3}$ is stable. Accordingly, a phase diagram can be constructed to show the stability region for $\mathrm{LaMnO_3}$ by considering the equivalent equations for each of the competing oxides (mathematical details for obtaining these are provided in appendix B.3):

$$\Delta\mu_{Mn} + \frac{1}{2}\Delta\mu_{O_2} \geq \Delta G^0_{fMnO} \tag{3.37}$$

$$\Delta\mu_{Mn} + \Delta\mu_{O_2} \geq \Delta G^0_{fMnO_2} \tag{3.38}$$

$$2\Delta\mu_{Mn} + \frac{3}{2}\Delta\mu_{O_2} \geq \Delta G^0_{fMn_2O_3} \tag{3.39}$$

$$3\Delta\mu_{Mn} + 2\Delta\mu_{O_2} \geq \Delta G^0_{fMn_3O_4} \tag{3.40}$$

$$2\Delta\mu_{La} + \frac{3}{2}\Delta\mu_{O_2} \geq \Delta G^0_{fLa_2O_3} \tag{3.41}$$

For the case of La_2O_3 it is necessary to substitute the value of $\Delta\mu_{La}$ from Eq. 3.33 into Eq. 3.41 before it can be plotted in the same plane, giving the inequality (Appendix B.4):

$$2\Delta G^0_{fLaMnO_3} - \Delta G^0_{fLa_2O_3} \geq 2\Delta\mu_{Mn} + \frac{3}{2}\Delta\mu_{O_2} \tag{3.42}$$

The line of this inequality represents the intersection between the La_2O_3 and $LaMnO_3$ planes and has a region of stability on the phase diagram which is in the opposite direction of those for $LaMnO_3$ and the manganese oxides, i.e. its chemical potentials are relevant when more negative than the energies of formation. When this diagram is viewed in the three-dimensions (Fig. 3.3) with the inclusion of the $\Delta\mu_{La}$ chemical potential axis, the inequalities that were previously described as lines can be shown as planes which form lines at their intersections. Therefore it is important to note that inequalities are only referred to as lines with reference to the two-dimensional diagram.

3.3 Ground States

The optimized lattice parameters of the most stable (crystallographic/magnetic) phases for $LaMnO_3$ and the competing oxides are given in Table 3.2. For the competing oxides some of the other commonly observed crystallograpic phases and magnetic configurations have been investigated and the results are reported in Table 3.3. The ΔE (meV per formula unit) is the increase in energy from the most stable phase and magnetic configuration of the corresponding compound given in Table 3.2.

The low temperature phase of $LaMnO_3$, which is orthorhombic and A-type antiferromagnetic (AAF) has been simulated. Since it is well established that this is the correct $LaMnO_3$ ground state, both by experiments [25,162] and simulations [28,63,72], it was not necessary for the purposes of this study to explore the other phases or magnetic configurations. The calculated lattice parameters **b** and **c** are in good agreement with the experimental values; the percentage error is less than 1.5%. The **a** parameter, however, is overestimated by almost 5% with respect to the low temperature (9K) structure cited. It is noted that there is no experimental certainty for this parameter; values between 5.472-5.748 Å are reported in literature [161]. Previous structural optimisations with different levels of theory also indicate a range of **a** values, which are shifted towards the upper limit; **a** = 5.740 **b** = 7.754 **c** = 5.620 for unrestricted Hartree-Fock [62], **a** = 5.753 **b** = 7.721 **c** = 5.559 for GGA [169]) and **a** = 5.623 **b** =

Table 3.2: Experimental and optimized lattice parameters (**a**, **b** and **c** in Å) of the most stable (crystallographic/magnetic) phases at low temperature for $LaMnO_3$ and the competing oxides. The magnetic solution is indicated in the second column as AFM, FM and NM for the antiferromagnetic, ferromagnetic and non-magnetic case; the type of AFM is labelled by (A) and (G), see Ref. [25]. The arrows proceeding the type of magnetic phase indicate the spin direction of the sequence of Mn atoms in the cell according to Fig. 3.1. The temperature at which the experimental geometry was obtained is given in the column labelled T(K) according to Ref. [161]; a specified range indicates where the compound is stable. The percentage error (%) of the calculated lattice parameters relative to the experimental parameters cited for the compound, are also included in italics.

Compound			Space Group		**a**	**b**	**c**	T(K)	Ref.
$LaMnO_3$		Exp.	Pnma	(62)	5.730	7.672	5.536	9	[162]
	AFM (A)	Opt.			6.010	7.735	5.614		
					4.89	*0.82*	*1.41*		
La_2O_3		Exp.	Ia3	(206)	11.360	-	-	≤770	[163]
	NM	Opt.			11.583	-	-		
					1.96	-	-		
MnO_2		Exp	Pnma	(62)	9.273	2.864	4.522	298	[93]
	AFM ↑↓↑↓	Opt.			9.269	2.882	4.624		
					-0.04	*0.62*	*2.26*		
Mn_2O_3		Exp.	Pbca	(61)	9.416	9.423	9.405	≤302	[90]
	FM	Opt.			9.479	9.538	9.566		
					0.67	*1.22*	*1.71*		
Mn_3O_4		Exp.	I41/amd	(141)	5.757	-	9.424	10	[164]
	FiM ↑↑↓↓↑↑	Opt.			5.814	-	9.558		
					0.99	-	*1.42*		
MnO		Exp.	Fm3m	(225)	4.444	-	-	293	[165]
	AFM (G)	Opt.			4.458	-	-		
					0.32	-	-		

7.814 **c** = 5.528 for GGA+U.

Some insight into the overestimation of the **a** parameter can be gained by analysis of the orientation of the J-T disorted octahedra and comparison with experimental measurements. The most significant observation from the predicted structure is that the elongated Mn-O bonds have the largest component along the **a** direction, indicating that the **a** parameter size is directly correlated to the degree of J-T distortion. This view is supported by recent measurements that shows that **a** parameter lengthening is directly correlated to the extent of J-T distortion of the octahedra, which is regulated by $LaMnO_3$ stoichiometry and doping [170, 171]. Discrepency in the measured **a** parameters, therefore, indicates that literature samples may be non-uniform (phase separated) or non-stoichiometric, and therefore manifest a reduced **a** parameter in averaged measurements [161].

The only competing binary oxide containing La is La_2O_3, which occurs in a body-centered cubic ($Ia3$) structure for the most stable phase (see Table 3.2) and in the trigonal ($P\bar{3}m1$) structure at high temperature (see Table 3.3) [161, 163, 172]; both are non-magnetic. The optimised lattice parameter for the cubic ground state shows

Table 3.3: Experimental and optimised lattice parameters of some of the other commonly observed structures. Annotation is the same as table 3.2, with the addition of **ΔE (meV per formula unit)**, which is the increase in energy from the most stable geometry and magnetic configuration of the corresponding compound given in Table 3.2. * indicates temperature at which the sample was synthesised

Compound			Space Group		**a**	**b**	**c**	ΔE	T(K)	Ref.
La_2O_3		Exp.	P$\bar{3}$m1	(164)	3.937	-	6.129		≥770	[163]
	NM	Opt.			3.999	-	6.331	**136**		
MnO_2		Exp	Pnma	(62)	9.273	2.864	4.522		298	[93]
	FM	Opt.			9.199	2.885	4.674	**43**		
	AFM ↑↓↓↑	Opt.			9.264	2.880	4.627	**8**		
	AFM ↓↓↑↑	Opt.			9.202	2.886	4.677	**39**		
		Exp	P42/mnm	(136)	4.404	-	2.877			[166]
	FM	Opt.			4.441	-	2.895	**67**		
	AFM	Opt.			4.429	-	2.894	**31**		
Mn_2O_3		Exp.	Ia3	(206)	9.417	-	-		723	[167]
	FM	Opt			9.520	-	-	**249**		
Mn_3O_4		Exp.	I41/amd	(141)	5.757	-	9.424		10	[164]
	FM	Opt.			5.842	-	9.560	**200**		
	FiM ↑↑↓↓↓	Opt.			5.800	-	9.577	**12**		
	FiM ↑↓↑↑↑	Opt.			5.822	-	9.554	**99**		
	FiM ↑↑↑↓↑↓	Opt.			5.809	5.825	9.566	**94**		
	FiM ↑↑↑↓↑↑	Opt.			5.821	5.832	9.558	**100**		
	FiM ↑↓↑↓↑↓	Opt.			5.818	-	9.554	**82**		
		Exp.	Pbcm	(57)	3.026	9.769	9.568		1000*	[168]
	FM	Opt.			3.069	9.977	9.637	**770**		
MnO		Exp.	Fm3m	(225)	4.444	-	-		293	[165]
	FM	Opt.			4.483	-	-	**96**		

good agreement with experiment with only a 1.96% error. Overall, for the manganese oxides in Table 3.2, the agreement between the experimental and calculated lattice parameters is also good; less than 2.3% error [65]. The competing binary Mn oxides are discussed in order of decreasing oxidation state as follows: MnO_2(IV), Mn_2O_3(III), Mn_3O_4(II/III) and MnO(II), corresponding to d^3, d^4, $d^{4/5}$ and d^5 occupancy of the d-band respectively.

The lowest energy for MnO_2 was found for the orthorhombic ($Pnma$) antiferromagnetic (AFM) structure, with the spin configuration as indicated by the arrows in Table 3.2. The differences in energy between various spin configurations both within and in between the orthorhombic and rutile ($P42/mnm$) structures, are of the order of tens of meV per formula unit of MnO_2. This can be linked to the high number of polymorphs observed for this material [94, 114]. This finding is in agreement with previous work, but it has to be noted that the stability order is reverted when paramagnetic energies are obtained by fitting a Heisenberg Hamiltonian [114]. In this case, the rutile structure is reported to have a lower energy (by 22 meV) with respect to the orthorhombic [114].

Mn_2O_3 was simulated in its cubic ($Ia3$) and orthorhombic ($Pbca$) forms. The rel-

a) MnO

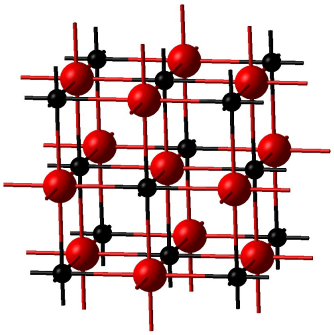

b) Mn_3O_4

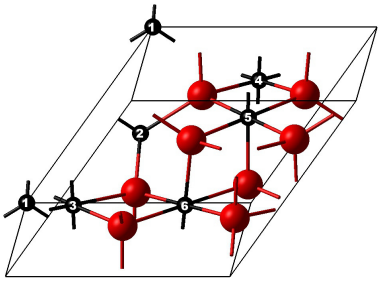

c) Mn_2O_3

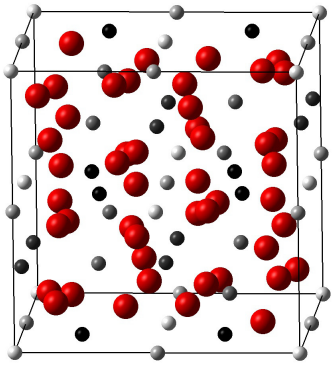

d) MnO_2

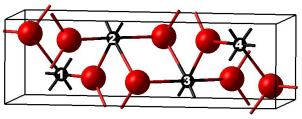

e) La_2O_3

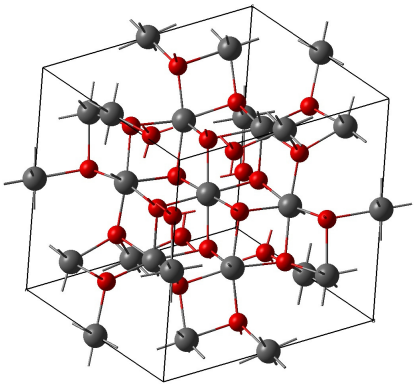

f) $LaMnO_3$

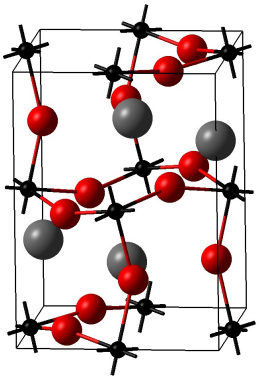

Figure 3.1: The structures of the competing oxides in their ground states. Large grey, Medium red and small black spheres correspond to the La, O and Mn atoms respectively. In the case of Mn_3O_4 and MnO_2, the labelling of the Mn atoms is linked to the assignment of spin in Tables 3.2 and 3.3. Symmetry irreducible Mn atoms are given in gray scale color for Mn_2O_3 for clarity.

ative energies agree with experiment, where the orthorhombic structure is considered stable at low temperature [90, 167]. The structure was only simulated in its ferromagnetic (FM) form as there is no consensus yet on its low temperature magnetic structure from experiment [91, 92].

Although Mn_3O_4 has a non-collinear magnetic structure with long range ordering [85, 86], the simulation has been limited to ferromagnetic and ferrimagnetic (FiM) configurations that can be defined within the primitive cell, consistent with previous work [111]. The spinel ($I41/amd$) FiM ↑↑↓↓↑↑ configuration (see Fig. 3.1 for notation) is the most stable. In Table 3.3 the various FiM/FM configurations of the spinel Mn_3O_4 are shown, differing within a range of 200 meV, while the high-pressure orthorhombic ($Pbcm$) phase is drastically less stable (ΔE =770 meV).

MnO has a faced-centered cubic ($Fm3m$) G-type antiferromagnetic structure at low temperature (T_N=118K); the spins order ferromagnetically on (111) planes with antiferromagnetic coupling between neighbouring planes [173,174]. The optimised structure is characterized by a uniform distortion of the cell angles by 1.52% indicating that at low temperatures the unit cell of MnO becomes rhombohedrally distorted, in agreement with Hartree-Fock calculations [109] and neutron diffraction studies [174]. The distance between antiferromagnetically coupled Mn is shorter (3.135 Å) compared to the ferromagnetically coupled Mn (3.170 Å); therefore, a contraction occurs normal to the ferromagnetic (111) planes corresponding to a magnetostriction effect. This does not occur in the FM phase, which has an energy 96 meV higher and an Mn-Mn distance of 3.170 Å.

3.4 Formation Energies

The calculated Gibbs formation energies for the stable (lowest energy) phases of $LaMnO_3$ and the competing Mn oxides are compared in Table 3.4 with experimental Gibbs formation energies obtained from a thermochemical database [99]. The calculated and experimental $\Delta_f G$ are identical by construction for La_2O_3 (cf. Section 3.2.2), therefore it is omitted from this table.

Table 3.4: Gibbs free energy of formation (eV) for $LaMnO_3$ and the manganese oxides [45, 99].

Compound	**Experimental** $\Delta_f G^0$	**Calculated**$\Delta_f G^0$	**Error**(%)
$LaMnO_3$	-14.03	-13.89	*-1.0*
MnO_2	-4.82	-4.68	*-3.0*
Mn_2O_3	-9.13	-9.21	*0.9*
Mn_3O_4	-13.30	-13.61	*2.4*
MnO	-3.76	-3.76	*<0.1*

The maximum percentage error of $\Delta_f G^0$ relative to the experimental value in Table 3.4 does not exceed $\pm 3\%$; a positive (negative) error means that the Gibbs formation energy is underestimated (overestimated). The mean relative error is 1.6%. The atypically large error for MnO_2 is noteworthy. It can be attributed to the natural occurance of Ruetschi defects in ramsdellite (orthorhombic MnO_2) [114]; this can stabilise the experimental energies with respect to the (defect free) calculated energy, because low energy defects introduce configurational entropy and lower the Gibbs energy.

In general, the calculated formation energies of the manganese oxides are in very good agreement with experiment. This highlights the quality of the hybrid-exchange functional B3LYP, which is able to consistently describe the oxygen molecule and the complete set of manganese oxides, even though they are characterised by different oxidation states of the transition metal. The accuracy of the data in Table 3.4 is a significant improvement on that present in recent reports (which have a mean error in the range of 7-22%) [71, 111]. This larger error can be attributed partially to the functionals used (PW91, PBE, PBE+U, PBE0 and HSE) and partially to the approaches adopted for the approximation of μ^0_{Mn} and $\mu^0_{\mathrm{O}_2}$, which did not adequately account for limited error cancellation in the respective approximations to DFT.

Careful consideration of error cancellation can lead to significantly improved energetics, as has been demonstrated in previous work [175]. On the other hand, approximating μ^0_{Mn} and $\mu^0_{\mathrm{O}_2}$ by using the *ab initio* energy of the metal and the oxygen molecule indiscriminately with respect to the exchange-correlation functional can systematically lead to an error. In this chapter, it is the maximisation of error cancellation when calculating the μ^0_{Mn} and $\mu^0_{\mathrm{O}_2}$, which, in addition to the choice of functional, has allowed for the most accurate calculation of the formation energies of the series of Mn oxides.

3.5 Phase Diagram of the La-Mn-O system

Phase diagrams, constructed from the experimental and calculated Gibbs formation energies, are compared in Fig. 3.2. The calculated bulk $LaMnO_3$ stability region is in good agreement with experiment. It is noted that in Fig. 3.2 the stability region of $LaMnO_3$ is affected by even a small percentage deviation from the experimental $\Delta_f G^0$ of $LaMnO_3$ and Mn_3O_4 (1% and 2.4%, respectively). This suggests that, in previous studies [71, 111] where the greatest accuracy for the series of calculated formation energies had a mean error of 7% (including a deviation of 16% for MnO_2), the resulting phase diagrams are likely to be misrepresenting the actual phase boundaries.

Figure 3.3 shows the phase diagram in 3D space by inclusion of the $\Delta\mu^0_{\mathrm{La}}$ axis. This

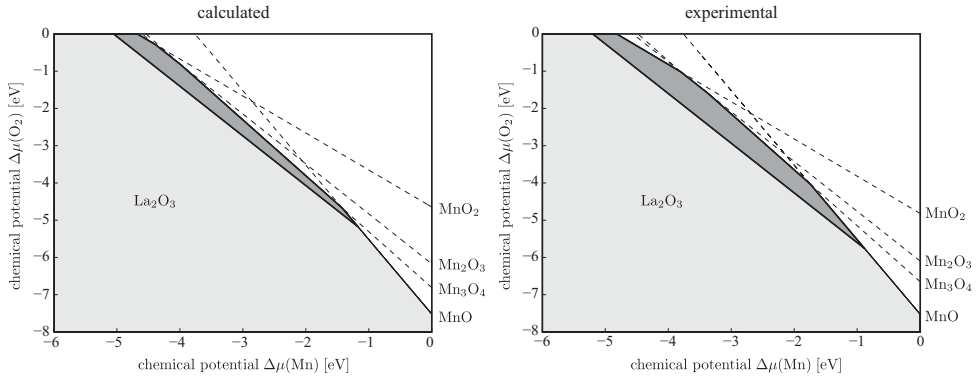

Figure 3.2: Two-dimensional phase diagrams obtained by using the experimental and calculated Gibbs formation energy at standard conditions. The stability region of $LaMnO_3$ is represented by the dark gray area.

allows for a better understanding of the stability of each compound and limiting phase equilibria. The decomposition of $LaMnO_3$ into La_2O_3 and gaseous oxygen sets the lower limit of the chemical potential of manganese. On the other hand, the upper limit for the manganese chemical potential varies strongly according to the environment. In strongly oxidising environments, the stability of $LaMnO_3$ is limited by the manganese oxide that can stabilise the most oxygen (MnO_2), while the reverse is true for a strongly reducing environment (MnO). Under mildly reducing or oxidizing conditions, $LaMnO_3$ forms equilibria with Mn_3O_4 and Mn_2O_3, which contain the intermediate (III) oxidation state of manganese.

This careful documentation of the $LaMnO_3$ bulk stability region sets meaningful limits of the chemical potentials for the investigation of surface terminations, which is a prerequisite for the investigation of catalytic properties in relation to AFC applications.

3.6 Summary

The thermodynamic phase stability of bulk $LaMnO_3$ and the manganese oxides have been investigated using hybrid DFT with periodic boundary conditions. The most stable geometric and magnetic phases of the compounds in the La-Mn-O system were determined and used to calculate the Gibbs formation energies. Quantitative agreement between calculated and experimental formation energies at standard temperature and pressure was achieved (a mean error of 1.6%). This allowed for the investigation of the different phase equilibria that confine the stability region of bulk $LaMnO_3$ in chemical potential space, and therefore the region where any surfaces of $LaMnO_3$ can be stable,

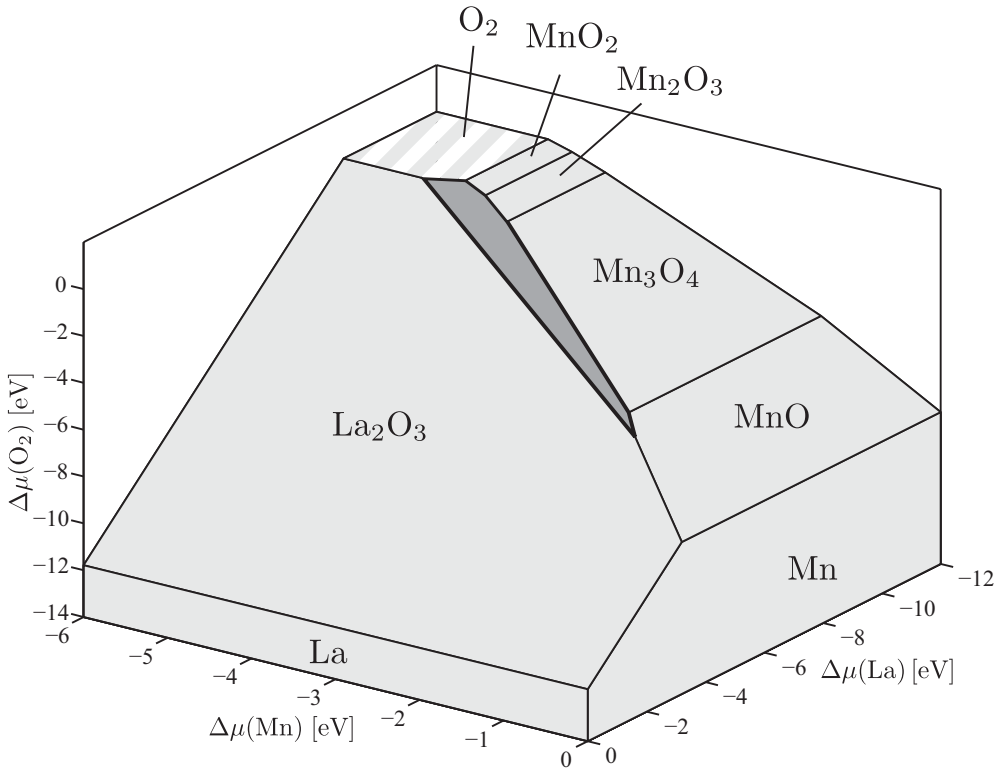

Figure 3.3: Three-dimensional phase diagram constructed from the calculated Gibbs formation energies at standard conditions. The stability region of $LaMnO_3$ is represented by the dark gray area.

for the complete system where metals, oxides, and gases partake.

The methodology developed in this chapter was key to the investigation, as it allowed for the accurate calculation of the oxygen and manganese chemical potentials, and subsequently demonstrated that DFT simulations using the B3LYP functional can accurately predict the thermodynamics for the range of manganese valence states in its oxides. With regards to the study of the $LaMnO_3$ as a catalyst in AFCs, this is crucial, as the surfaces of $LaMnO_3$ are certain to contain multiple oxidation states of manganese. Therefore, in conclusion, our methodology properly described the thermodynamics of bulk $LaMnO_3$ and will be able to address its surfaces.

4

Oxidation State Mapping of Manganese

4.1 Introduction

It is apparent, from the discussion of $LaMnO_3$ literature in Sec. 1.3, that there is a lack of knowledge on the surfaces that exist on actual crystallites of orthorhombic $LaMnO_3$. This is because the characterisation of $LaMnO_3$ surfaces is difficult by experiment, since the majority of synthesis routes lead to polycrystalline powder samples, where the exposed surface facets are not well defined. A macroscopic picture of powdered oxide surfaces can be obtained via techniques such as X-ray photoelectron spectroscopy (XPS) and low-energy ion scattering (LEIS) [176, 177], which can reveal chemical states and atomic compositions. However, on its own, this data does not aid us in determining which specific surfaces are present on $LaMnO_3$ crystallites; this can be achieved by comparing the measured data with a picture of the chemical states and compositions of each surface. It is in building up this picture of the surfaces, that predictive simulations have an important role to play.

The structural composition of various $LaMnO_3$ surfaces are studied in the following chapter. Thus, LEIS measurements of the surface composition from $LaMnO_3$ crystallites and single crystals can be compared to the predicted structures for verification. The chemical states of the studied surfaces, on the other hand, are not investigated. Thus, the aim of this chapter is to identify descriptors for the chemical state of the atoms on the $LaMnO_3$ surfaces through computational means. Correlating experimental measurements of $LaMnO_3$ crystallites to simulations using these descriptors can then validate the structural features at the crystallite surfaces.

In terms of experimental techniques that are sensitive to the valence state of ions, both XPS and electron energy loss spectroscopy (EELS) qualify [178, 179]. In fact, under the right conditions, EELS can even resolve single atomic sites [180]. The high resolution of EELS could, therefore, allow it to be used for the identification of Mn ions that are characteristic of specific $LaMnO_3$ surfaces. The change in valence state of various ions is typically observed by a shift of the ionisation edges in the EEL spectra [179]. For Mn, the shift is significant in the L_2 and L_3 edges and is documented for a range of Mn oxides [181]. In literature, however, these edges are not well characterised for the $LaMnO_3$ surfaces.

In this chapter, therefore, a methodology is developed where the ionisation edges can be predicted for the states of the Mn ion in various Mn oxides. The predicted ionisation edges are compared with measured spectra to determine the accuracy of the simulated EEL spectra. The accuracy of the simulated EEL spectra determines if the methodology is viable for the mapping of Mn oxidation states on the $LaMnO_3$ surface.

4.2 Electron Energy Loss Spectroscopy

When an electron beam is passed through a solid, electrons that are scattered inelastically carry information about its chemical environment and electronic structure [179]. EELS is a technique that extracts this information from the EEL spectrum, which plots the electron scattering intensity against the energy-loss of the transmitted electron. Because this technique involves the transmission of an electron beam through the sample (usually carried out *in situ* during transmission electron microscopy (TEM)) and measuring the energy loss, typically the bulk properties of the sample are obtained. However, if the spatial resolution is small enough it is possible to obtain a signal specific to atoms at a precise location, i.e. for a column of specific atoms at an edge (surface).

Since an exhaustive discussion of EELS can be found in various textbooks [179, 182, 183], in this section, the aspects of EELS relevant to the methodology adopted in this work are mainly discussed; the focus being on the signal change due to different states of the Mn ion, which can be observed in the Mn $L_{2,3}$ edges. These edges refer to peaks in the region of the energy loss signal that correspond to inner shell excitation, where the core electrons are excited into the unoccupied states above the Fermi level. In particular, the L_2 and L_3 edges of Mn occur due to the excitation of electrons from the $2p^{1/2}$ and $2p^{3/2}$ states, respectively, into the empty $3d$ states (see Table 4.1) as permitted by the dipole-selection rule [183].

Table 4.1: Summary of the initial and final states corresponding to the L_2 and L_3 core-shell ionisation edges in Mn.

Edge	Initial State	Final State
L_2	$2p^{1/2}$	s, d
L_3	$2p^{3/2}$	s, d

The region of the EEL spectra extending for 15 eV above ionisation edge onset is referred to as the energy-loss near-edge structure (ELNES). The ELNES can be described as a continuum of electron-scattering phenomena that is sensitive to the valence and local environment (coordination, bond distance) of the atoms [183]. The peaks in the ELNES region are dependent on the energies of the empty states in the conduction band that accept the ejected electrons, meaning that the energy loss of the incident electrons reflects the distribution of the empty states. Therefore, the simplest model of the ELNES mirrors the unfilled density of states (DOS) above the Fermi level [183, 184]. Additionally, for the analysis of specific atomic sites, this region can be interpreted by means of the projected density of states (PDOS) of the atom being probed. Although this interpretation of the ELNES does not consider effects such as multiple scattering and core holes, these differential effects are not significant for the excitation of core electrons (contrary to valence electron excitation), allowing for the edges to be well approximated by single-atom theory [184]. Evidence for the correlation of DOS with ELNES peaks can be found in studies of diamond, graphite, TiO_2 and many other compounds [184–186].

In order to simulate the $L_{2,3}$ edge of Mn in this work the DOS will be projected only on Mn atoms. Additionally, to identify the characteristics of the $L_{2,3}$ edge for Mn atoms with particular valence states or coordination, projections of DOS onto the atomic orbitals centred at the considered Mn sites will be performed. The energy loss of the incident electrons will also be approximated as the difference in energy between the $2p$ and $3d$ orbitals of the specific Mn site. The broadening of the measured ELNES due to the energy resolution of the instrument is accounted for by a convolution of the DOS with a Gaussian function of width proportional to the resolution (0.4 eV in the reference work discussed in the following section) [187]. Lastly, it is important to point out that in the case of the $L_{2,3}$ edge, spin-orbit splitting gives two initial states with different energy ($2p^{1/2}$ and $2p^{3/2}$), resulting in the measured ELNES to be equivalent to two shifted unoccupied DOS distributions. In this work the DFT calculation does not account for spin-orbit splitting. The single DOS of the unoccupied states produced is, therefore, approximated as the L_3 edge.

In order to evaluate the simulated EEL spectra, the main compounds analysed are,

Mn_3O_4, Mn_2O_3 and MnO, since they provide references for Mn in different oxidation states and chemical environments (coordination). Mn_3O_4 is a particularly useful reference compound for the simulated EEL spectra since the ground state structure, as determined in Ch. 3, consists of Mn in two different states; two of the Mn ions in the formula unit are in the +3 oxidation state with an octahedral (Oh) coordination, while the remaining Mn ion is +2 with tetrahedral (Td) coordination. This will allow for evaluation with respect to the changes in coordination/valence of Mn within the same compound, similar to what is expected for the $LaMnO_3$ surface. Furthermore, the L_3 edge of these Mn valence states has been measured for a range of compounds, including Mn_3O_4, thus providing sufficient references for comparison [181, 187].

4.3 Mapping the Oxidation states of Mn in Mn_3O_4

In this section the simulated EEL spectra are presented and evaluated in terms of their ability to identify the oxidation states of Mn in various compounds (i.e. in different chemical environments). Furthermore, comparisons are made with the measured EEL spectra to verify the accuracy of the computational methods and explore the origins of the L_3 edge shapes.

In Fig. 4.1, the simulated EEL spectra for the L_3 edge of Mn in the 2+ and 3+ oxidation state are presented for Mn_3O_4, Mn_2O_3 (3+) and MnO (2+). The calculated L_3 edges for Mn^{3+} in Mn_3O_4 and Mn_2O_3 match reasonably well (upper spectra in Fig. 4.1), although the Mn_2O_3 feature is broader. This could perhaps be associated with the large number of symmetry related Mn^{3+} sites available in Mn_2O_3 (see Fig. 3.1). It is possible that variations occur in the L_3 signal due to the different local environment of each Mn^{3+} site, which combine to give the overall broader L_3 edge observed. On the contrary there are only two Mn^{3+} sites in Mn_3O_4, resulting in the better defined L_3 edge. Overall, other than the effects of local environment (i.e. coordination), which are known to affect the peak shape [179, 181], it can be said that the simulated spectra show good alignment for the shift of the peaks on the Mn^{3+} site, serving as a valid "proof of concept" for identifying this oxidation state of a surface Mn ion in $LaMnO_3$.

The calculated L_3 edges for Mn^{2+} in Mn_3O_4 and MnO also show good agreement (middle spectra in Fig. 4.1), except for the presence of a larger shoulder at higher binding energy (638 eV) in Mn_3O_4. Again, this variation in the shape of the L_3 edge is attributed to the different local environments for Mn^{2+} in Mn_3O_4 and MnO, while the shift of the main peak remains well aligned to the oxidation state.

In order to understand the effects of local environment on the shape of the L_3 edge

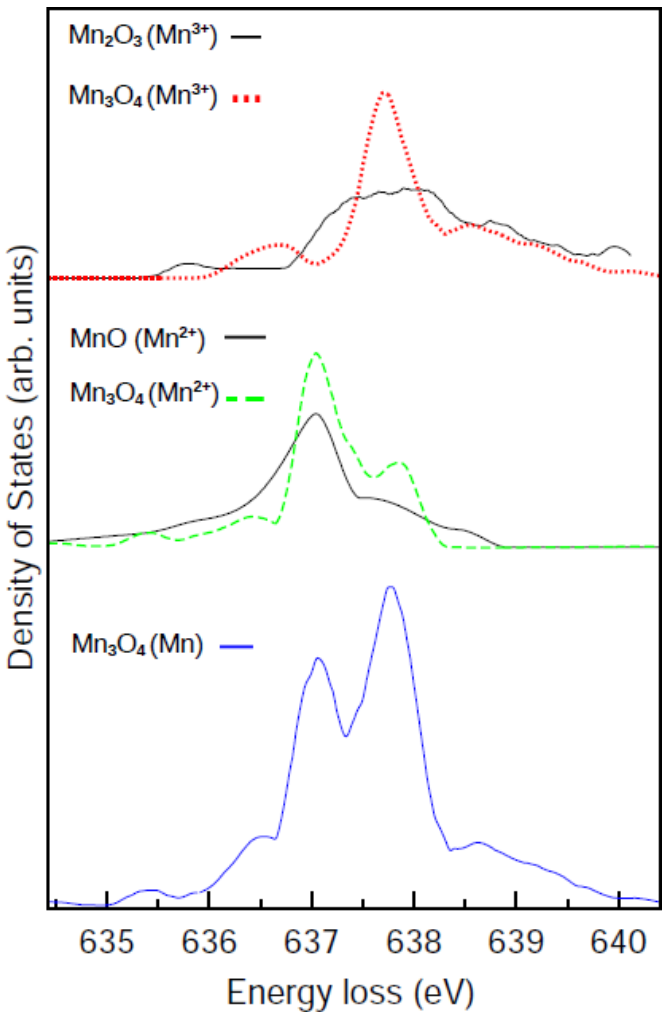

Figure 4.1: Calculated EEL spectra (L_3) for Mn^{2+}/Mn^{3+} in various compounds.

it is useful to compare the simulated spectra against the measured data available in literature for the EEL spectra of Mn_3O_4, presented in Fig. 4.2. In the measured EEL spectra, it is immediately evident that the shape of the Mn^{2+} L_3 edges for MnO and Mn_3O_4 do not match due to the presence of a shoulder in the Mn_3O_4 spectra at higher binding energy (as observed in the corresponding simulated spectra). For the measured EEL spectrum of Mn_3O_4, the Mn^{2+} signal is isolated by using spatially resolved EELS on a crystal of Mn_3O_4 oriented in the (100) direction. This orientation gives columns of Mn atoms separated by their oxidation state (Mn^{2+} and Mn^{3+}), allowing a separate signal for each state to be obtained. The existence of the aforementioned shoulder would, therefore, indicate that the signal for Mn^{2+} in Mn_3O_4 is unique from that in

MnO due to its local environment. However, the authors (Tan *et al.*) of the measured EELS data suggest that this discrepancy occurs solely due to signal intermixing, disregarding contributions from the difference in Mn^{2+} coordination in the compounds (octahedral (Oh)/tetrahedral(Td)).

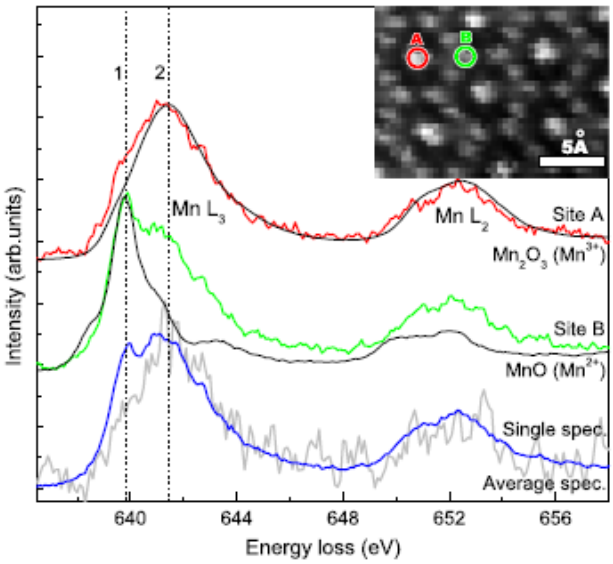

Figure 4.2: EEL spectra ($L_{2,3}$) for Mn^{2+}/Mn^{3+} in Mn_3O_4, Mn_2O_3 and MnO, measured by Tan *et al.* [187]. Red, green and blue line correspond to Mn^{3+}, Mn^{2+} and total Mn spectra from Mn_3O_4, respectively. Inset shows the corresponding atomic sites via HAADF-STEM*.

In order to extract the origin of the shape of these L_3 edges and the proposed invariance with local environment, it is possible to further analyse both the measured and simulated EEL spectra of Mn^{2+}. To begin with, we consider the proposed intermixing effect. The shoulder on the L_3 edge of Mn^{2+} in Mn_3O_4 is rationalised by Tan *et al.* to be due to intermixing, with 22% of the Mn^{3+} signal being present on the Mn^{2+} site [187]. A simple model for delocalisation, $d_E = 0.5\lambda/\theta_E^{\frac{3}{4}}$ [180, 188], suggests a limit of 1.4Å for the experiment by Tan *et al.* [187]. This is equal to the distance between the two sites, thus intermixing is not expected to be pronounced. Additionally, the increase in intensity of the shoulder from the reference Mn^{2+} signal in the measured Mn_3O_4 spectra is far greater than the proposed 22% intermixing (Fig. 4.2 suggests 50% of the Mn^{3+} signal).

An alternative explanation for the Mn_3O_4 L_3 edge is based on the effect of Oh versus Td coordination on the Mn^{2+}-$3d$ states. This can be understood by projecting

* Reprinted with permission from H. Tan, S. Turner, E. Yucelen, J. Verbeeck, and G. Van Tendeloo, *Phys. Rev. Lett.* **107** 107602 2011. Copyright 2011 by the American Physical Society.

the calculated EEL spectra (PDOS) onto the symmetry distinct Mn^{2+}-*3d* states, as presented in Fig. 4.3. In order to provide an additional reference for *Td* coordinated Mn^{2+}, the calculated EEL spectrum of $MnFe_2O_4$ is also presented here.

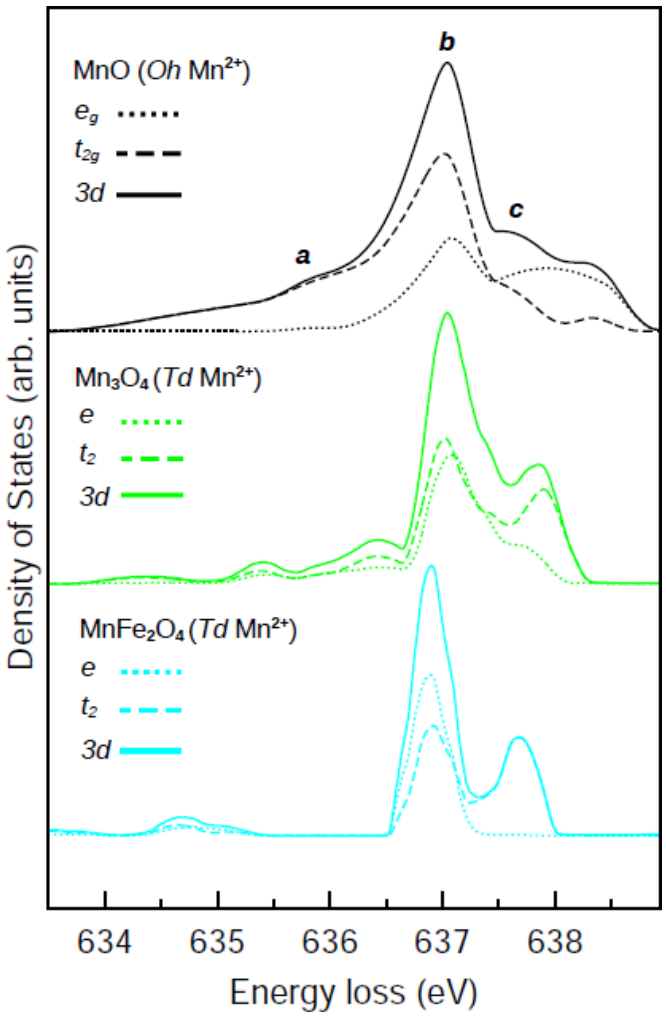

Figure 4.3: Calculated EEL spectra with split 3*d* states (L_3) for Mn^{2+}/Mn^{3+}. Spectra are scaled to have equal peak **b** intensities for comparison.

It is apparent from the calculated L_3 edges of these three compounds that the shift of the main peak **b** is defined only by the oxidation state - it remains the same. On the other hand, moving from *Oh* to *Td* coordination results in a significant reduction in the intensity of the peak labelled **a**. This is also observed in the measured Mn_3O_4 EEL spectra of Fig. 4.1 where the (green) L_3 edge of Mn^{2+} in Mn_3O_4 is observed to lose intensity in the peak **a** region.

The shoulder previously identified at higher binding energy on the L_3 edge of Mn^{2+} in Mn_3O_4 is labelled in Fig. 4.3 as peak **c**. This peak, contrary to what is observed for peak **a**, becomes more intense in Mn_3O_4. It is also shifted to a higher binding energy energy in the *Td* coordination, being more clearly defined. This can be explained in terms of crystal field splitting; the t_2 (*Td*) states being at higher binding energy than the t_{2g} (*Oh*) states - as observed in the simulated EEL spectrum.

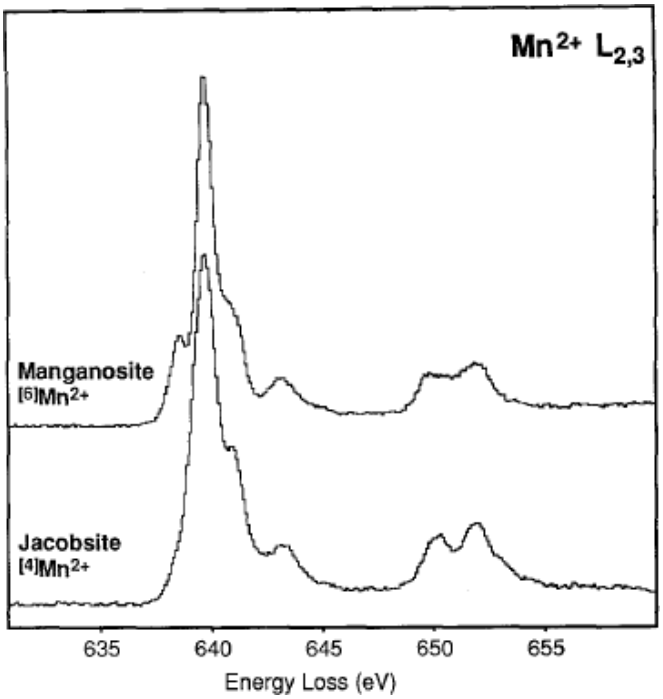

Figure 4.4: EEL spectra showing the Mn^{2+} $L_{2,3}$ edges of *Oh* coordinated Mn in Manganosite (MnO) and *Td* coordinated Mn in Jacobsite ($MnFe_2O_4$), measured by Garvie *et al.* [181].†

Similar changes to peaks **a** and **c** are observed when moving from *Oh* coordination in the measured L_3 edges of MnO to *Td* coordination in $MnFe_2O_4$, as shown in Fig. 4.4. It is notable that the increase in intensity of peak **c** in Mn_3O_4 (Fig. 4.1) is much larger than that measured for the corresponding peak of $MnFe_2O_4$ (Fig. 4.4), even though both peaks are from *Td* coordinated Mn^{2+}. This is in fact predicted in the simulated EEL spectra where the increase of peak **c** intensity in Mn_3O_4 is also greater by 20%. It is apparent that this is due to the combined contribution of e and t_2 states to peak **c** in Mn_3O_4, whereas in $MnFe_2O_4$ only the t_2 states contribute. This suggests that small

†Reprinted from Ultramicroscopy , **21**, L. A. J. Garvie and A. J. Craven, Electron beam induced reduction of Mn in manganese oxides as revealed by parallel EELS, 191–206, Copyright 1994, with permission from Elsevier.

changes in local environments (i.e. the presence of Fe) have a measurable effect on the L_3 edge.

4.4 Summary

The calculation of the L_3 edge of the EELS of Mn using the method adopted in this work has shown that the oxidation state of Mn can be identified in various compounds. It is characterised by a distinct shift in binding energy for the main peak of the L_3 edge. In this work shifts have been identified for the Mn^{3+} and Mn^{2+} oxidation states. Additionally, it has been shown that the calculated and measured L_3 edge of Mn is highly sensitive to the local environment of the Mn ion, particularly for Mn^{2+}. By calculating the L_3 edges of the split $3d$ states (i.e. t_{2g} and e_g) it is further possible to identify peak features that convey the type of coordination around the Mn ion.

Correlating these simulations to the measured EELS spectra of Mn ions should, therefore, not only allow for mapping of the oxidation states of surface Mn ions, but also reveal the type of coordination around the Mn ion. The coordination around the surface Mn ions can allow us identify whether a site is likely to be reactive, but is also useful as it enables structural verification of any predicted surface terminations.

5

The Stability of Orthorhombic $LaMnO_3$ Surfaces

5.1 Introduction

In the literature relating to experimental work on $LaMnO_3$ (Sec. 1.3.1), it was noted that there is very little knowledge of the structure and properties of the surfaces of $LaMnO_3$. In particular, the range of surfaces that exist on the crystallites that make up the catalyst powders used in AFCs have not been identified. This provides an opportunity, therefore, for simulations to predict the thermodynamically favoured surfaces that are possible based on their stability.

Towards this goal, theoretical works have studied the low index (001), (110) and (111) surfaces, exploring various terminations and reporting on their structure and stability [28,67,71,189]. Investigation of the structural differences between the cubic and orthorhombic phase surfaces have also been carried out [28, 71]. These works, however, do not consider the additional variations in surface structure of the orthorhombic phase due to its symmetry. For instance, in the cubic phase the (100), (010) and (001) surfaces are equivalent, but in orthorhombic phase they are considerably different.

The lack of focus on the orthorhombic surfaces may be partly due to fact that the standard DFT methods neglect the important on-site correlations, which allow an accurate description of J-T distortion and orbital ordering in the orthorhombic phase [34, 119]. The effects of these local distortions and the long range ordering in the near surface region are an important consideration when studying the atomic structure of the $LaMnO_3$ surfaces [34, 63]. Only a single theoretical study so far has reported the effects of J-T distortion on the surface of orthorhombic $LaMnO_3$ [78]. This work, which

reports the % displacement of the surface atoms upon relaxation from the optimised bulk geometry, unfortunately considers only the (001) surface.

Since the full extent of the variations in surface structure due to the distortions of the orthorhombic phase is not known, nor has any attempt to comprehensively study the range of surfaces and terminations possible on orthorhombic $LaMnO_3$ been made so far, this chapter will focus on working from the ground up and establishing the surfaces that can exist. Only once we have determined this can we systematically build up a picture of the catalyst particle surfaces based on their thermodynamic stability.

The first step to achieve this is to identify and construct the surface slabs according to the low index surfaces possible – (hkl), with $|h|$, $|k|$ and $|l| \leq 1$ – as detailed in Sec. 5.1.1 below. Subsequently, the structure of the modelled surfaces before and after relaxation is discussed in Sec. 5.2. After this basic analysis, the effects of J-T distortion, bond cleavage, the compensation of ion undercoordination and relaxation on the surface formation energies are explained in Sec. 5.3 and Sec. 5.4, the latter section using electron density difference maps to highlight the polarisation of the undercoordinated ions. Finally a Wulff construction is used to analyse the % coverage of the surfaces in an equilibrium crystal morphology in Sec. 5.5, before Sec. 5.6 summarises the main findings of the chapter.

5.1.1 Surface Simulation

The surfaces of orthorhombic $LaMnO_3$ have been studied by adopting a slab model, which is periodic in two directions and consists of a sequence of atomic layers – parallel to the planes defined by the Miller indices (hkl) – cut from the optimized bulk geometry that has been reported previously [190]. In order to assess the stability of the various surfaces, the surface formation energy per unit area, E_s, is:

$$E_s = \frac{1}{2A}\left(E_{slab} - nE_{bulk}\right) \tag{5.1}$$

where E_{slab} is the total energy of the slab per unit cell of area A containing n formula units, and E_{bulk} is the total energy per formula unit in the bulk. Equation 5.1 does not take into account the influence of the chemical environment, and is only applicable to slabs with bulk stoichiometry.

All of the low index surfaces of the orthorhombic ($Pnma$) $LaMnO_3$ phase, as determined by cleaving the relaxed bulk structure [190], are listed in Table 5.1. These surfaces can be analysed and classified according to the charge q (assuming formal charges for all ions) of each atomic layer and the dipole moment perpendicular to

Table 5.1: The atomic layer sequences of the low index surfaces of orthorhombic (*Pnma*) AAF $LaMnO_3$. In the column "Sequence", the stacking sequence of the atomic layers in the non-periodic direction (z) is indicated for the repeat unit of the slab; as regards notation, 2O-2La 2O-2O-2Mn, for instance, corresponds to a sequence of four layers as separated by hyphens. n-layers and n-atoms give the number of layers and of atoms in the repeat unit.

Miller Indices	Sequence	n-layers	n-atoms	Area(Å^2)	**a**(Å)	**b**(Å)
(1 0 0)	O-La-2O-2O-La-O-2Mn	7	10	43.425	5.614	7.735
(0 1 0)	2O-2La 2O-2O-2Mn	4	10	33.740	5.614	6.010
(0 0 1)	La-O-2O-2O-O-La-2Mn	7	10	46.483	6.010	7.735
(1 1 0)	O-La-O-O-O-O-La-O-2Mn	9	10	54.992	5.614	9.795
(1 0 1)	2O-La-La-O-2O-O-4Mn-O-2O-O-La-La-2O	13	20	63.611	7.735	8.224
(0 1 1)	2O-2O-2La-2O-2Mn-2O-2La-2O-2O-2Mn	10	20	57.437	6.010	9.558
(1 1 1)	O-O-O-La-La-O-O-O-2Mn	9	10	72.005	8.224	9.558

the surface μ_z of a stoichiometric repeat unit of atomic layers [191]. Upon examining the atomic layers of the planes in Table 5.1, it is evident that orthorhombic (*Pnma*) $LaMnO_3$ cannot form any low index Tasker Type 1 surfaces, since there are no neutral atomic layers ($q \neq 0$) [191]. However, it is possible to take the charged atomic layers and construct symmetric slabs so that there is no dipole moment perpendicular to the surface ($\mu_z = 0$), corresponding to Tasker Type 2 surfaces. This is achieved by choosing the appropriate terminating atomic layer, restricting us to the options listed in Table 5.2 for unreconstructed surfaces.

Table 5.2: The sequence of atomic layers of the low index surfaces of the orthorhombic (*Pnma*) $LaMnO_3$ phase simulated as Tasker Type 2 slabs in this work. The notation is as in Table 5.1.

Miller Indices	Sequence	n-layers	n-atoms	Thickness(Å)
(1 0 0)	2O-La-O-2Mn-O-La-2O	7	10	2.893
(0 0 1)	2O-O-La-2Mn-La-O-2O	7	10	2.523
(1 1 0)	O-O-La-O-2Mn-O-La-O-O	9	10	2.197
(1 0 1)	2O-La-La-O-2O-O-4Mn-O-2O-O-La-La-2O	13	20	3.753

The (010), (011) and (111) surfaces are Tasker Type 3 and cannot form Tasker Type 2 by choosing a suitable terminating layer. This type of surface is characterised by a dipole moment ($\mu_z \neq 0$) and results in a surface energy that is infinite, based on purely electrostatic considerations [191]. Reconstructions, chemical adsorptions and charge transfer can quench the macroscopic dipole and stabilise a Tasker Type 3 surface. The focus of this study, however, is on the surface energetics and relaxation of the orthorhombic phase of $LaMnO_3$, the features of which can be more easily isolated on the less complex unreconstructed stoichiometric surfaces listed in Table 5.2.

5.2 Surface Structure and Energetics

The Type 2 surfaces listed in Table 5.2 and the surface formation energies E_s are analysed in terms of bond cleavage, local geometry, relaxation and octahedral distortions. The different contributions to E_s can be disentangled by comparing the unrelaxed and relaxed slabs and defining the relaxation energy $E^{\text{Relaxation}}$ as the energy difference between them, which is normalised with respect to the surface area. The energy of the unrelaxed slab is used to rationalise the cost of cleavage by focusing on cleaved bonds and the truncation of octahedra at the surface terminations (note that by "bond" we do not imply a covalent bond but an Mn-O contact). For the relaxed slab we can focus on the specific local relaxations that increase $E^{\text{Relaxation}}$ and thus contribute to the stability of the surface.

In Fig. 5.1 the unrelaxed and relaxed E_s are presented as a function of slab thickness. The E_s value, converged with respect to the slab thickness for each surface, is also given in Table 5.3, where the surfaces are listed in the order of E_s. Both the unrelaxed and relaxed surfaces show the same order of stability, although the (001) and (101) surfaces become very similar in energy upon relaxation, due to the large relaxation of the (001) surface. The terminating oxygen layer of the (001) surface is also characterised by the greatest inward relaxation Δz of all the surfaces studied.

Table 5.3: The surface formation energies E_s of the stoichiometric Type 2 surfaces of orthorhombic ($Pnma$) AAF $LaMnO_3$. Mn^{coord} is the average coordination of the Mn in the surface layer. The inward/outward relaxation of the terminating oxygen is reported with a negative/positive Δz. $E_s^{\text{Unrelaxed}}$ and E_s^{Relaxed} are the surface formation energies for the unrelaxed and relaxed surfaces, respectively; $E^{\text{Relaxation}}$ is the difference in energy between them, i.e. the surface area normalised energy of relaxation.

Miller Indices	Mn^{coord}	Δz(Å)	$E^{\text{Relaxation}}$(J/m^2)	$E_s^{\text{Unrelaxed}}$(J/m^2)	E_s^{Relaxed}(J/m^2)
(1 1 0)	4.5	0.028	*0.69*	2.67	1.98
(0 0 1)	5	−0.376	*1.13*	2.52	1.39
(1 0 1)	5.5	−0.038	*0.89*	2.25	1.36
(1 0 0)	5	−0.200	*0.49*	1.47	0.98

The average coordination of Mn at the termination of each surface is also included in Table 5.3. Surface cleavage reduces the Mn coordination from the bulk value of 6. It has been argued that transition metal coordination to oxygen is the dominant factor in determining E_s and that E_s scales linearly with the loss of coordination [29, 192]. However, for the surfaces we have studied, it is clear that the scaling of E_s is not linear with the Mn coordination, and that the (100) and (001) surfaces have a large difference in formation energy despite having the same Mn coordination. This behaviour is analysed further in Secs. 5.3 and 5.4.

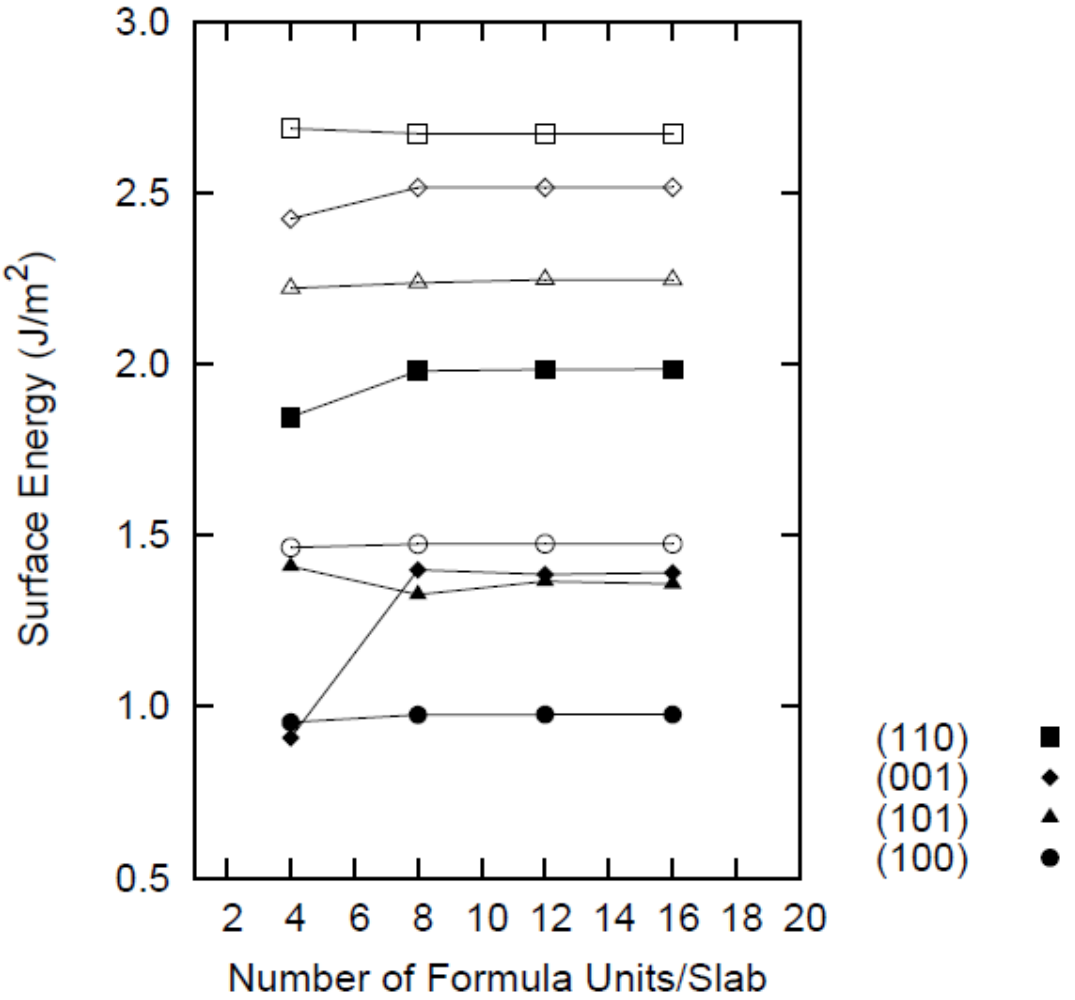

Figure 5.1: The unrelaxed and relaxed surface formation energies E_s with increasing slab thickness, indicated as a function of the number of formula units of $LaMnO_3$ per slab. The unrelaxed and relaxed energies are indicated by the empty and filled points, respectively.

The unrelaxed and relaxed structure of each surface are shown in Figs. 5.2 - 5.5 and discussed in detail in the following sections. The discussion is based on the comparison with the bulk geometry, which can be considered as a packing of corner-sharing MnO_6 octahedra with interstitial La ions. The octahedra are distorted due to the J-T effect, which breaks the degeneracy of the e_g states of Mn^{3+}. Specifically, in each octahedron the Mn-O bond is elongated along a local apical axis (2.31Å) and contracted in the equatorial planes (1.99Å and 1.92Å) [190]. The interaction of these local distortions produces the orbital ordering observed in the bulk structure, which is correctly reproduced in our calculations [34, 190].

The relaxed octahedra at each surface are displayed in Figs. 5.2 - 5.5. On careful examination, it is evident that with respect to the bulk geometry there are significant surface relaxations, which further distort the octahedra via additional rotation and tilt, and further shortening and lengthening of the Mn-O bonds. These effects also propagate through the sub-surface layers by means of the corner-sharing octahedra: geometrical changes which affect O ions linking octahedra lead to distortions that spread from the surfaces into the substrate.

Before we proceed to analyse each surface in more detail (from the highest to lowest E_s), it is important to note that a comparison with previous literature is not straightforward, since the Miller indices referring to a particular surface depend on the space group setting. For orthorhombic $LaMnO_3$, the standard space group setting is *Pnma* (No. 62), but in some of the previous works the *Pbnm* setting has been adopted [67,71]; in this case the set of lattice vectors **abc** of the *Pnma* setting are transformed into **cab**, i.e. the (110) surface of the *Pnma* setting adopted here corresponds to (011) of the *Pbnm* setting [79, 80].

5.2.1 The (110) surface

The (110) surface layer is characterized by 4- and 5-coordinated Mn ions and an La ion, as can be seen from Fig. 5.2. When this surface is relaxed, the truncated octahedron centred at the 4-coordinated Mn is heavily distorted relative to the bulk, while the octahedron centred at the 5-coordinated Mn does not change significantly. There is also a slight outward movement of the La ions. In Figs. 5.2 -5.5 the octahedron in the relaxed slab are only depicted as complete if the Mn-O bond distances are equal or less than the largest bulk Mn-O distance (2.31Å for the apical bond). The incomplete octahedra in the sub-surface layers of the relaxed slab, therefore, indicate cases where the Mn-O distances have significantly increased. The elongated Mn-O bonds are 2.40 and 2.51Å for the incomplete octahedra in the sub-surface layer nearest to the termination. The subsequent octahedra have elongated bonds that are 2.32 and 2.37Å and only return to the bulk value of 2.31Å 32 atomic layers (8.19Å) below the surface. The relaxation of the terminating oxygen layer documented in Table 5.3 indicates an unusual expansion of the (110) surface. If we consider the atomic coordinates of the terminating atoms, it is evident that this surface exhibits a weak rumpling, where the outermost oxygen ion moves inward (by -0.02Å) and the subsequent oxygen ion moves outward (by 0.07Å) becoming the terminating ion. Overall the relaxation reduces the formation energy by 0.69 J/m^2.

The (110) surface of the orthorhombic phase has been previously studied by using an empirical electrostatic shell-model potential [193]. In this study, several terminating layers were studied and it was concluded that the Mn termination was the most stable. However, it is also reported that upon relaxation the La ions are raised to the surface layer and thus the relaxed structure, which is otherwise dominated by Mn and O ions, will also contain La ions. This description of the relaxed surface is in qualitative agreement with our findings.

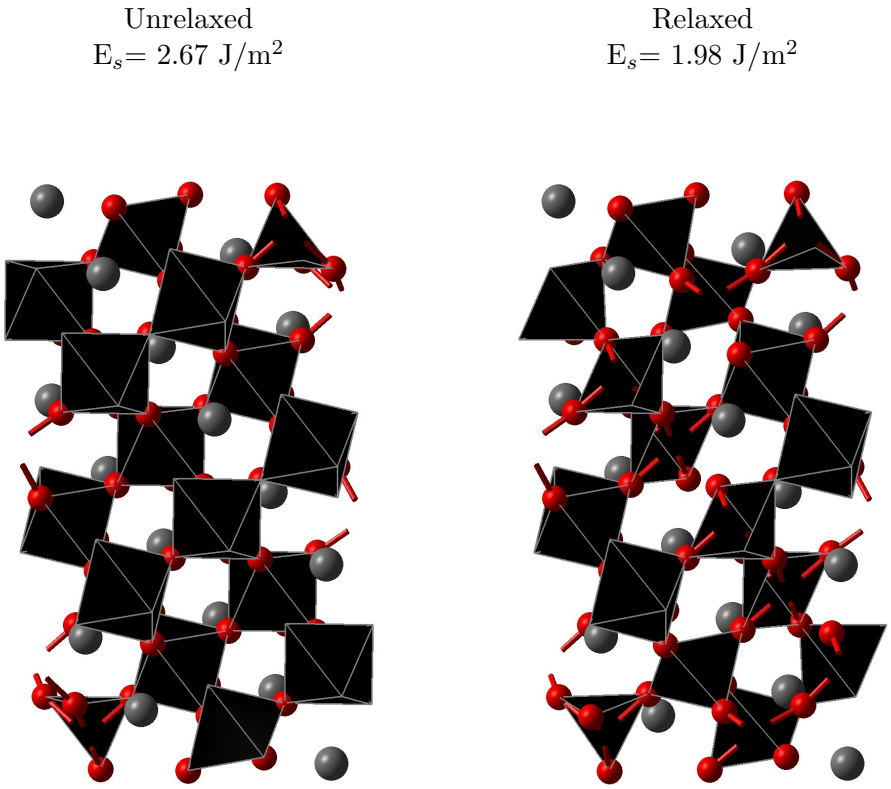

Figure 5.2: The unrelaxed and relaxed slabs of the (110) surface are displayed and the corresponding formation energy reported. Large and small spheres correspond to the La and O ions, respectively. The Mn-O_n unit is represented by a black polyhedron. Incomplete octahedra at the unrelaxed slab terminations indicate cleavage of Mn-O bonds. After relaxation, incomplete octahedra may also indicate a strong distortion by means of Mn-O bond elongation significantly beyond the largest bulk bond distance (the apical bond - 2.31Å).

5.2.2 The (001) surface

The (001) surface layer is terminated by O ions, which belong to truncated octahedra centered at 5-coordinated Mn ions. From Fig. 5.3, it can be seen that the truncated octahedra are tilted relative to the surface normal, and that the interstitial La ions are also exposed. Upon relaxation, the cleaved octahedra at the surface tilt and adopt a different orientation to the bulk. In order to allow this, the Mn-O bonds of the corner sharing octahedra in the sub-surface layers distort relative to the bulk. This effect is visible in the third layer of Mn octahedra for the elongated apical Mn-O bond, which undergoes an increase from 2.31Å to 2.33Å, as indicated by the truncated octahedra in the relaxed slab of Fig. 5.3. These relaxation effects result in the largest inward displacement of the terminating oxygen layer (0.376Å) among all of the surfaces studied (see Table 5.3), as well as the largest $E^{relaxation}$. Interestingly, the relaxation mostly affects the coordination and orientation of the Mn octahedra, while the La ions do not move significantly nor have any noticeable effect on their neighbouring O ions.

To the best of our knowledge, there are no previously published studies of the (001) surface of orthorhombic (*Pnma*) $LaMnO_3$.

5.2.3 The (101) surface

The (101) surface layer has fewer incomplete octahedra per unit cell than either the (110) or (001) surfaces, and this is reflected in its lower $E_s^{\text{Unrelaxed}}$, since fewer bonds have been cleaved. As evident in Fig. 5.4, only half of the terminating octahedra are incomplete, each exposing a 5-coordinated Mn. A unique feature of this surface is that the incomplete surface octahedron exposes the 5-coordinated Mn in a trough between two La ions. The remaining features of the surface are otherwise similar to the other surfaces considered, being terminated by O and exposing La ions.

Upon relaxation of the (101) surface, the only significant change occurs on the terminal layer, where an apical Mn-O bond belonging to the terminating 6-coordinated octahedron is lengthened to 2.42Å (as indicated by the newly truncated octahedron in the relaxed slab of Fig. 5.4). Since this relaxation occurs perpendicular to the surface normal, it is expected that the relaxation (in z) of the terminating oxygen layer would not be large (–0.038Å, as reported in Table 5.3). The relaxation energy is, however, relatively high at 0.89 J/m^2, implying that the relaxation of the terminating oxygen layer is not necessarily an indicator of the relaxation energy of a surface.

The (101) surface of orthorhombic (*Pnma*) $LaMnO_3$ is equivalent to the (110) surface in the *Pbnm* setting. Using this alternative setting, previous studies have been

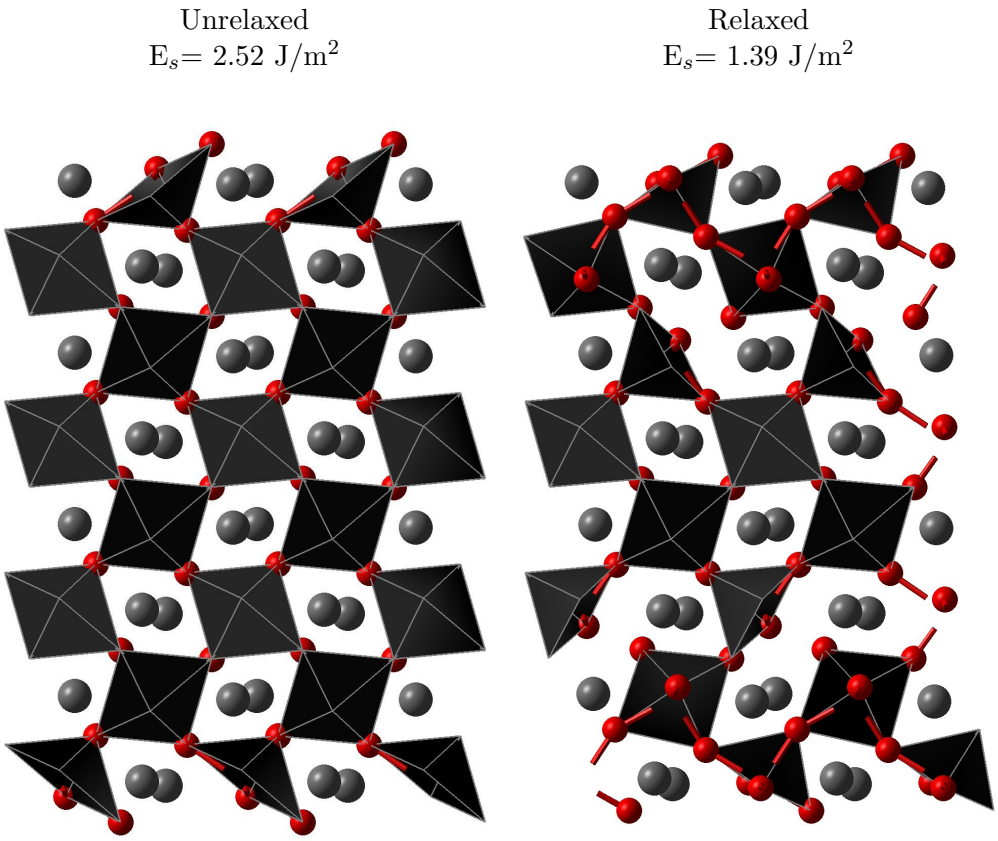

Figure 5.3: The unrelaxed and relaxed slabs of the (001) surface. The unit cell of this surface has been repeated laterally for a clearer depiction of the octahedra. It is terminated by two Mn ions, one of which is symmetric to and hidden from view by the visible one. See Fig 5.2 for details.

published using a variety of approximations (unrestricted Hartree-Fock (UHF) linear combination of atomic orbitals (LCAO) [67], hybrid B3PW LCAO, generalised gradient approximation-plane wave (GGA-PW) [28], and GGA-PW91 [71]). Comparison of the data computed here is not possible as there is an apparent discrepancy in the description of the surface: the (110) atomic layer sequences in the previous studies do not correspond to the orthorhombic phase of $LaMnO_3$. The *Pbnm* (110) surface is reported with an atomic layer sequence of LaMnO-2O-LaMnO-2O, whereas the correct sequence (for *Pnma* (101)) is 2O-La-La-O-2O-O-4Mn-O-2O-O-La-La-2O (as reported in Table 5.2). The sequence in the previous studies appears to instead belong to the (110) surface of the cubic phase.

Unrelaxed
E_s= 2.25 J/m^2

Relaxed
E_s= 1.36 J/m^2

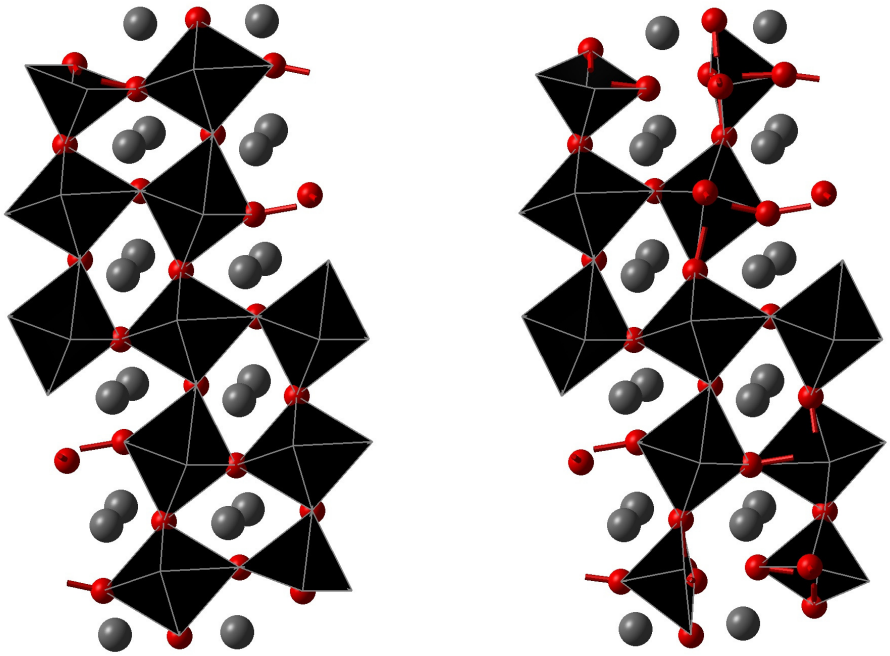

Figure 5.4: The unrelaxed and relaxed slabs of the (101) surface. This surface is terminated by four Mn ions, two of which are symmetric to and obstructed from view by the visible two. See Fig. 5.2 for details.

5.2.4 The (100) surface

The (100) surface is similar to the (001) surface (compare Fig. 5.3 and Fig. 5.5); the terminating layers of both contain 5-coordinated Mn, and the corresponding truncated octahedra share a similar orientation relative to the surface normal. Nevertheless, $E_s^{\text{Unrelaxed}}$ of the (100) surface is much lower than that calculated for the (001) surface, and also significantly lower than the (101) surface, which actually has less Mn under-coordination. This result disagrees with the previously proposed model, which rationalises that the surface formation energies of oxides are dominated by the degree of metal coordination loss [29, 167]. The energetics of the $LaMnO_3$ surfaces are governed by more complex phenomena than simple bond cleavage, as discussed in detail in the following section.

Upon relaxation, the terminating Mn octahedra do not tilt to the same degree observed on the (001) surface, but a set of apical Mn-O bonds in sub-surface layer are lengthened. This leads to an energy of relaxation and inward displacement roughly half of that for the (001) surface (see Table 5.3). As with the (001) surface, to the best of the authors knowledge there are no previous studies of the (100) surface of orthorhombic *Pnma* $LaMnO_3$.

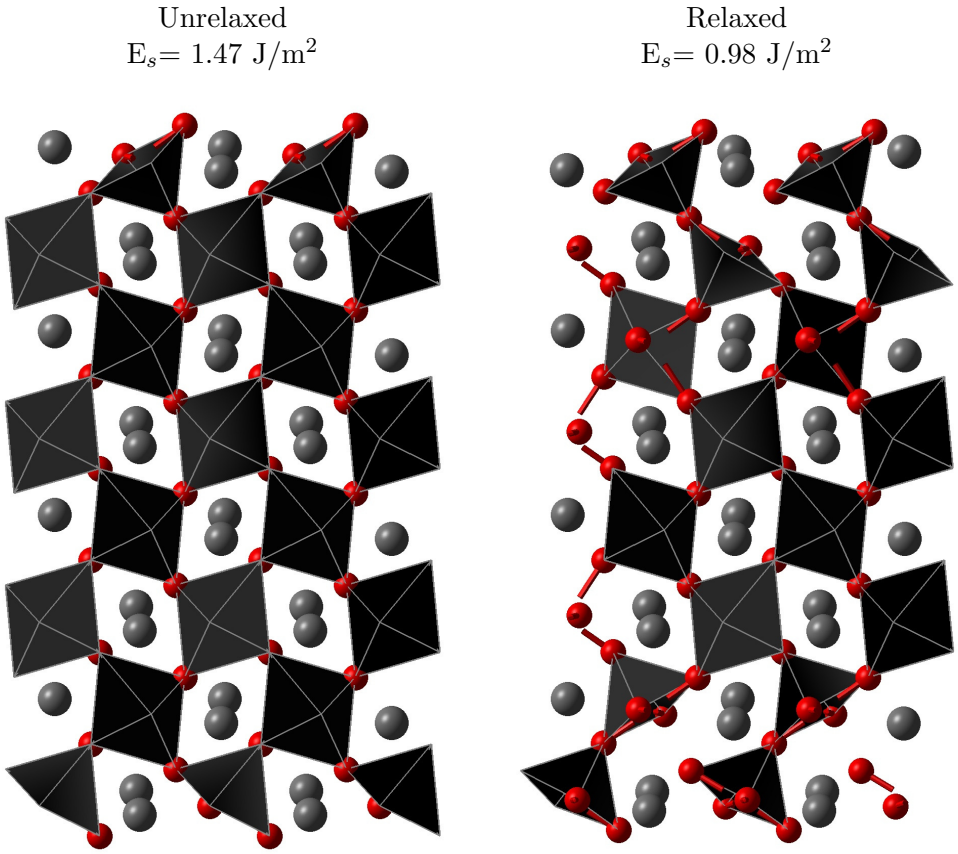

Figure 5.5: The unrelaxed and relaxed slabs of the (100) surface. The unit cell of this surface has been repeated laterally for a clearer depiction of the octahedra. It is normally terminated by two Mn ions, one of which is symmetric to and hidden from view by the visible one. See Fig. 5.2 for details.

5.3 The Jahn Teller Effect and Transition Metal Ion Undercoordination

In order to fully explain the trend of surface formation energy for the orthorhombic AAF phase of $LaMnO_3$, it is necessary to consider not only the average Mn coordination at the surface when it is cleaved from the bulk, as described above, but also the type of Mn-O bond cleaved, the presence of undercoordinated Mn and O ions in the same octahedron and the polarisation of the undercoordinated ions. These factors were not considered in the previous works [29,167], but are of similar importance to the number of cleaved transition metal to oxygen bonds.

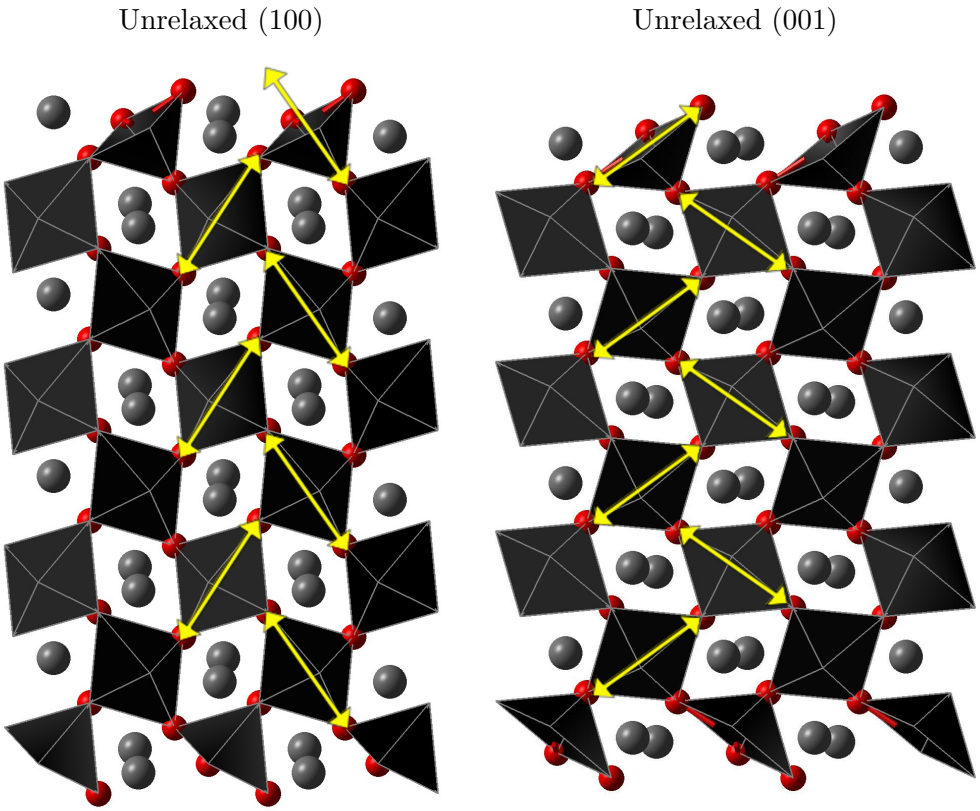

Figure 5.6: The slabs of the unrelaxed (100) and (001) surface, with arrows indicating the direction of the elongating apical (longest Mn-O bonds) J-T distortion. The shortening equatorial J-T distortion occurs perpendicular to the arrows (see Fig. 5.2 for details).

The different types of bonds cleaved (apical and equatorial), the total number of Mn ions per cell in the surface layer and E_s are given in Table 5.4. A comparison of

the (100) and (001) surfaces can be used to illustrate the difference that the type of bond cleaved makes to the surface energy. In Fig. 5.6 the arrows indicate the direction of the apical bonds; it is clear that the orientation of the octahedra is such that, upon cleavage of the the (100) surface, a relatively weak (the longer apical) bond is cleaved. This requires less energy than cleaving the (001) surface, where a relatively strong (the shorter equatorial) bond is cleaved. Hence, the (100) surface has a lower E_s than the (001) surface, despite having the same number of cleaved Mn-O bonds overall.

Table 5.4: The unrelaxed surface formation energy $E_s^{\text{Unrelaxed}}$ of the stoichiometric Type 2 surfaces of orthorhombic ($Pnma$) AAF $LaMnO_3$. N_{Mn} is the number of Mn ions at the termination, Ap^{cleaved} is the number of cleaved apical Mn-O bonds at the surface and Eq^{cleaved} is the number of cleaved equatorial Mn-O bonds. Remaining notation is as in Table 5.3.

Miller Indices	N_{Mn}	Mn^{coord}	Ap^{cleaved}	Eq^{cleaved}	$E_s^{\text{Unrelaxed}}(\text{J/m}^2)$
(1 1 0)	2	4.5	2	1	2.67
(0 0 1)	2	5	0	2	2.52
(1 0 1)	4	5.5	2	0	2.25
(1 0 0)	2	5	2	0	1.47

The order of stability of the studied surfaces is in general agreement with the assumption that cleaving an apical Mn-O bond is more facile than cleaving an equatorial Mn-O bond. The (110) surface has the highest E_s with 1 equatorial and 2 apical bonds cleaved, and the second highest E_s corresponds to the (001) surface with 2 equatorial bonds cleaved. The remaining two surfaces both have 2 apical bonds cleaved and therefore are the lowest in energy. However, there is large discrepancy between their energies, which cannot be rationalised by considering only the type of Mn-O bond cleaved at the surface. The difference in energy between the (101) and (100) surfaces can be further analysed in terms of the cleavage costs of the bonds, which can be approximated by the unrelaxed surface formation energy normalised with respect to the number of bonds rather than the surface area. The (001) surface energy implies an equatorial bond cleavage energy of 5.85×10^{-19}J/bond. The energies of apical bond cleavage are 3.20×10^{-19}J/bond and 7.14×10^{-19}J/bond, when evaluated from the (100) and (101) surface energies, respectively. The (110) surface contains both apical and equatorial bonds; if we substitute the equatorial bond energy obtained from the (001) surface, the resulting apical bond cleavage energy is determined as 4.42×10^{-19}J/bond. This suggests that the energy of the apical bond cleavage for the (101) surface is exceptionally high.

The higher cost of apical bond cleavage and the corresponding higher surface formation energy of the (101) surface can be studied further by considering the differences in the local structure at the surface terminations. Upon cleaving the (101) surface (see

Fig. 5.4), undercoordinated Mn ions and undercoordinated O ions are exposed, with each undercoordinated ion in a separate octahedron. The cleavage of the (100) surface, instead, produces an undercoordinated O and undercoordinated Mn in the same octahedron (see Fig. 5.5). This is the main reason for the higher bond cleavage energy of the (101) surface. A simple ionic model can be used to rationalise the differences in energy, based on the electrostatics of the cleaved octahedra. If an octahedron is cleaved so that an O ion is left monocoordinated (O ions normally coordinate to 2 Mn ions), the O ion polarises, maximising the attractive interaction with the remaining Mn ion and increasing its effective coordination. Similarly, if an octahedron is cleaved so that an Mn is 5-coordinated, the Mn ion will polarise and maximise the attractive interaction with the remaining O ions in order to increase its effective coordination. In the instance that an octahedron contains both an undercoordinated O and Mn, as in the (100) surface, then the polarisation of both ions works cooperatively so that the coordination loss of both of the ions is efficiently compensated, resulting in a lower cost of cleavage. This compensation mechanism is present in all of the surfaces, except the (101) surface where the undercoordinated ions are in separate octahedra. To the author's knowledge this mechanism, which has a significant effect on the relative surface energies and thus crystallite morphology, has not been described previously.

5.4 Electron Density Difference Maps

The polarisation of the electron density on the unrelaxed surfaces due to loss of ion coordination can be explored by mapping the electron density difference with respect to a superposition of the spherical charge density of the ions (Mn^{3+}, O^{2-}), as presented in Figs. 5.7 and 5.8 At both the (100) and (101) surfaces, it is evident that the Mn ions polarise in order to reduce the electron density in the planes of the short equatorial bonds – this decreases the strong repulsion between Mn $3d$ electrons and the equatorial O ions. Consequently, the Mn electron density along the longer apical bond direction increases – where the repulsion from the apical O ions is lower. This behaviour is simply a consequence of the Mn^{3+} d^4 J-T distortion and is also seen in the bulk crystal.

In addition to the polarisation due to the J-T distortion, undercoordinated surface ions polarise in order to increase their effective coordination, and thus offset some of the cost of cleavage. On the difference map of the (100) surface there are 2 notable features:

1. The electron density of the 5-coordinated Mn spreads out towards the region left

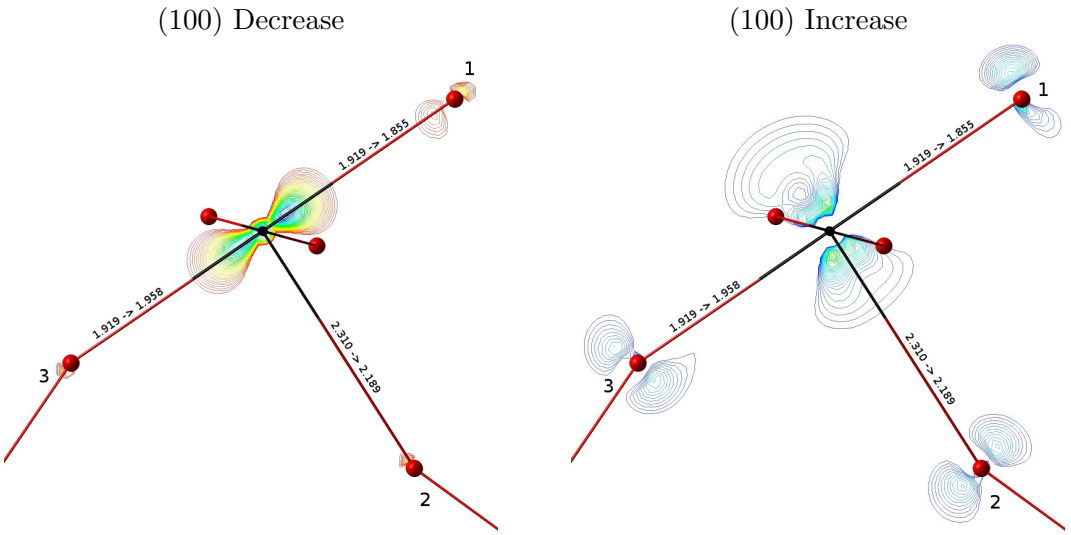

Figure 5.7: Difference maps (increase and decrease) between the electron density of the Mn centred octahedra at the (100) surface and a spherical reference density of ionic superpositions (Mn^{3+} and O^{2-}). The unrelaxed 5-coordinated Mn on the (100) surface is presented with the oxygen atoms in the plane of the electron density slice labelled from 1 to 3. The bond distances before -> after relaxation are given along the bonds in Å. The maps are all generated using 50 contours. The isovalue ranges, measured in e/Bohr^3, are: -0.30 to -0.02 (decrease) and 0.02 to 0.21 (increase).

vacant by the cleaved apical O ion, evident by the enlarged contours above the Mn ion and the smaller contours in the direction of the remaining apical Mn-O bond. This reduces the repulsion between the Mn 3d electrons and the remaining apical oxygen ion (labelled as "2" in Fig. 5.7), and is related to the reduction in bond length from 2.31Å to 2.19Å upon relaxation.

2. The electron density of the monocoordinated O along its remaining bond is reduced (see O "1" in left of Fig. 5.7), which, in combination with the polarisation of the Mn ion, results in a significant decrease in repulsion between the Mn 3d electrons and the O ion. This is related to the shortening of this equatorial bond from 1.92Å to 1.86Å upon relaxation.

Both of these effects result in polarisation that works to increase the effective coordination of the undercoordinated ions and thus stabilising the surface. The difference maps of the (101) surface are displayed in Fig. 5.8 **a** for the octahedron containing the monocoordinated O (O "1"), and Fig. 5.8 **b** for its neighbouring octahedron containing the 5-coordinated Mn. The polarisation effects present on this surface are more complex than the (100) surface, because the undercoordinated ions (5-coordinated Mn and

monocoordinated O) occupy separate (neighbouring) octahedra. The notable features of the maps are detailed below:

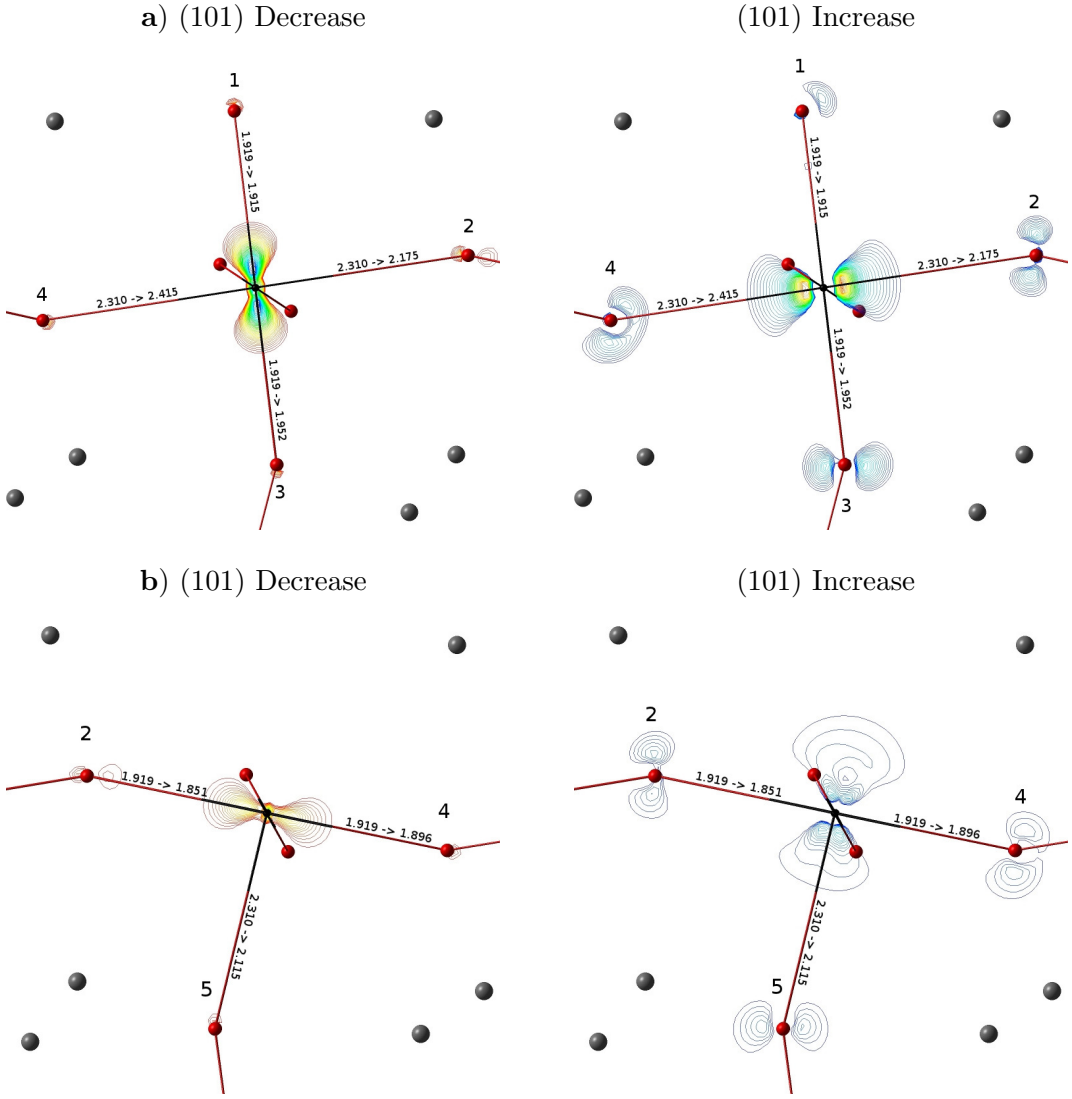

Figure 5.8: Difference maps (increase and decrease) between the electron density of the Mn centred octahedra at the (101) surface and a spherical reference density of ionic superpositions (Mn^{3+} and O^{2-}). **a**) is the unrelaxed 6-coordinated Mn on the (101) surface, with the oxygen atoms in the plane of the electron density slice labelled 1 to 4. **b**) is the unrelaxed 5-coordinated Mn on the (101) surface, with the oxygen atoms in the plane of the electron density slice labelled 2, 4 and 5, referring to the O ions bridging the 6-coordinated Mn (2 and 4) and an additional O (5). The isovalue ranges, measured in e/Bohr^3, are: -0.30 to -0.02 (decrease) and 0.02 to 0.15 (increase).

1. The polarisation of the monocoordinated O of the (101) surface is different to that

in the (100) surface as it does not involve a decrease of the O electron density along the O-Mn bond (see O "1" in left of Fig. 5.8 **a**). This is likely to be due to the absence of any cooperative polarisation from the 6-coordinated Mn, which does not require an increase in coordination. Since the O ion is unable to polarise to increase its effective coordination, the cleavage of the surface becomes more costly. The absence of any attractive polarisation from the monocoordinated O is evident by the relatively minor change in the O "1"-Mn bond distance upon relaxation.

2. The electron density difference around the 6-coordinated Mn on the (101) surface remains constrained and symmetric (Fig. 5.8 **a**), behaving similar to that of the bulk Mn ion, while the electron density difference around its neighbouring 5-coordinated Mn (Fig. 5.8 **b**) is similar to that of the 5-coordinated Mn on the (100) surface (Fig. 5.7). Notably, there is a comparable reduction in the bond length between the 5-coordinated Mn and the remaining apical O, labelled as "5" in Fig. 5.8 **b** (2.310Å to 2.115Å upon relaxation). The 5-coordinated Mn on the (101) surface is therefore also able to polarise to offset some of the cost of cleavage.

3. The strong polarisation of the 5-coordinated Mn is favourable, however, it also results in additional repulsive interactions for the neighbouring 6-coordinated Mn. The O labelled as "4" in Fig. 5.8 **a** and 5.8 **b** bridges the two Mn ions and polarises its electron density to reduce its repulsion to that of the 5-coordinated Mn. As a result, the O electron density is shifted towards the 6-coordinated Mn (note the shape of the O "4" electron density in Fig. 5.8 **a**), significantly increasing the repulsion between itself and the $3d$ electrons of the 6-coordinated Mn. This repulsion will contribute to the higher cost of cleavage and is evident by the large increase in the length of this bond from 2.310Å to 2.415Å upon relaxation.

These effects further make it clear that undercoordinated ions polarise to increase their effective coordination. In particular, it evident from the (101) surface that, if a surface is cleaved so that undercoordinated counterions do not share the same octahedron, the polarisation of the ions can cause a disruptive electron repulsion that destabilises the surface and results in a higher cost of cleavage. The relaxation of such a surface will then work to restore the effective coordination of the undercoordinated ions to the bulk level.

To summarise, the main factors that affect the surface formation energy are:

- The strength and number of Mn-O bonds cleaved at the surface (equatorial vs apical)
- Whether undercoordinated counterions are bound to each other to compensate for coordination loss (undercoordinated Mn and O sharing the same octahedron)
- The relaxation of the surface resulting from the polarisation of the electron density of the undercoordinated ions (aimed at restoring the effective coordination).

5.5 Crystal Shape and Manganese Sites

The computed surface energies have been used to predict the equilibrium crystal morphology based on a Wulff construction (see Fig. 5.9). It is important to highlight here that this Wulff construction is based on the restricted set of low-index surfaces and non-polar unreconstructed terminations. A crystallite in the AFC environment can potentially exhibit other surfaces, terminations and stoichiometries. Using this simplified representation we are able to study the the effects of Jahn-Teller distortion, mechanisms of surface stabilisation and the nature of reaction sites in a controlled environment. This also provides the basis for systematic studies of other surfaces and terminations in the future.

The plot shows that the (100) surface is dominant, contributing 32% surface area (see Table 5.5). This is as expected, since the (100) surface has the lowest formation energy. The (001) and (101) surfaces also make a contribution to the area in proportion to their formation energies. It is notable that due to its orientation, the (110) surface contributes a large area (27.8%), even though it has the highest formation energy.

Table 5.5: The Mn sites, % surface area (from the plot in Fig. 5.9) and formation energies E_s (in J/m^2) of the stoichiometric Type 2 surfaces of orthorhombic ($Pnma$) AAF $LaMnO_3$. The superscripts ^{Ap} and ^{Eq} refer to apical and equatorial bindings sites respectively (i.e. the type of O ion cleaved to form the site).

Miller Indices	E_s^{Relaxed}	Surface Area (%)	Mn Sites
(1 1 0)	1.98	27.8	1 MnO_5^{Ap} & 1 MnO_4^{Ap+Eq}
(0 0 1)	1.39	19.9	2 MnO_5^{Eq}
(1 0 1)	1.36	20.1	2 MnO_5^{Ap}
(1 0 0)	0.98	32.3	2 MnO_5^{Ap}

As part of a study on an AFC catalyst surface, it is useful to classify the various types of reaction (Mn) sites that are available on the surfaces, where the ORR can take place [6, 7]. All of the surfaces studied are characterised by 5-coordinated Mn adsorption sites; 4-coordinated Mn adsorption sites also exist, but are present on only

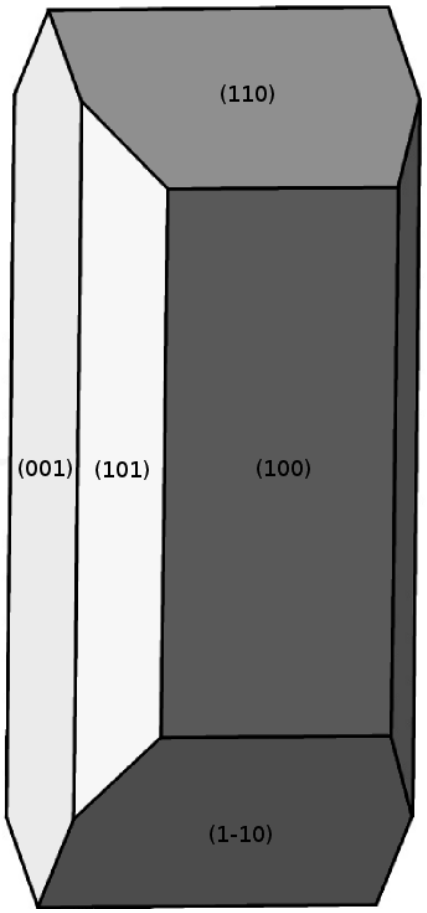

Figure 5.9: Wulff plot showing the equilibrium crystal morphology based on the relaxed surface formation energies.

the (110) surface. In the equilibrium crystal morphology 18.6% of the Mn sites available are 4-coordinated ($\frac{2}{3}$ of the (110) sites, see Table 5.5), while the remainder (81.4%) are 5-coordinated. The sites are also distinguished by the changes in Mn-O bond distance due to J-T distortion and surface relaxation. If we take only the J-T distortion into consideration, we are left with four distinct Mn sites: MnO_4^{Ap}, MnO_4^{Eq}, MnO_5^{Ap} and MnO_5^{Eq}, where the labelling is based on the bond distance of the O ion cleaved to make the site. It is expected that the equatorial sites will bind adsorbates strongly while the apical sites will bind adsorbates weakly. The types of site available on each surface are presented in Table 5.5, and the total contribution of each site is: MnO_5^{Ap} - 61.7%, MnO_5^{Eq} - 19.9%, MnO_4^{Ap} - 9.3%, MnO_4^{Eq} - 9.3%.

The activity of a reaction is likely to be critically dependant on the strength with which a reactant adsorbs on a catalyst site, where a balance between strong and weak

adsorption is sought. This has been shown to be the case for the ORR reaction on a range of perovskites where the binding strength between the transition metal site and O_2 has been found to be near optimal on a $LaMnO_3$ powder sample prepared via a co-precipitation method [7]. In this study, however, the range of adsorption sites available on the $LaMnO_3$ powder and the differences in binding strength that J-T distortion could introduce were not considered. Based on the current work it is likely that a further distinction related to the type of site is possible. The investigation of these adsorption sites is key to the optimisation of ORR catalysis in AFCs. Once the best adsorption sites have been identified, using our understanding of the surface thermodynamics it may be possible to tailor the $LaMnO_3$ crystal morphology and increase the proportion of sites which are more active [29, 190].

5.6 Summary

In this chapter a detailed investigation into the structure and energetics of the unreconstructed stoichiometric surfaces of orthorhombic AAF $LaMnO_3$ using hybrid-exchange density functional theory has been presented. The order of stability for the surfaces has been determined to be (low energy) (100)<(101)<(001)<(110) (high energy). The calculated equilibrium crystal morphology indicates that the surface area contribution of the (100) surface is dominant (32.3%), followed by the contribution of the (110) surface (27.8%). The most widely available adsorption site for the oxygen reduction reaction is an apically cleaved MnO_5 octahedra, making up to 61.7% of the Mn sites. The second most widely available site is an equatorially cleaved MnO_5 octahedra, at 19.9% of the Mn sites.

Analysis of the surface terminations with respect to the surface formation energies has revealed that the Mn coordination is insufficient to explain the relative stability of the surfaces, contrary to previous work [29, 192]. It is also necessary to consider; 1) the strength and number of cleaved Mn-O bonds, 2) the compensation of undercoordinated ions at the terminations and 3) the relaxation from the bulk geometry.

These factors form the basis for rationalising the surface formation energy in transition metal oxides. Equally, the crystal morphology and predicted adsorption sites provide the groundwork for analysing the catalytic activity of $LaMnO_3$, which will be pursued in subsequent work.

6

Oxygen Adsorption on Orthorhombic $LaMnO_3$

6.1 Introduction

The structure and adsorption sites of the stoichiometric and non-polar surfaces of $LaMnO_3$ have been studied in Ch. 5. As demonstrated, there are six types of Mn sites available from the range of surfaces studied. Beyond the structural analysis carried out previously, these sites can be further characterised by simulating the adsorption of ORR species, such as those in Fig. 1.5, in order to gain an understanding of the adsorbate-site interactions. In particular, certain steps of the ORR mechanism are identified as rate-limiting, such as the initial binding of O_2 (by displacement of OH^- as indicated in Fig. 1.5) [7]. Simulating the adsorbtion of O_2 on the sites should, therefore, allow us to evaluate the activity of each site based on strength with which O_2 binds. This exploits the concept discussed previously, where a middle ground is sought between overly strong or weak binding of adsorbates for higher catalytic activity [77].

In the past the adsorption of O_2 on the $LaMnO_3$ surface has been investigated in only a few computational studies, which, as discussed in Sec. 1.3, focus mainly on the cubic phase for SOFC applications [73,74,194,195]. Due to the structural differences of the cubic and orthorhombic phases, these studies are not very relevant for evaluation of the ORR in the AFC. In particular, the lack of J-T distortion on the cubic phase, which, as shown in Sec. 5.5 is a major factor in determining the geometry of the surface reaction sites.

To the author's knowledge the only previous studies of O_2 adsorbtion on orthorhombic $LaMnO_3$ are for the (010) and (001) surfaces [70, 75, 195]. The (010) surface is

actually studied as the (001) surface in the non-standard *Pbnm* setting (see Sec. 5.2), where a range of adsorption modes and binding sites are explored, focusing on SOFC mechanics [70, 195]. On the other hand, in the work studying the (001) surface, only a single adsorbtion site is investigated; a 5 coordinated Mn octahedron (Mn-O_5) [75] It is worth noting here that none of these studies specify if the binding sites are apical or equatorial, while our work in Chapter 5 indicates that the (001) surface should have equatorial distorted Mn sites [75]. This may be due to their choice of standard DFT functionals, which are not able to properly describe the J-T distortion of the octahedra (as discussed in Ch. 5).

It is evident from literature that a full understanding of the nature of O_2 adsorption on the surfaces of orthorhombic $LaMnO_3$ has yet to achieved. In this chapter, therefore, a thorough characterisation of the binding interaction of O_2 on the full range of sites available on the low-index, stoichiometric and non-polar surfaces of $LaMnO_3$ will be provided.

Following this introduction, the methodology for adsorbing molecules on the surfaces and calculating their binding energies is described. The computational details for these calculations are as provided in Sec. 2.6. The result sections include atomic models of the adsorption modes of O_2 on the surfaces and their respective binding energies. These energies are analysed with respect to catalytic activity and the data available in previous literature, after which conclusions are drawn with regards to the ORR activity of the sites and surfaces.

6.2 Binding Energies of Adsorbed Molecules

In this chapter, the simulations require adsorbtion of O_2 molecules on the various Mn adsorbtion sites identified in Chapter 5. This is achieved by placing an O_2 molecule on the Mn site "end-on", at a distance reflecting the type of Mn-O bond cleaved when forming the surface, followed by a geometry optimisation. The O_2 molecule placement is demonstrated in Fig. 6.1 where, as indicated, the molecule is adsorbed on both upper and lower surfaces in order to retain symmetry and prevent generation of a macroscopic dipole.

After the adsorbate-substrate system has been relaxed, it is possible to determine the binding energy of the O_2 molecule. This binding energy **BE**, can be defined in terms of the computed total energies of the adsorbate-substrate system $\mathbf{E}_{sys}$, molecule $\mathbf{E}_{mol}$ and surface $\mathbf{E}_{sur}$ [196]:

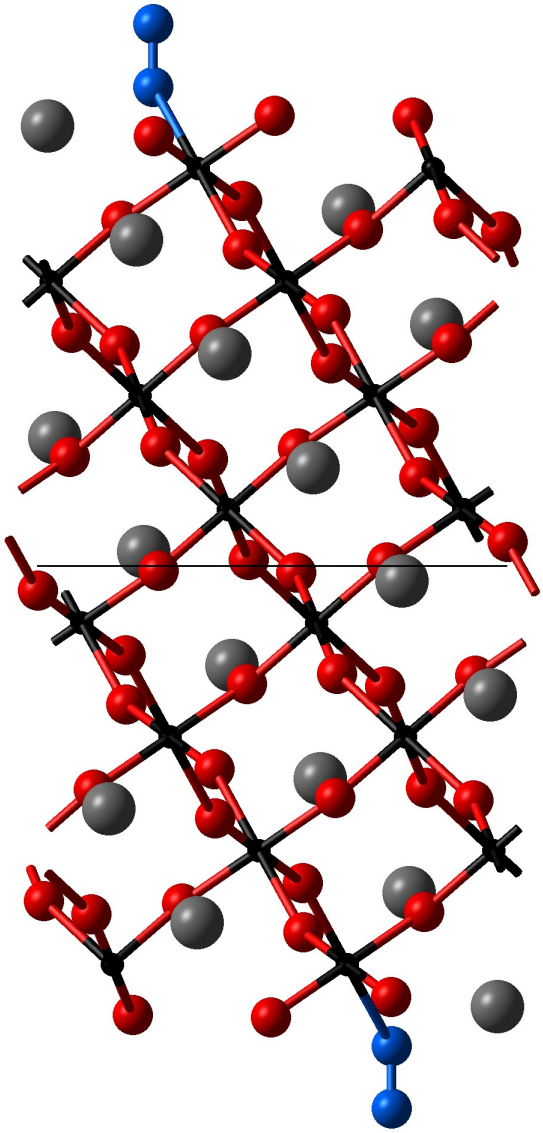

Figure 6.1: The (110) surface with an O_2 molecule (blue) adsorbed on an apical Mn site (MnO_5^{Ap}), before relaxation. The lattice Mn, O and La are represented by the small black, medium red and large grey spheres respectively.

$$\mathbf{BE} = \mathbf{E}_{sys} - (\mathbf{E}_{mol} + \mathbf{E}_{sur}) \tag{6.1}$$

The BE thus obtained can be compared to the energy of adsorption $\mathbf{E}_{ads}$ of a molecule, which is measured by calorimetric techniques or estimated from temperature programmed desorption (TPD) [52,196]. However, this definition is quite simplistic and

does not take into account basis set superposition error (BSSE), which relates to the increase in stabilisation of the overall adsorbate-substrate system due to the provision of larger basis set for the overall system than its component systems. In order to correct for this BSSE and obtain a more accurate BE, it is necessary to implement the counter-poise (CP) correction [141]. For this purpose it is useful to redefine the BE in terms of the energy required to distort a system from its isolated state to that after adsorption $\mathbf{E}_{dis}$, and the interaction energy between the subsystems already distorted to the geometry of the overall system $\mathbf{E}_{int}$ [196]:

$$\mathbf{BE} = \mathbf{E}_{dis} + \mathbf{E}_{int} \tag{6.2}$$

$\mathbf{E}_{dis}$ is obtained separately for both the surface $\mathbf{E}_{dis}^{sur}$ and the adsorbate molecule $\mathbf{E}_{dis}^{mol}$:

$$\mathbf{E}_{dis}^{sur} = \mathbf{E}_{sur|sys} - \mathbf{E}_{sur} \tag{6.3}$$

$$\mathbf{E}_{dis}^{mol} = \mathbf{E}_{mol|sys} - \mathbf{E}_{mol} \tag{6.4}$$

where $\mathbf{E}_{sur|sys}$ and $\mathbf{E}_{mol|sys}$ refer to the energy of the isolated substrate and adsorbate subsystems at the geometry adopted in the overall system. As the energies required to obtain $\mathbf{E}_{dis}$ in Eq. 6.3 and Eq. 6.4 are calculated from the same basis set, there is no BSSE in the energy of distortion. On the other hand, the calculation of $\mathbf{E}_{int}$, which is defined as:

$$\mathbf{E}_{int} = \mathbf{E}_{sys} - (\mathbf{E}_{mol|sys} + \mathbf{E}_{sur|sys}) \tag{6.5}$$

would require three different basis sets to account for each component and therefore incurs BSSE. To overcome this we can instead determine the CP-corrected interaction energy $\mathbf{E}_{int}^{CP}$ [126, 196]:

$$\mathbf{E}_{int}^{CP} = \mathbf{E}_{sys} - (\mathbf{E}_{mol|sys}^{G} + \mathbf{E}_{sur|sys}^{G}) \tag{6.6}$$

which uses "ghosted atoms" (^{G}) in order to include the full basis set of the adsorbate-substrate system when determining the energies of the subsystems. The CP-corrected binding energy $\mathbf{BE}^{CP}$ is thus obtained by [126, 196]:

$$\mathbf{BE}^{CP} = \mathbf{E}_{sys} - (\mathbf{E}_{mol|sys}^{G} + \mathbf{E}_{sur|sys}^{G}) + (\mathbf{E}_{sur|sys} - \mathbf{E}_{sur}) + (\mathbf{E}_{mol|sys} - \mathbf{E}_{mol}) \tag{6.7}$$

In addition to accounting for BSSE between the adsorbate and substrate, it is important to be aware of the effect of any intermolecular interactions between adsorbed molecules. Since the surface is simulated as a two dimensional slab, a single molecule adsorbed on the surface represents a periodic array (i.e. a monolayer) of molecules on the surface. If the cell parameters are small, it is possible that lateral interactions between molecules can occur, which results in a unique binding energy for an adsorbed monolayer rather than that for the adsorbed molecule.

Interactions and distortions due to the intermolecular distances are checked by comparing the energy of one unit cell of a geometry optimised free monolayer against the energy of its isolated and optimised component molecule. If there are no lateral interactions in the monolayer these energies will be qualitatively identical and the periodic array of adsorbed molecules can be used to obtain binding energies as described in Eq. 6.7. It is, however, also necessary to check for BSSE between the molecules in the periodic array. This can be carried out simulating a supercell of the adsorbate at the geometry of the overall system, where the neighbouring adsorbate molecules are "ghosted" atoms that include only the basis sets. The $\mathbf{E}_{dis}^{mol}$ obtained using the "ghosted" supercell system should be qualitatively identical to the $\mathbf{E}_{dis}^{mol}$ obtained normally as in Eq. 6.4 if there is no BSSE between adsorbate molecules.

For the calculations carried out in this chapter, the existence of lateral interactions and BSSE between adsorbed O_2 was confirmed to be negligible by the methods detailed above using O_2 adsorbed on the (100) surface. This surface has the smallest lattice parameters (5.614 Å and 7.735 Å as reported in Table 5.1) and thus the shortest intermolecular distances between adsorbed O_2.

6.3 Adsorption Modes of O_2

As was depicted in Fig. 6.1, the O_2 molecules have been adsorbed with an initial, vertical aligned "end-on" position onto the adsorption sites. This initial adsorption mode was subjected to geometry optimisation, which revealed the ground state configurations for the adsorbed O_2 molecules on the various $LaMnO_3$ surfaces studied. In order to quantitatively analyse the nature of O_2 binding on these surfaces, atomic models of the O_2-$LaMnO_3$ system are discussed with respect the interatomic distances between the O atoms of the adsorbed molecules and the Mn of the adsorption site.

Analysis of local geometry is also carried in terms of the Jahn-Teller distortion of the adsorption sites (as highlighted in Ch. 5) in order to evaluate its effect on the binding modes of O_2. The relaxation of the overall surface structure upon adsorption

of the molecules is not analysed in detail, but is naturally accounted for due to its contribution to the determined binding energies, which are discussed in Sec. 6.4.

In the following sections the adsorption sites of each of the surfaces studied are analysed with respect to the adsorption of a single O_2 per unit cell of the surface, irrespective to the number of sites available. The (100) and (001) surfaces are first compared before the more complex adsorption sites of the (101) and (110) surfaces are analysed.

6.3.1 The (100) Surface

The (100) surface has adsorption sites of Mn, which are coordinated by 5 lattice O ions. Since the O ion cleaved to form the site (Mn is coordinated by 6 O ions in the bulk) was bound at the bulk apical bond distance, this adsorption site will be referred to by the notation MnO_5^{Ap}, as detailed in Sec. 5.5. In Fig. 6.2 the adsorbed O_2 molecule is shown bound to one of the two available MnO_5^{Ap} sites of the (100) surface. The repeat units of the adsorbed molecule and surface unit cell are included in the figure to allow for an evaluation of the local environment of the adsorbed molecule. The periodicity of the surface unit cells are indicated by repetition of the single adsorbed molecule. The molecule largely retains the initial end-on orientation after relaxation of the geometry, although, as can be seen from the side view in Fig. 6.2b, there is a tilt of the distal O (the O atom of the O_2 molecule furthest from the surface) towards the neighbouring vacant MnO_5^{Ap} adsorption site.

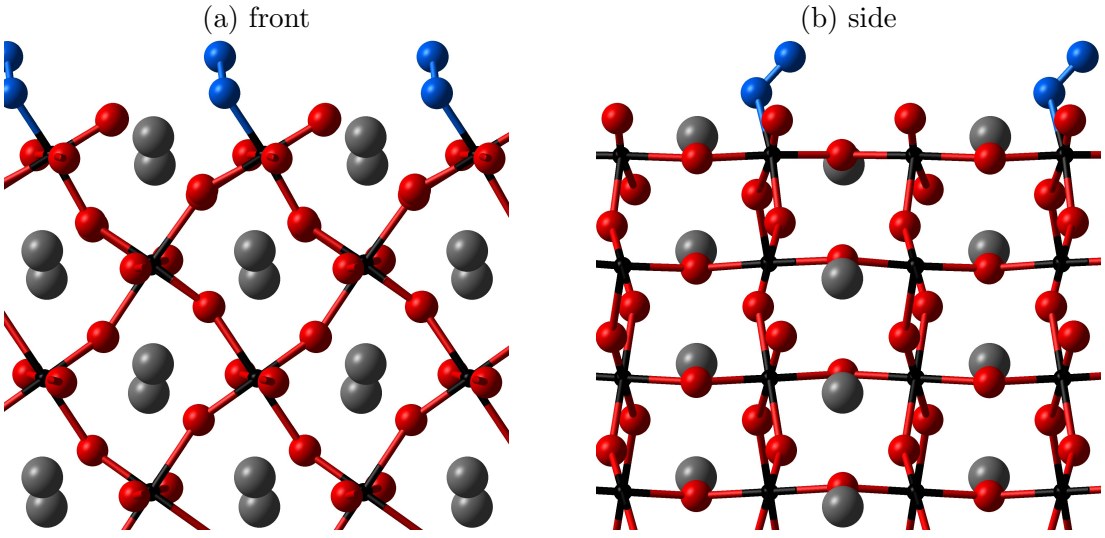

Figure 6.2: Optimised geometry of the (100) surface after an O_2 molecule was initially adsorbed on the MnO_5^{Ap} site with a front (a) and side (b) view.

The O-O bond distance d(O-O) for the adsorbed O_2 molecule is 1.31Å, which is longer than that observed for the molecule in the gas phase (1.21Å) and the hybrid (B3LYP) DFT simulation of the isolated molecule (1.23Å) [197]. This is not unexpected since previous studies of O_2 adsorption on various perovskite and noble metal surfaces have shown that d(O-O) increases in length upon adsorption [73, 74, 197]. The Mn-O bond distance d(Mn-O_2) of the surface Mn to the binding O of the adsorbed O_2 molecule is 2.00Å. This is unexpected as it indicates that binding on the apical site is actually closer to the equatorial Mn-O bond distances in the equilibrium bulk geometry, which are 1.92Å and 1.99Å, rather than the apical Mn-O bond distance of 2.31Å. On inspection of the bond distances of the octahedra at the (100) surface, given in Table 6.1, it is clear that surface octahedra undergo an internal relaxation. The greatest effect being the overall shorter Mn-O bond distances in order to increase the effective coordination of the previously undercoordinated Mn ion (this effect is detailed in Sec. 5.4). Perhaps the most notable feature of O_2 adsorbtion on this site is, therefore, that it undergoes only minor changes upon adsorption, predicting a small binding energy. This picture is consistent with the hypothesis that the MnO_5^{Ap} sites are generally weaker binding sites. Furthermore, it would appear that the (100) surface could be the surface of $LaMnO_3$ that is least affected by both the removal (as shown in Ch. 5) or re-addition of its terminal apical Mn-O bond, due to the J-T distortion.

6.3.2 The (001) Surface

The (001) surface has MnO_5^{Eq} adsorption sites, as discussed previously in Sec 5.5. The adsorption of an O_2 molecule on one of the two available sites of this surface is shown in Fig. 6.3. Contrary to the adsorption on the (100) surface, the adsorbed molecule adopts a more lateral orientation, where the tilting of the O_2 molecule is also in the opposite direction to that observed on the (100) surface. The proximity of the distal O atom of the bound O_2 molecule to the surface suggests there is an attractive interaction,

Table 6.1: The bond distances of the O coordinated Mn octahedra at the (100) surface. $MnO_5^{Ap}c$ are the octahedra on the clean (100) surface while MnO_5^{Ap} and MnO_5^{Ap}-O_2 indicate the octahedra with vacant and occupied site respectively after an O_2 molecule is adsorbed. The d(Mn-O_2) is in bold text.

$MnO_5^{Ap}c$(Å)	MnO_5^{Ap}(Å)	MnO_5^{Ap}-O_2(Å)
1.85	1.84	1.80
1.93	1.95	1.89
1.96	1.97	**2.00**
2.02	2.02	2.00
2.19	2.14	2.02
		2.06

Table 6.2: The bond distances of the O coordinated Mn octahedra at the (001) surface. $MnO_5^{Eq}c$ are the octahedra on the clean (001) surface while MnO_5^{Eq} and MnO_5^{Eq}-O_2 indicate the octahedra with vacant and occupied site respectively after an O_2 molecule is adsorbed. The d(Mn-O_2) is in bold text.

$MnO_5^{Eq}c$(Å)	MnO_5^{Eq}(Å)	MnO_5^{Eq}-O_2(Å)
1.85	1.84	1.77
1.96	1.98	1.88
1.96	2.01	1.89
2.12	2.05	1.97
2.17	2.16	**2.07**
		2.25

although clearly the O_2 is still bound through a single O atom.

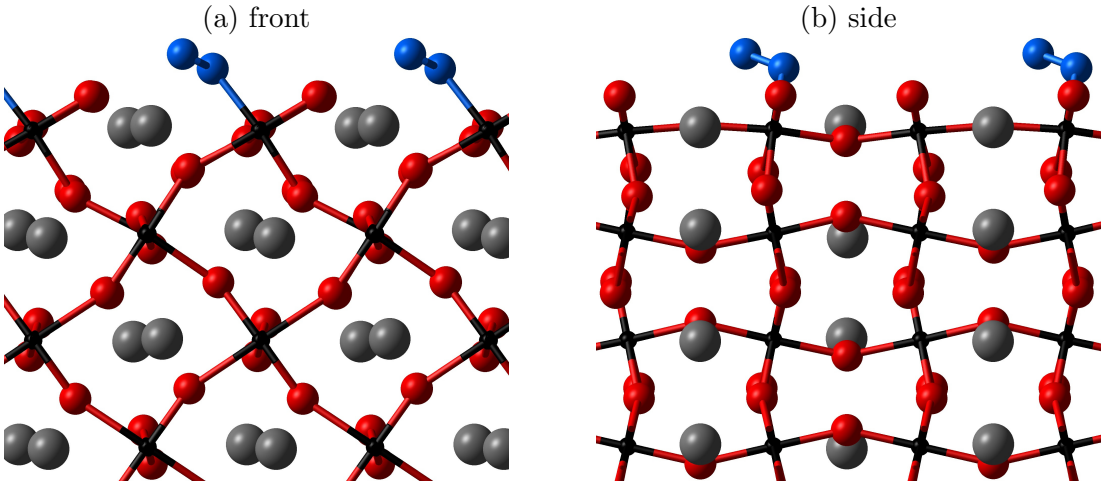

Figure 6.3: Optimised geometry of the (001) surface with an O_2 molecule initially adsorbed on the MnO_5^{Eq} site with a front (a) and side (b) view.

The d(O-O) for the adsorbed O_2 molecule is 1.34Å, which is slightly longer than that observed on the (100) surface (1.31Å). Similarly, the d(Mn-O_2) of 2.07Å is also slightly longer than that observed on the (100) surface. The d(Mn-O_2) on the (001) is quite unexpected since an equatorial site binds O at a much shorter distance than the apical site in the bulk geometry. If we consider the bond distances of the octahedra at the (001) surface (Table. 6.2), it is evident that prior to adsorption the bond distances of the O coordinated Mn octahedra at the (100) surface are very similar to those on the (001) surface. Following adsorption of O_2, however, the now fully coordinated octahedron MnO_5^{Eq}-O_2 further elongates an apical bond in order to balance the increase in coordination. It is also highly likely that, since the octahedra are linked together via Mn-O-Mn bonds, further distortions occur in the lower layers and the neighbouring vacant site MnO_5^{Eq} octahedron (as evident by the changes in bond distance in Table. 6.2),

which also alleviate the effects of adsorption. These changes are likely to occur upon adsorption on all of the studied surfaces and are quantified in terms of the calculated binding energy, which will be discussed in Sec. 6.4

6.3.3 The (101) Surface

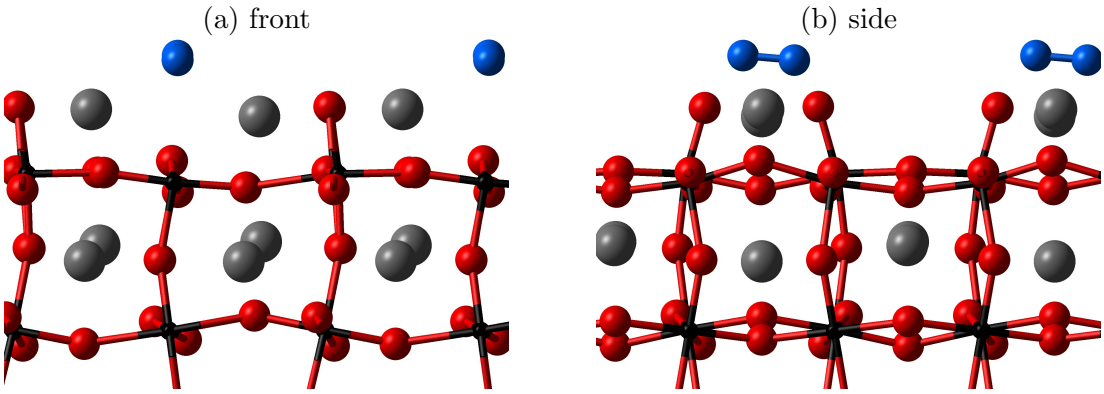

Figure 6.4: Optimised geometry of the (101) surface with an O_2 molecule initially adsorbed on the MnO_5^{Ap} site with a front (a) and side (b) view.

The (101) surface has two MnO_5^{Ap} adsorption sites per unit cell of the surface, as well as two fully O coordinated (MnO_6) Mn octahedra. The adsorption of an O_2 molecule on one of the two MnO_5^{Ap} sites of this surface was attempted, and the results are demonstrated in Fig. 6.4. As evident from the atomic model, the O_2 molecule does not bind to the MnO_5^{Ap} site, but prefers a sideways 'physisorption' like bridging position in the space above and between two La ions, and also between the two MnO_5^{Ap} sites. This adsorption mode of O_2 is completely different than that observed on any of the other studied surfaces of $LaMnO_3$ and can firstly be rationalised by the explanation that the interaction of the available MnO_5^{Ap} (weak binding) site to the O_2 molecule must be less than the attraction from the La ions. This can be further verified in terms of the binding energies in Sec. 6.4, but can also be seen in terms of the structural changes listed in Table. 6.3. The d(Mn-O_2) is included here only to indicate the shortest distance to Mn from O_2 molecule. In fact, one of the O atoms of the O_2 molecule is slightly tilted towards an Mn site, despite otherwise evenly bridging the two MnO_5^{Ap} sites. This slight bias from tilting results in a minor change in the Mn-O bond distances but otherwise the surface structure remains the same after adsorption.

With regards to this physisorption like adsorption, it is important to not overlook the d(O-O) for the adsorbed O_2 molecule, which is 1.36Å. This is larger than that observed on both the (100) and (001) surfaces, and suggests a binding nature that is

Table 6.3: The bond distances of the O coordinated Mn octahedra at the (101) surface. $MnO_5^{Ap}c$ are the octahedra on the clean (101) surface while MnO_5^{Ap} and MnO_5^{Ap}-O_2 indicate the octahedra with vacant and occupied site respectively after an O_2 molecule is adsorbed. The d(Mn-O_2) is in bold text.

$MnO_5^{Ap}c$(Å)	MnO_5^{Ap}(Å)	MnO_5^{Ap}-O_2(Å)
1.85	1.86	1.90
1.90	1.90	1.93
2.03	2.02	1.94
2.11	2.05	2.05
2.12	2.09	2.09
		3.39

contrary to that inferred from the Mn-O bond distances. A large d(O-O) indicates that the adsorption of O_2 in this bridging position is actually stronger than mere physisorption, since physisorbed molecules should only have a weak interaction with the surface and mostly retain their molecular geometry.

The non-preference for O_2 to bind on the MnO_5^{Ap} site of the (101) surface also allows us another insight into the nature of O_2 adsorption on the surfaces of orthorhombic $LaMnO_3$: the attraction of O_2 to the MnO_5^{Ap} site is weak enough that La ions in the local environment are able to provide a better adsorption site. However, there must be certain conditions since the MnO_5^{Ap} site of the (100) surface (Fig. 6.2) still binds. The difference on the (101) surface being that the La ions are further exposed than the MnO_5^{Ap} site.

6.3.4 The (110) Surface

The (110) surface of $LaMnO_3$ is the most complex surface with regards to the adsorption of O_2 since it has 3 types of adsorption site available: MnO_5^{Ap}, MnO_4^{Ap} and MnO_4^{Eq}. For each of these sites an O_2 molecule was adsorbed initially at the position of the cleaved lattice O ion to form the site, as demonstrated in Figs. 6.5-6.7. In order to describe the nature of adsorption on these sites it is more useful to analyse the initial geometry and final preferred geometry for O_2 adsorption. This allows us to understand that, due to their close proximity, particular sites of this surface will be preferred for O_2 adsorption regardless of the initial adsorption state.

Consider the MnO_5^{Ap} site in Fig. 6.5. Here the molecule moves from its vertical end-on position on the MnO_5^{Ap} site by tilting towards the neighbouring MnO_4 octahedron and binding on its equatorial site ($MnO_4^{Eq-Lateral}$). It adopts a lateral position which may allow for a stabilising interaction between the now vacant MnO_5^{Ap} site and the distal (non-binding) O of the O_2 molecule. For the initial adsorption on the MnO_4^{Ap} site in Fig. 6.6, the adsorbed molecule also prefers the equatorial site, going from a vertical

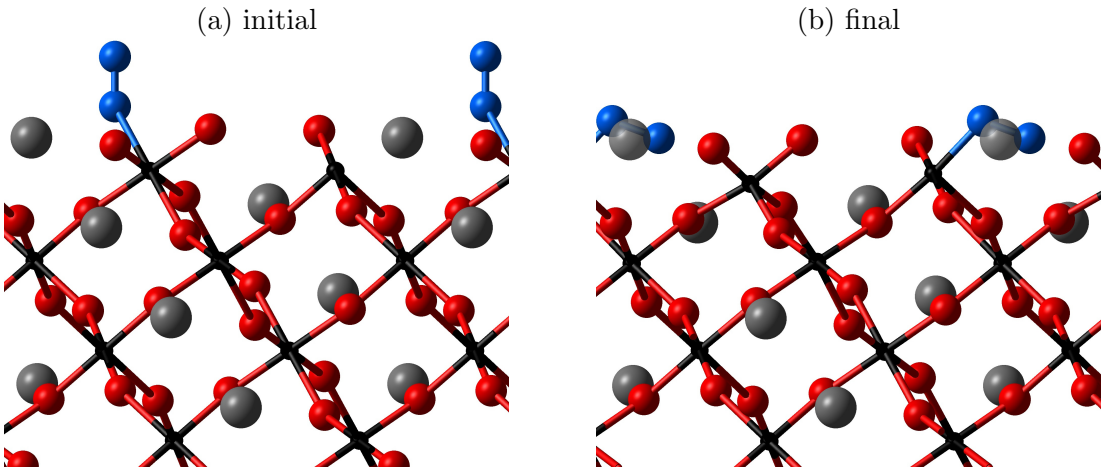

Figure 6.5: The (110) surface with an O_2 molecule adsorbed on the MnO_5^{Ap} site with initial geometry (a) and after relaxation (b). O_2 binding changes from $MnO_5^{Ap} > MnO_4^{Eq}$.

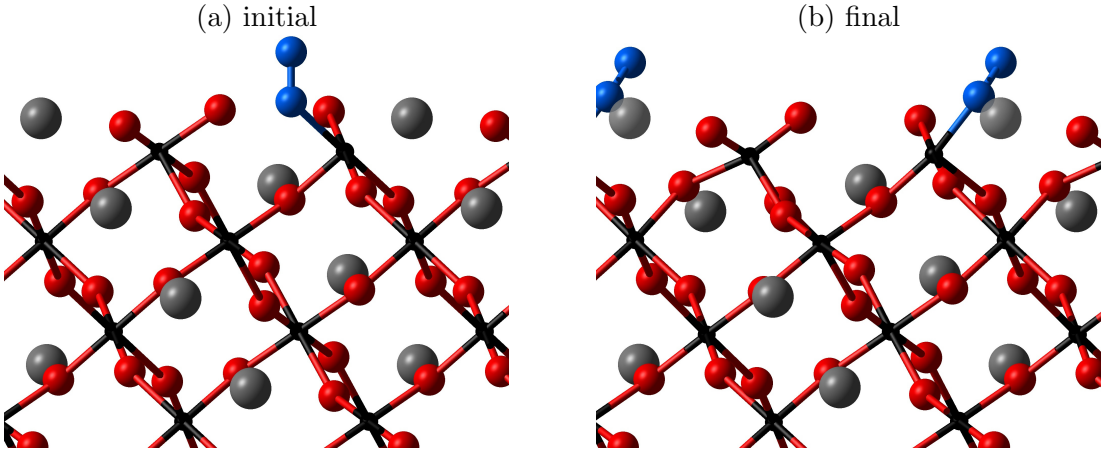

Figure 6.6: The (110) surface with an O_2 molecule adsorbed on the MnO_4^{Ap} site with initial geometry (a) and after relaxation (b). O_2 binding changes from $MnO_4^{Ap} > MnO_4^{Eq}$.

end-on orientation to a diagonal orientation on the $MnO_4^{Eq-End-on}$ site. Lastly, when initially adsorbing on the MnO_4^{Eq} site as in Fig. 6.7, the relaxed geometry results in a unique 'bidentate' binding mode $MnO_4^{Eq-Bidentate}$ where the bond between the O atoms in O_2 remains intact while each atom is also bound to the MnO_4 site. This appears to be a result of the equatorially bound O_2 molecule tilting so that the distal O moves towards the MnO_4^{Ap} site from its initial position. However, this distal oxygen does not exactly occupy the MnO_4^{Ap} site, since its binding angle is restrained by the unbroken O-O bond.

From briefly studying the modes of adsorption it is clear that the adsorption of O_2 is

Table 6.4: The Mn-O bond distance d(Mn-O_2) of the surface Mn to the binding O of the adsorbed O_2 molecule, and the O-O bond distance d(O-O) the adsorbed O_2 molecule on the (110) surface.

Adsorption Mode	d(Mn-O_2)(Å)	d(O-O)(Å)
$MnO_5^{Ap} > MnO_4^{Eq-Lateral}$	1.93	1.48
$MnO_4^{Ap} > MnO_4^{Eq-End-on}$	2.03	1.34
$MnO_4^{Eq} > MnO_4^{Eq-Bidentate}$	1.94	1.46

preferred on the MnO_4^{Eq} site above all other sites of this surface. However, there is some variation in the orientation of the adsorbed O_2 molecule, which may reflect adsorption modes in the real adsorbate-substrate system (i.e. there are some local minima that reflect possible metastable states of O_2 adsorption on this surface). For the structural analysis of these states or adsorption modes, it is useful to directly compare their relative d(Mn-O_2) and d(O-O), which are concisely presented in Table. 6.4.

At the first instance it is clear that the binding on the equatorial site results in a shorter d(Mn-O_2) than observed on other surfaces. This could simply be a result of Mn undercoordination remaining even after adsorption of O_2. The d(O-O) of these adsorption modes, however, can be linked to the orientation of the adsorbed O_2 molecule. In the first case ($MnO_5^{Ap} > MnO_4^{Eq-Lateral}$) the d(O-O) of 1.48Å is likely due to the lateral tilting of the adsorbed O_2 molecule towards the vacant MnO_5^{Ap} site where the attraction of the distal oxygen stretches the O-O bond. This is verified by the fact that adsorption on the same site but with more vertical orientation, as in the second adsorption mode ($MnO_4^{Ap} > MnO_4^{Eq-End-on}$), involves no such attraction of the distal oxygen and therefore no stretching of the O-O bond. In the third mode of adsorption ($MnO_4^{Eq} > MnO_4^{Eq-Bidentate}$), the O-O bond of the O_2 molecule is stretched by attraction of distal O atom towards the apical site of the same octahedron. Although the discussion of O_2 adsorption on the $LaMnO_3$ surface will now move onto the binding energies, it is important to highlight that the d(Mn-O_2) and d(O-O) of the O_2 adsorption modes on this surface are not only useful since they give insight into the local interactions at the surface, but also because in future they can be linked to vibrational frequencies and bond distances obtained from experiment, allowing for the identification of O_2 adsorption modes in real systems.

6.4 Energetics and Electronic Properties

6.4.1 BSSE Correction

As indicated in the previous section, the adsorption mode of O_2 on the surfaces of orthorhombic $LaMnO_3$ varies to a great degree, depending on the nature of the adsorp-

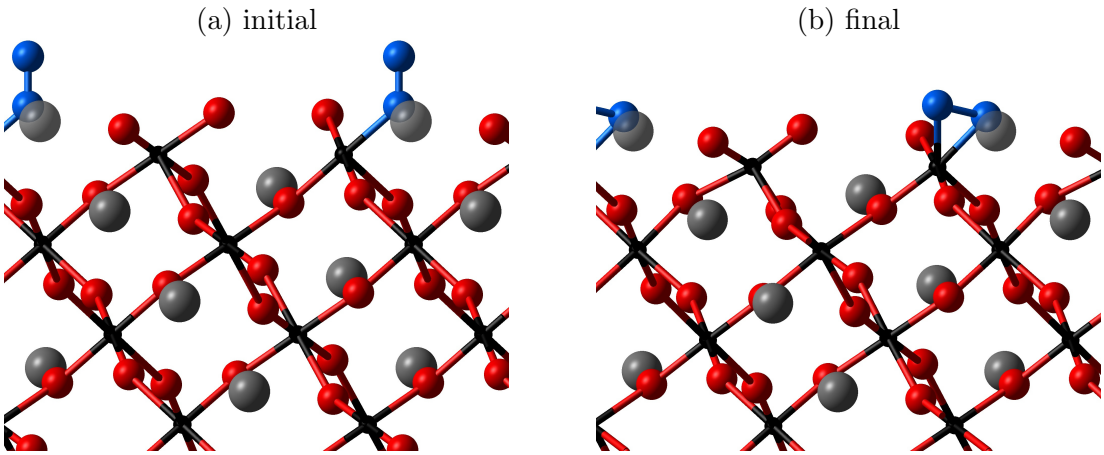

Figure 6.7: The (110) surface with an O_2 molecule adsorbed on the MnO_4^{Eq} site with initial geometry (a) and after relaxation (b). O_2 binding changes from $MnO_4^{Ap} > MnO_4^{Eq-Bi}$.

Table 6.5: The binding energy **BE** and bond distances of the various adsorption modes of O_2 on the $LaMnO_3$ surfaces, indicating the initial and final adsorption mode where relevant. $\mathbf{BE}^{CP}$ and $\mathbf{BE}^{CP(101)}$ correspond to standard and static (101) BSSE corrections using the counter-poise method (Sec. 6.2). See Table 6.4 for remaining notation.

Adsorption Mode	d(Mn-O_2)(Å)	d(O-O)(Å)	**BE** (eV)	$\mathbf{BE}^{CP}$ (eV)	$\mathbf{BE}^{CP(101)}$ (eV)
(100) MnO_5^{Ap}	2.00	1.31	*-0.35*	*-0.08*	**-0.18**
(001) MnO_5^{Eq}	2.07	1.34	*-0.94*	*-0.61*	**-0.77**
(101) MnO_5^{Ap} > La Bridge	3.39	1.36	*-1.45*	*-1.28*	**-1.28**
(110) $MnO_5^{Ap} > MnO_4^{Eq-Lateral}$	1.93	1.48	*-2.33*	*-1.52*	**-2.16**
(110) $MnO_4^{Ap} > MnO_4^{Eq-End-on}$	2.03	1.34	*-2.60*	*-1.67*	**-2.43**
(110) $MnO_4^{Eq} > MnO_4^{Eq-Bidentate}$	1.94	1.46	*-2.95*	*-2.32*	**-2.79**

tion sites available and the local geometry of the surface. In order to characterise the effectiveness of these sites for the ORR, it is still necessary to determine the strength with which O_2 is bound. The binding energy (**BE**) of each of the adsorption modes identified has therefore been calculated, as detailed in Sec. 6.2, and is presented in Table 6.5 alongside the d(Mn-O_2) and d(O-O) introduced previously.

There are 3 sets of energies presented in Table 6.5, **BE**, $\mathbf{BE}^{CP}$ and $\mathbf{BE}^{CP(101)}$. These correspond to the **BE** energy calculated without correction for BSSE (Eq. 6.1), the CP corrected energy (Eq. 6.7) and the CP corrected binding energy using a static value for the BSSE taken from the (101) surface. As evident by the differences between the **BE** and $\mathbf{BE}^{CP}$, the calculated BSSE is quite significant; for the (001) surface it accounts for 78% of the uncorrected binding energy. Overestimation of the BSSE using the CP method is typically attributed to cases where the basis sets used to describe the component systems of the substrate and molecule are inadequate. In Ch. 3, however, to properly describe the various Mn oxide systems the basis sets have already been

optimised. The overestimation of BSSE in this case is instead largely due to changes in the molecule and substrate upon adsorption.

When determining the BSSE, the CP method expects that the geometry of the isolated subsystems (the clean substrate and free molecule) remain the same in the overall system (substrate with molecule adsorbed) [126, 196, 198]. This is normally the case when the adsorbing molecule physisorbs, but in systems such as ours, a strongly bound O_2 molecule can distort from the geometry it adopts as a free molecule (d(O-O) calculated as 1.23Å compared to those presented in Table 6.5). Similar distortions can also occur to the substrate if the adsorbing molecule significantly stabilises undercoordinated ions (see Ch. 5 for details). In fact, from our calculations it has been determined that although there is a distortion of the adsorbing O_2 molecule, its contribution to BSSE is actually far less than that from the distortions of the surface substrate.

After investigating the change in geometry of the surface and its interaction with the adsorbing O_2, it is apparent that overestimation of BSSE occurs largely due to; 1) relaxation of the surface geometry after O_2 adsorption and 2) a stabilising polarisation of the Mn electron density into the ghost basis set of O_2. In particular, it is found that orbitals of the O_2 basis set that are normally unoccupied in the overall system, become filled with Mn electron density when O_2 is ghosted. This indicates that the exploitation of the empty O_2 orbitals by Mn electron density is further overestimating BSSE.

In order to have a better estimate of BSSE without the issues above, a simple solution is to adopt the quantity of BSSE determined by the CP method for the (101) surface ($\mathbf{BE}^{CP(101)}$). The adsorption of O_2 on this surface provides the lowest overestimation for the CP corrected BSSE since, as discussed in the previous section, O_2 binds at a large distance from the Mn site. This means that the electron density of Mn cannot easily exploit the unoccupied orbitals of the ghosted O_2, while at the same time the distortion of the bulk is minimised since the undercoordination of the Mn site remains the same as the clean surface.

As an additional note regarding the accuracy of the **BE**s calculated here, it is worth mentioning that in a recent study, the binding of O_2 on the (001) surface of orthorhombic (*pnma*) $LaMnO_3$ has been calculated using the plane wave approach to DFT with the GGA functional [75]. The **BE** is reported as -0.66 eV, which is comparable to the $\mathbf{BE}^{CP}$ of -0.77 eV observed here. This suggests that, because the plane wave approach eliminates all BSSE due to the basis set being independent of atomic positions and species, the estimation of BSSE from the (101) surface is reasonably accurate.

Table 6.6: The binding energy **BE** and bond distances of the various adsorption modes of O_2 on the $LaMnO_3$ surfaces, indicating the initial and final adsorption mode where relevant. O_2 q is the charge of the adsorbed O_2 molecules. See Table 6.4 and 6.5 for remaining notation.

Adsorption Mode	d(Mn-O_2)(Å)	d(O-O)(Å)	$\mathbf{BE}^{CP(101)}$(eV)	O_2 q (e)
(100) MnO_5^{Ap}	2.00	1.31	**-0.18**	-0.48
(001) MnO_5^{Eq}	2.07	1.34	**-0.77**	-0.61
(101) MnO_5^{Ap} > La Bridge	3.39	1.36	**-1.28**	-0.74
(110) MnO_5^{Ap} > $MnO_4^{Eq-Lateral}$	1.93	1.48	**-2.16**	-1.24
(110) MnO_4^{Ap} > $MnO_4^{Eq-End-on}$	2.03	1.34	**-2.43**	-0.70
(110) MnO_4^{Eq} > $MnO_4^{Eq-Bidentate}$	1.94	1.46	**-2.79**	-1.04

6.4.2 Adsorption Sites

The negative value of the **BE**s presented in Table 6.5 indicates that it is energetically favourable to adsorb an O_2 molecule on all of the adsorption sites considered. It also appears that the adsorption sites can indeed be separated into the proposed "weakly binding" MnO_5^{Ap} sites and "strongly binding" MnO_5^{Eq} sites, based on their relative **BE**. This classification of O_2 adsorption sites on $LaMnO_3$ is unique from literature, largely because previous studies have not compared the (100) and (001) surfaces of orthorhombic $LaMnO_3$, let alone observed the existence of J-T distorted adsorption sites. In addition to the **BE** and geometry of the adsorbed O_2 molecules, further analysis can be carried out in terms of the charge transfer from the surface to the adsorbed molecule. This information is presented in Table 6.6, in terms of the Mulliken population analysis of the adsorbed molecule, recording the change in charge with respect to the free (neutral) molecule *.

The MnO_5^{Ap} Site

The binding of O_2 on the MnO_5^{Ap} site of the (100) surface appears to be the weakest among all the sites, based on the $\mathbf{BE}^{CP(101)}$ of -0.18 eV. This also coincides with the d(O-O) of 1.31Å, which represents the shortest change from the 1.23Å calculated for the free O_2 molecule. As stated earlier, previous studies of O_2 adsorption have not considered the (100) surface of orthorhombic $LaMnO_3$, and as a result, it is not possible to make any comparison.

The MnO_5^{Ap} site is also present on the (101) and (110) surfaces, however, as demonstrated in Sec. 6.3, the local environment around each site is different. In the case of

*Note that in the bulk-like regions of the $LaMnO_3$ lattice, O ions possesses -1.3 e in mulliken population analysis relative to the free (neutral) molecule. Since O^{2-} is the oxidation state in bulk $LaMnO_3$, a value of -0.65 e in Table 6.6 would be approximately equivalent to the whole O_2 molecule accepting a single electron.

the (110) surface, the MnO_5^{Ap} site is not active to O_2 adsorption since the neighbouring MnO_4^{Eq} site is favoured (this is discussed below). On the (101) surface, the MnO_5^{Ap} site is also not occupied, but the O_2 molecule adopts a bridging position between two La ions (and at a greater distance, the two available MnO_5^{Ap} sites). It is now clear from the **BE**s calculated that this bridging adsorption mode is simply more energetically favourable than the single MnO_5^{Ap} site.

With regards to the chemical state of the adsorbed O_2 molecule, it accepts a charge of 0.48 e, which can be quantified as 74% of a whole electron in the $LaMnO_3$ bulk if the population analysis of $LaMnO_3$ is considered to be representative of formal ionic charges. Based on the charge transfer and lower d(O-O) of the adsorbed O_2, this suggests that O_2 does not fully transform into its superoxide form (O_2^-). The transfer of an electron to adsorbed O_2 is an important factor to consider in the analysis of adsorption sites for the ORR. In various studies the adsorption of O_2 is considered to be a rate limiting step, however, in recent work it is suggested that the molecular adsorption of O_2 is fast and that the subsequent transfer of an electron from Mn to O_2 is slow and limits the rate of reaction [7, 108]. Taking these factors into account, the characteristics of the MnO_5^{Ap} site indicate that it may be active for the ORR, but perhaps kinetically slow due to the relatively weak binding and low electron transfer.

The MnO_5^{Eq} Site

The $\mathbf{BE}^{CP(101)}$ of -0.77 eV for O_2 on the MnO_5^{Eq} site of the (001) surface reflects the change from apical (weak binding) to equatorial (strong binding) J-T distortion; the binding energy on the MnO_5^{Eq} site is over 4 times greater than the MnO_5^{Ap} site on the (100) surface. The d(O-O) of 1.34Å is also greater, further indicating a stronger binding. As discussed in Sec. 6.3, the d(Mn-O_2) on the MnO_5^{Eq} site is actually longer than that for the MnO_5^{Ap}, and is attributed to balancing of the effective coordination around the Mn site. This is now further rationalised by the fact that the binding energy is significantly greater for the MnO_5^{Eq} site - cooperative relaxations (as indicated by Table 6.2) of the surface region have a greater affect on the overall binding energy than those localised mainly to the Mn-O_2 bond (observed in Table 6.1).

Unlike the MnO_5^{Ap} site, the MnO_5^{Eq} site exists only on the (001) surface (from among the surfaces studied in this work). The adsorption of O_2 on (001) surface of orthorhombic ($Pnma$) $LaMnO_3$ has, also unlike the (100) surface, been investigated in the past using DFT with various functionals; GGA, GGA+U (with $U = 4$) and HSE06 [75]. Although there is agreement with the **BE** calculated by GGA, the other

BEs reported are very inconsistent (-0.659, -0.205 and 0.162 eV respectively). This is attributed to the different treatments of electron correlation in the methods, or more specifically, it is suggested that this could be due to overcorrection for correlation in GGA+U and HSE06 [75].

The charge transfer to O_2 on the MnO_5^{Eq} site is larger than on the MnO_5^{Ap} site; 0.61 e can be quantified as 94% of a whole electron in the $LaMnO_3$ bulk. This is noticeably larger than observed for the MnO_5^{Ap} site, suggesting that the MnO_5^{Eq} site is more active with regards to the rate limiting electron transfer step.

The La Bridge Site

As indicated by the increased d(O-O) of the adsorbed O_2 on the (101) surface relative to free O_2, the bridge adsorption mode does indeed involve actual adsorption of O_2 (rather than mere physisorption), evident from the $\mathbf{BE}^{CP(101)}$ of -1.28 eV. It is unusual, however, that the binding is far stronger than the MnO_5^{Eq} site which binds O_2 conventionally. Additionally, the charge transfer to the adsorbed O_2 is also greater than the previously discussed adsorption sites; 0.74 e, which quantifies to 114% of a whole electron in the bulk, indicating that the ORR could proceed despite the unusual La bridge site adsorption.

Since this is the first study to consider the (101) surface of orthorhombic $LaMnO_3$, it is not possible to make a direct comparison of the **BE** for the La Bridge site. Adsorption of O_2 on cubic $LaMnO_3$ surfaces, however, suggests that adsorption on La is possible, though generally weaker than Mn [73]. It may be that adsorption and electron transfer only occurs for La on this particular bridging site due to La being more exposed to the surface than Mn.

The MnO_4^{Eq} Site

Although the (110) surface possesses 3 adsorption sites, as identified in Sec. 6.3, only one of the sites is favoured for adsorbtion; the MnO_4^{Eq} Site. This is further emphasised when the $\mathbf{BE}^{CP(101)}$ is considered for the various forms of adsorption on the MnO_4^{Eq} Site. The $\mathbf{BE}^{CP(101)}$ -2.16 eV observed for the $MnO_5^{Ap} > MnO_4^{Eq-Lateral}$ adsorption is over 10 times greater than that associated with the MnO_5^{Ap} site on the (100) surface, justifying the preference for this adsorption mode. The $MnO_4^{Ap} > MnO_4^{Eq-End-on}$ adsorption mode can be justified in the same way, although the slightly larger $\mathbf{BE}^{CP(101)}$ of -2.43 eV can be attributed to the end-on position of the adsorbed O_2, which is known to be more energetically favourable than lateral adsorption [70].

The lateral mode has a lower **BE** than end-on mainly due to the difference in the interaction of O_2 with the surface atoms and the scale of charge transfer. Although the adsorbed O_2 molecule is stabilised by the lateral mode, this brings both O atoms of O_2 towards the surface, allowing for charge to be more easily transferred to the distal O atom; 1.24 e is accepted by the lateral O_2 compared to 0.70 e for end-on. This additional charge transfer results in some destabilisation of the $LaMnO_3$ surface, since it is cooperatively extracted from the neighbouring lattice atoms.

The lateral adsorption mode accepts charge that can be quantified as 191% of an electron in the bulk, while the end-on mode accepts 108%. This can be approximated as transfer of two and one electrons respectively. The transfer of two electrons is characteristic of O_2 adsorption in its peroxide form (O_2^{2-}), which can readily form the the adsorbed peroxide species OOH^- in the presence of H_2O in order to proceed with the ORR [7]. Although this appears to be an ideal site for the ORR, previous studies indicate that formation of the peroxide species is also fast process following adsorption in the superoxide form [73,108]. The immediate formation of peroxide species, instead, can be a precursor to dissociative adsorption, which is associated with the energetically more costly direct 4 electron pathway (Eq. 1.4) [15,73].

Another concern for adsorption on the MnO_4^{Eq} site is that the **BE**s are too high, resulting in permanent adsorption of O_2 or its by products and thus preventing catalysis. This is an even greater concern for the $MnO_4^{Ap} > MnO_4^{Eq-Bidentate}$ adsorption mode, where the the largest $\mathbf{BE}^{CP(101)}$ of -2.79 eV is observed. The high **BE** can mostly be attributed to the stabilisation of both adsorption sites through the unique bidentate adsorption mode. This effectively cancels out the undercoordination of the 4 O coordinated Mn octahedra and massively stabilises the surface.

The adsorbed O_2 on this site accepts a charge of 1.04 e, which is quantified as 160% of a whole electron in the bulk. This may be considered surprising based on the strong adsorption and is likely to be due to the bidentate O_2 coordination, which mostly restricts the overlap of oxygen orbitals to the electron density in the proximity of the Mn site.

6.5 Summary

In this chapter a detailed study into the structure and surface energetics of the adsorption sites of orthorhombic ($Pnma$) $LaMnO_3$ has been presented. The sites available on the (100), (001), (101) and (110) surfaces are investigated by adsorption of molecular oxygen (O_2) in hybrid-exchange density functional theory calculations.

The binding energies of O_2 indicate that adsorption sites formed through cleavage of apical bonds have a weak interaction with O_2 (the (100) surface), while equatorially cleaved sites bind more strongly (the (001) surface). Adsorption on the (101) surface reveals an unusual and strongly binding La bridge site, while the (110) surface indicates several meta-stable states with the strongest O_2 binding energies.

Charge transfer data suggests that the rate limiting electron transfer step can occur more readily on the equatorially cleaved surfaces. The amount of charge transfer also indicates that O_2 adsorbs as either a superoxide (O_2^-) or peroxide (O_2^{2-}); the peroxide form only occurring when binding energy is particularly high and the O-O bond of O_2 is elongated to 1.46Åor greater.

The electronic and structural characteristics of the adsorption sites and the adsorbed O_2 molecule ultimately provide an understanding of catalytic properties of the studied surfaces towards the ORR, based on the importance of the initial O_2 adsorption and electron transfer step. If the presence and activity of these sites is confirmed by experiment, the surfaces that correlate to optimal catalytic activity can be defined. Knowing which surfaces must be maximised will be a major step towards the optimisation of $LaMnO_3$ crystallite morphology for catalysis of the ORR.

7

Conclusions

In this work, periodic hybrid-exchange density functional calculations were performed in order to understand the origins of the catalytic activity of $LaMnO_3$, working towards its optimisation for the oxygen reduction reaction (ORR) in alkaline fuel cells (AFCs).

Fine characterisation of $LaMnO_3$ catalyst powders is difficult by experiment since the fundamental reaction steps occur on unknown facets at unknown reaction sites. Therefore, by exploiting theoretical methods, $LaMnO_3$ is characterised at the atomic scale in order to provide an understanding of the mechanics behind AFC catalysis. Calculations of the bulk and surface of $LaMnO_3$ are used to predict crystallite morphology, characterise the structure and composition of facets, and subsequently, the nature of surface reaction sites.

The work has four main components; (Ch. 3) establishing the phase stability and thermodynamics of $LaMnO_3$, (Ch. 4) mapping the oxidation state of Mn, (Ch. 5) determining the stability of $LaMnO_3$ surfaces and (Ch. 6) characterising the reaction sites. In the first component the thermodynamics of $LaMnO_3$ and the competing oxides in the La-Mn-O system are found to be more accurately predicted (a mean error of only 1.6% for their Gibbs formation energies) than in any previous study. The high accuracy of these calculations assures us that the systems modelled are a good representation of the actual materials. Additionally, it also indicates that the phase diagram constructed for the La-Mn-O system correctly identifies the chemical potential limits for the stability of the bulk phase, and thus the range of environmental conditions in which the surface are stable.

These chemical potential limits are the particularly relevant to the surfaces of $LaMnO_3$ that are non stoichiometric, since their stability strongly correlates to changes in the chemical potential of the reactive gasses in equilibrium with the crystallite. For

instance, a surface that has an excess of oxygen will be stabilised by a high oxygen chemical potential (oxidising conditions); however, if the high oxygen chemical potential is beyond the limit of $LaMnO_3$ stability identified in the phase diagram, the surface may in fact be unstable.

The second component of this work involved provision of a means by which the presence of $LaMnO_3$ surfaces could be identified by experiment. This was demonstrated by mapping the oxidation states of Mn in its various oxides using simulated electron energy-loss spectroscopy (EELS). The Mn oxides are a useful analogue to the surfaces of $LaMnO_3$ as they contain Mn in multiple oxidation states and bonding environments (this is also expected to be the case for the $LaMnO_3$ surfaces), and are well characterised by EELS.

The simulated EEL spectra show that the oxidation state of Mn in various compounds is characterised by distinct shifts in binding energy for the main peak of the L_3 edge. Additionally, it is shown that both the calculated and measured L_3 edge shapes of Mn are highly sensitive to the local environment of the Mn ion, particularly for Mn^{2+}. By comparison of the calculated L_3 edges of the split $3d$ states (i.e. t_{2g} and e_g) with measured data, it is further possible to identify peak features that convey the type of coordination around the Mn ion.

Using EELS simulations to interpret the measured EELS spectra of Mn ions at the $LaMnO_3$ surface should, therefore, not only identify the oxidation states of Mn ions at surface facets, but also reveal the type of coordination around the Mn ion to give structural verification of the predicted $LaMnO_3$ surface structures at an even finer level.

The third component of this work involves a detailed study of the structure and energetics of the low-index, stoichiometric and non-polar surfaces of $LaMnO_3$. The order of stability for the surfaces is determined to be (low energy) (100)<(101)<(001)<(110) (high energy). Structural analysis of these surfaces provides their first detailed description in literature with the exception of the (110) surface. The equilibrium crystal morphology (Wulff plot) calculated from the formation energies of these surfaces indicates that the surface area contribution of the (100) surface is dominant (32.3%) and that the most widely available adsorption site for the oxygen reduction reaction is an apically cleaved MnO_5 octahedra, making up to 61.7% of the Mn sites.

A detailed analysis of the surface structure reveals that the formation energies of the surfaces are dependent on three factors; 1) the strength and number of cleaved Mn-O bonds (modulated by Jahn-Teller distortion), 2) the compensation of undercoordinated ions at the terminations and 3) the relaxation from the bulk geometry. These factors form the basis for rationalising the surface formation energies of transition metal ox-

ides and are a reference for the scientific community. At the same time, the crystal morphology and predicted adsorption sites provide the groundwork for analysing the catalytic activity of $LaMnO_3$.

The final component of this work involved a detailed characterisation of the structure and energetics of the adsorption sites. By analysing the interaction of the sites with molecular O_2, their reactivity towards the ORR is predicted. The binding energies of O_2 indicate that adsorption sites formed through cleavage of apical bonds have a weak interaction with O_2 (the (100) surface), while equatorially cleaved sites bind more strongly (the (001) surface). Adsorption on the (101) surface reveals an unusual and strongly binding La bridge site, while the (110) surface indicates several meta-stable states with the strongest O_2 binding energies.

Analysis of charge transfer suggests that the rate limiting electron transfer step can occur more readily on the equatorially cleaved surfaces. The amount of charge transfer also indicates that O_2 adsorbs as either a superoxide (O_2^-) or peroxide (O_2^{2-}); the peroxide form only occurring when binding energy is particularly high and the O-O bond of O_2 is elongated to 1.46 Å or greater.

The electronic and structural characteristics of the adsorption sites and the adsorbed O_2 molecule ultimately provide an understanding of catalytic properties of the studied surfaces towards the ORR, based on the importance of the initial O_2 adsorption and electron transfer step. If the presence and activity of these sites is confirmed by experiment, the surfaces that correlate to optimal catalytic activity can be defined. Knowing which surfaces must be maximised will be a major step towards the optimisation of $LaMnO_3$ crystallite morphology for catalysis of the ORR.

The significance of each of the above components can be summarised as follows in terms of their contribution toward understanding and optimising $LaMnO_3$ as a catalyst for the ORR.

- The initial thermodynamic work was a necessary step to establish the accuracy of the adopted methodology and for future study of non-stoichiometric surfaces and equilibrium crystal morphologies.

- The oxidation state mapping of Mn presents a valuable tool for determining the presence of surfaces (that have been predicted) on actual $LaMnO_3$ crystallites.

- The existence of multiple previously unidentified surfaces is detailed and rationale for their stability is provided. Each of the surfaces present unique adsorption sites on which the ORR can be investigated.

- Characterisation of the adsorption sites indicates the likely reactivity of the surfaces previously identified, and reveals the structural features required for weak/strong adsorption. Experimental confirmation of the activity of these sites will provide a reference for the structural features required at the surface for optimal catalysis.

In conclusion, the investigation so far has significantly increased the basic understanding of $LaMnO_3$ in the AFC environment and has established much of the required groundwork to address the challenging goal of optimising its catalytic activity. In future work, the computational study can be expanded to include non-stoichiometric and polar (reconstructed) surfaces, after which the equilibrium crystal morphology of $LaMnO_3$ will be dynamic and vary depending on the chemical potentials (environment). Following experimental confirmation of the presence and reactivity of the predicted adsorption sites, it should then be possible to design a synthesis route for morphologically optimised $LaMnO_3$ catalyst powders, where the surfaces containing the most active sites are maximised.

Appendix A

Basis Sets

The basis sets used in this work are given in the Tables below. The exponents, α_j, and the coefficients, c_j, of the Gaussian type orbitals (GTOs) below were found to be optimal for the series of oxides studied in Ch. 3

A.1 Oxygen

The basis set for O atoms was denoted as a 8-411d(1) contraction, corresponding to one s, three sp and one d shells.

Shell-type	α_j	c_j	
1s		s	
	8020	0.00108	
	1338	0.00804	
	255.4	0.05324	
	69.22	0.1681	
	23.90	0.3581	
	9.264	0.3855	
	3.851	0.1468	
	1.212	0.0728	
2sp		s	p
	49.43	-0.00883	0.00958
	10.47	-0.0915	0.0696
	3.235	-0.0402	0.2065
	1.217	0.379	0.347
3sp		s	p
	0.4567	1.0	1.0
4sp		s	p
	0.1843	1.0	1.0
3d		d	
	0.6	1.0	

A.2 Manganese

The basis set for Mn atoms was denoted as an 86-411d(41) contraction, corresponding to one s, four sp and two d shells.

Shell-type	α_j	c_j	
$1s$		s	
	292601.0	0.000227	
	42265.0	0.0019	
	8947.29	0.0111	
	2330.32	0.0501	
	702.047	0.1705	
	242.907	0.3691	
	94.955	0.4035	
	39.5777	0.1437	
$2sp$		s	p
	732.14	-0.0053	0.0086
	175.551	-0.0673	0.0612
	58.5093	-0.1293	0.2135
	23.129	0.2535	0.4018
	9.7536	0.6345	0.4012
	3.4545	0.2714	0.2222
$3sp$		s	p
	38.389	0.0157	-0.0311
	15.4367	-0.2535	-0.0969
	6.1781	-0.8648	0.2563
	2.8235	0.9337	1.6552
$4sp$		s	p
	1.2086	1.0	1.0
$5sp$		s	p
	0.4986	1.0	1.0
$3d$		d	
	22.5929	0.0708	
	6.1674	0.3044	
	2.0638	0.5469	
	0.7401	0.5102	
$4d$		d	
	0.249	1.0	

A.3 Lanthanum

The basis set of the valence electrons for the La atoms was denoted as a 411p(411)d(311) contraction corresponding to one *s*, three *sp* and one *d* shells. The core electrons are described by a pseudopotential designed by Dolg *et al.* and adapted for usage in CRYSTAL09 [199, 200].

Shell-type	α_j	c_j
5*s*		*s*
	6.3238774	-0.086529557
	3.7199279	0.61078587
	2.1881929	-1.0956970
	0.51247125	0.80819274
6*s*		*s*
	0.27290268	1.0
7*s*		*s*
	0.15	1.0
5*p*		*p*
	6.5427184	-0.0094583546
	3.8486579	0.11792823
	2.2639164	-0.33256926
	0.63548358	0.49511706
6*p*		*p*
	0.31351355	1.0
7*p*		*p*
	0.15	1.0
5*d*		*d*
	3.1281946	0.017184007
	1.7836083	-0.10742130
	1.0491814	0.090724362
6*d*		*d*
	0.41219354	1.0
7*d*		*d*
	0.15	1.0

Appendix B

Thermodynamic Equations

B.1 The Surface Formation Energy of a Non-stoichiometric Surface

$$E_s = \frac{1}{2A}\left(E_{slab} - N_{La}\mu_{La} - N_{Mn}\mu_{Mn} - N_{O_2}\mu_{O_2}\right) \tag{B.1}$$

$$E_s = \frac{1}{2A}\left(E_{slab} - N_{La}\left(G^{bulk}_{LaMnO_3} - \mu_{Mn} - \frac{3}{2}\mu_{O_2}\right) - N_{Mn}\mu_{Mn} - N_{O_2}\mu_{O_2}\right) \tag{B.2}$$

$$E_s = \frac{1}{2A}\left(E_{slab} - N_{La}G^{bulk}_{LaMnO_3} + N_{La}\mu_{Mn} + N_{La}\frac{3}{2}\mu_{O_2} - N_{Mn}\mu_{Mn} - N_{O_2}\mu_{O_2}\right) \tag{B.3}$$

$$E_s = \frac{1}{2A}\left(E_{slab} - N_{La}G^{bulk}_{LaMnO_3} + \mu_{Mn}(N_{La} - N_{Mn}) + \mu_{O_2}(\frac{3}{2}N_{La} - N_{O_2})\right) \tag{B.4}$$

B.2 Change of variable for NS surface

$$E_s 2A - \mu^0_{Mn}(N_{La} - N_{Mn}) - \mu^0_{O_2}(\frac{3}{2}N_{La} - N_{O_2}) = \tag{B.5}$$

$$E_{slab} - N_{La}G^{bulk}_{LaMnO_3} + \Delta\mu_{Mn}(N_{La} - N_{Mn}) + \Delta\mu_{O_2}(\frac{3}{2}N_{La} - N_{O_2})$$

$$E_s = \frac{1}{2A}\Bigg(E_{slab} - N_{La}G^{bulk}_{LaMnO_3} + \Delta\mu_{Mn}(N_{La} - N_{Mn}) + \Delta\mu_{O_2}(\frac{3}{2}N_{La} - N_{O_2}) \quad \text{(B.6)}$$

$$+\mu^0_{Mn}(N_{La} - N_{Mn}) + \mu^0_{O_2}(\frac{3}{2}N_{La} - N_{O_2})\Bigg)$$

B.3 The Inequalities Plotted in the La-Mn-O Phase Diagram

Firstly, the standard chemical potential of the elements are substracted by both sides of previous equations.

$$2\mu_{La} + \frac{3}{2}\mu_{O_2} - 2\mu^0_{La} - \frac{3}{2}\mu^0_{O_2} \leq \mu^{bulk}_{La_2O_3} - 2\mu^0_{La} - \frac{3}{2}\mu^0_{O_2} \quad \text{(B.7)}$$

$$\mu_{Mn} + \frac{1}{2}\mu_{O_2} - \mu^0_{Mn} - \frac{1}{2}\mu^0_{O_2} \leq \mu^{bulk}_{MnO} - \mu^0_{Mn} - \frac{1}{2}\mu^0_{O_2} \quad \text{(B.8)}$$

$$\mu_{Mn} + \mu_{O_2} - \mu^0_{Mn} - \mu^0_{O_2} \leq \mu^{bulk}_{MnO2} - \mu^0_{Mn} - \mu^0_{O_2} \quad \text{(B.9)}$$

$$2\mu_{Mn} + \frac{3}{2}\mu_{O_2} - 2\mu^0_{Mn} - \frac{3}{2}\mu^0_{O_2} \leq \mu^{bulk}_{Mn_2O_3} - 2\mu^0_{Mn} - \frac{3}{2}\mu^0_{O_2} \quad \text{(B.10)}$$

$$3\mu_{Mn} + 2\mu_{O_2} - 3\mu^0_{Mn} - 2\mu^0_{O_2} \leq \mu^{bulk}_{Mn_3O_4} - 3\mu^0_{Mn} - 2\mu^0_{O_2} \quad \text{(B.11)}$$

Now, when the following change of variable is performed in Eq.B.7 to Eq.B.11

$$\Delta\mu_{La} = \mu_{La} - \mu^0_{La}$$

$$\Delta\mu_{Mn} = \mu_{Mn} - \mu^0_{Mn}$$

$$\Delta\mu_{O_2} = \mu_{O_2} - \mu^0_{O_2}$$

the previous equations become as follows:

$$\Delta\mu_{Mn} + \frac{1}{2}\Delta\mu_{O_2} = \mu^{bulk}_{MnO} - \mu^0_{Mn} - \frac{1}{2}\mu^0_{O_2} \quad \text{(B.12)}$$

$$\Delta\mu_{Mn} + \Delta\mu_{O_2} = \mu^{bulk}_{MnO_2} - \mu^0_{Mn} - \mu^0_{O_2} \quad \text{(B.13)}$$

$$2\Delta\mu_{Mn} + \frac{3}{2}\Delta\mu_{O_2} = \mu^{bulk}_{Mn_2O_3} - 2\mu^0_{Mn} - \frac{3}{2}\mu^0_{O_2} \tag{B.14}$$

$$3\Delta\mu_{Mn} + 2\Delta\mu_{O_2} = \mu^{bulk}_{Mn_3O_4} - 3\mu^0_{Mn} - 2\mu^0_{O_2} \tag{B.15}$$

$$2\Delta\mu_{La} + \frac{3}{2}\Delta\mu_{O_2} = \mu^{bulk}_{La_2O_3} - 2\mu^0_{La} - \frac{3}{2}\mu^0_{O_2} \tag{B.16}$$

Applying the inequailty condition and the formation energy relationship as described in section 3.2 gives:

$$\Delta\mu_{Mn} + \frac{1}{2}\Delta\mu_{O_2} \geq \Delta G^o_{fMnO} \tag{B.17}$$

$$\Delta\mu_{Mn} + \Delta\mu_{O_2} \geq \Delta G^o_{fMnO_2} \tag{B.18}$$

$$2\Delta\mu_{Mn} + \frac{3}{2}\Delta\mu_{O_2} \geq \Delta G^o_{fMn_2O_3} \tag{B.19}$$

$$3\Delta\mu_{Mn} + 2\Delta\mu_{O_2} \geq \Delta G^o_{fMn_3O_4} \tag{B.20}$$

$$2\Delta\mu_{La} + \frac{3}{2}\Delta\mu_{O_2} \geq \Delta G^o_{fLa_2O_3} \tag{B.21}$$

B.4 Inequality for Lanthanum Oxide on the Mn-O_2 axis

For the case of plotting La_2O_3 on the Mn-O_2 axis:

$$2\Delta\mu_{La} + \frac{3}{2}\Delta\mu_{O_2} \geq \Delta G^o_{fLa_2O_3}$$

$$2(\Delta G^o_{fLaMnO_3} - \Delta\mu_{Mn} - \frac{3}{2}\Delta\mu_{O_2}) + \frac{3}{2}\Delta\mu_{O_2} \geq \Delta G^o_{fLa_2O_3}$$

$$2\Delta G^o_{fLaMnO_3} - 2\Delta\mu_{Mn} - 3\Delta\mu_{O_2} + \frac{3}{2}\Delta\mu_{O_2} \geq \Delta G^o_{fLa_2O_3}$$

$$2\Delta G^o_{fLaMnO_3} - 2\Delta\mu_{Mn} - \frac{3}{2}\Delta\mu_{O_2} \geq \Delta G^o_{fLa_2O_3}$$

$$2\Delta G^{o}_{fLaMnO_3} - \Delta G^{o}_{fLa_2O_3} \geq 2\Delta\mu_{Mn} + \frac{3}{2}\Delta\mu_{O_2} \tag{B.22}$$

B.5 Phase Diagram Line Equations

In order to plot the two-dimentional phase diagram, $\Delta\mu_{Mn}$ is expressed as a function of $\Delta\mu_{O_2}$ as follows:

$$\Delta\mu_{Mn} \leq (\mu^{bulk}_{LaMnO_3} - \mu^{0}_{La} - \mu^{0}_{Mn} - \frac{3}{2}\mu^{0}_{O_2}) - \frac{1}{2}(\mu^{bulk}_{La_2O_3} - 2\mu^{0}_{La} - \frac{3}{2}\mu^{0}_{O_2}) - \frac{3}{4}\Delta\mu_{O_2} \tag{B.23}$$

$$\Delta\mu_{Mn} \leq -\frac{1}{2}\Delta\mu_{O_2} + (\mu^{bulk}_{MnO} - \mu^{0}_{Mn} - \frac{1}{2}\mu^{0}_{O_2}) \tag{B.24}$$

$$\Delta\mu_{Mn} \leq -\frac{1}{2}\Delta\mu_{O_2} + \frac{1}{2}(\mu^{bulk}_{MnO_2} - \mu^{0}_{Mn} - \mu^{0}_{O_2}) \tag{B.25}$$

$$\Delta\mu_{Mn} \leq -\frac{3}{4}\Delta\mu_{O_2} + \frac{1}{2}(\mu^{bulk}_{Mn_2O_3} - 2\mu^{0}_{Mn} - \frac{3}{2}\mu^{0}_{O_2}) \tag{B.26}$$

$$\Delta\mu_{Mn} \leq -\frac{2}{3}\Delta\mu_{O_2} + \frac{1}{3}(\mu^{bulk}_{Mn_3O_4} - 3\mu^{0}_{Mn} - 2\mu^{0}_{O_2}) \tag{B.27}$$

B.6 Oxygen Chemical Potential by Oxide Method

The combination of formulas for standard Gibss energy of formation for the series of Mn oxides that remain after removing the equivalencies are listed below (the combinations can be seen on the left hand side, the right hand side has already been simplified):

$$\Delta G^{0}_{fMnO_2} - \Delta G^{0}_{fMnO} = \mu^{bulk}_{MnO_2} - \mu^{bulk}_{MnO} - \frac{1}{2}\mu^{0}_{O_2} \tag{B.28}$$

$$\Delta G^{0}_{fMn_2O_3} - 2\Delta G^{0}_{fMnO} = \mu^{bulk}_{Mn_2O_3} - 2\mu^{bulk}_{MnO} - \frac{1}{2}\mu^{0}_{O_2} \tag{B.29}$$

$$\Delta G^{0}_{fMn_3O_4} - 3\Delta G^{0}_{fMnO} = \mu^{bulk}_{Mn_3O_4} - 3\mu^{bulk}_{MnO} - \frac{1}{2}\mu^{0}_{O_2} \tag{B.30}$$

$$\Delta G^{0}_{fMn_2O_3} - 2\Delta G^{0}_{fMnO_2} = \mu^{bulk}_{Mn_2O_3} - 2\mu^{bulk}_{MnO_2} + \frac{1}{2}\mu^{0}_{O_2} \tag{B.31}$$

$$\Delta G^0_{fMn_3O_4} - 3\Delta G^0_{fMnO_2} = \mu^{bulk}_{Mn_3O_4} - 3\mu^{bulk}_{MnO_2} + \mu^0_{O_2} \tag{B.32}$$

$$2\Delta G^0_{fMn_3O_4} - 3\Delta G^0_{fMn_2O_3} = 2\mu^{bulk}_{Mn_3O_4} - 3\mu^{bulk}_{Mn_2O_3} + \frac{1}{2}\mu^0_{O_2} \tag{B.33}$$

Upon isolating the chemical potential of oxygen from these combinations, the following are given:

$$\mu^0_{O_2} = 2(\mu^{bulk}_{MnO_2} - \mu^{bulk}_{MnO} - \Delta G^0_{fMnO_2} + \Delta G^0_{fMnO}) \tag{B.34}$$

$$\mu^0_{O_2} = 2(\mu^{bulk}_{Mn_2O_3} - 2\mu^{bulk}_{MnO} - \Delta G^0_{fMn_2O_3} + 2\Delta G^0_{fMnO}) \tag{B.35}$$

$$\mu^0_{O_2} = 2(\mu^{bulk}_{Mn_3O_4} - 3\mu^{bulk}_{MnO}\Delta G^0_{fMn_3O_4} - 3\Delta G^0_{fMnO}) \tag{B.36}$$

$$\mu^0_{O_2} = 2(\Delta G^0_{fMn_2O_3} - 2\Delta G^0_{fMnO_2} - \mu^{bulk}_{Mn_2O_3} + 2\mu^{bulk}_{MnO_2}) \tag{B.37}$$

$$\mu^0_{O_2} = \Delta G^0_{fMn_3O_4} - 3\Delta G^0_{fMnO_2} - \mu^{bulk}_{Mn_3O_4} + 3\mu^{bulk}_{MnO_2} \tag{B.38}$$

$$\mu^0_{O_2} = 2(2\Delta G^0_{fMn_3O_4} - 3\Delta G^0_{fMn_2O_3} - 2\mu^{bulk}_{Mn_3O_4} + 3\mu^{bulk}_{Mn_2O_3}) \tag{B.39}$$

Appendix C

Permissions

Below are copies of documents giving permission to reproduce third party content in this thesis; for Figs. 1.5, 1.7, 4.2 and 4.4 respectively.

RightsLink

Copyright Clearance Center

Thank You For Your Order!

Dear Mr. Ehsan Ahmad,

Thank you for placing your order through Copyright Clearance Center's RightsLink service. Nature Publishing Group has partnered with RightsLink to license its content. This notice is a confirmation that your order was successful.

Your order details and publisher terms and conditions are available by clicking the link below:
http://s100.copyright.com/CustomerAdmin/PLF.jsp?ref=364785a5-90bb-4f0a-8650-f633a189f9bf

Order Details
Licensee: Ehsan A Ahmad
License Date: Jul 15, 2013
License Number: 3190301451377
Publication: Nature Chemistry
Title: Design principles for oxygen-reduction activity on perovskite oxide catalysts for fuel cells and metal-air batteries
Type Of Use: reuse in a thesis/dissertation
Order Reference: suntivich
Total: 0.00 GBP

To access your account, please visit https://myaccount.copyright.com.

Please note: Online payments are charged immediately after order confirmation; invoices are issued daily and are payable immediately upon receipt.

To ensure we are continuously improving our services, please take a moment to complete our customer satisfaction survey.

B.1:v4.2

+1-877-622-5543 / Tel: +1-978-646-2777

RightsLink

Copyright Clearance Center

Thank You For Your Order!

Dear Mr. Ehsan Ahmad,

Thank you for placing your order through Copyright Clearance Center's RightsLink service. Elsevier has partnered with RightsLink to license its content. This notice is a confirmation that your order was successful.

Your order details and publisher terms and conditions are available by clicking the link below:
http://s100.copyright.com/CustomerAdmin/PLF.jsp?ref=2e736ec3-557c-4a9c-93ad-7e1caa7a0e66

Order Details
Licensee: Ehsan A Ahmad
License Date: Aug 26, 2013
License Number: 3216700656733
Publication: Surface Science
Title:
Type Of Use: reuse in a thesis/dissertation
Order Reference: co2/o2 ads isotherm
Total: 0.00 USD

To access your account, please visit https://myaccount.copyright.com.

Please note: Online payments are charged immediately after order confirmation; invoices are issued daily and are payable immediately upon receipt.

To ensure we are continuously improving our services, please take a moment to complete our customer satisfaction survey.

B.1:v4.2

+1-877-622-5543 / Tel: +1-978-646-2777

AMERICAN PHYSICAL SOCIETY
One Physics Ellipse, College Park, MD 20740 · http://www.aps.org

September 25, 2013

Dr. Ehsan Ahmad
Department of Chemistry
Imperial College of Science, Technology and Medicine
South Kensington
London
SW7 2AZ

Ref # 24631

Thank you for your permission request dated Sept. 22, 2013. We are pleased to grant you a non-exclusive, non-transferable permission, English rights, limited to **print and electronic format**, provided you meet the criteria outlined below. Permission is for a one-time use and does not include permission for future editions, updates, databases, translations, or any other matters. Permission must be sought for each additional use. This permission does not include the right to modify APS material.

Please print the required copyright credit line on the first page that the material appears: "Reprinted (abstract/excerpt/figure) with permission from [FULL REFERENCE CITATION] as follows: authors names, journal title, volume number, page number and year of publication. Copyright (YEAR) by the American Physical Society.

The following language must appear somewhere on the website: "Readers may view, browse, and/or download material for temporary copying purposes only, provided these uses are for noncommercial personal purposes. Except as provided by law, this material may not be further reproduced, distributed, transmitted, modified, adapted, performed, displayed, published, or sold in whole or part, without prior written permission from the American Physical Society."

Provide a hyperlink from the reprinted APS material (the hyperlink may be embedded in the copyright credit line). APS's link manager technology makes it convenient and easy to provide links to individual articles in APS journals. For information, see: http://link.aps.org/.

You must also obtain permission from at least one of the authors for each separate work, if you haven't done so already. The author's name and address can be found on the first page of the published Article.

Use of the APS material must not imply any endorsement by the American Physical Society.

Permission is granted for use of the following APS material only:

- Fig. 2, Phys. Rev. Lett. 107, 107602 (2011)

Permission is limited to the single title specified of the publication as follows:
A thesis entitled "Density functional theory study of LaMnO3 and its competing oxides: An insight into a prospective alkaline fuel cell cathode" to be published by Imperial College.

If you have any questions, please refer to the Copyright FAQ at: http://publish.aps.org/copyrightFAQ.html or send an email to assocpub@aps.org.

Sincerely,

Jamie L. Casey
Circulation and Fulfillment Assistant

RightsLink

Copyright Clearance Center

Thank You For Your Order!

Dear Mr. Ehsan Ahmad,

Thank you for placing your order through Copyright Clearance Center's RightsLink service. Elsevier has partnered with RightsLink to license its content. This notice is a confirmation that your order was successful.

Your order details and publisher terms and conditions are available by clicking the link below:
http://s100.copyright.com/CustomerAdmin/PLF.jsp?ref=3b4eec7b-e0dc-4cd4-875f-a3b081436197

Order Details
Licensee: Ehsan A Ahmad
License Date: Oct 21, 2013
License Number: 3253870400942
Publication: Ultramicroscopy
Title: Electron-beam-induced reduction of Mnin manganese oxides as revealed by parallel EELS
Type Of Use: reuse in a thesis/dissertation
Order Reference: garviefig
Total: 0.00 EUR

To access your account, please visit https://myaccount.copyright.com.

Please note: Online payments are charged immediately after order confirmation; invoices are issued daily and are payable immediately upon receipt.

To ensure we are continuously improving our services, please take a moment to complete our customer satisfaction survey.

B.1:v4.2

+1-877-622-5543 / Tel: +1-978-646-2777

Bibliography

[1] M.-F. Hsu, L.-J. Wu, J.-M. Wu, Y.-H. Shiu, and K.-F. Lin, *Electrochemical and Solid-State Letters* **9** A193–A195 2006.

[2] S. J. Skinner, *International Journal of Inorganic Materials* **3** 113 – 121 2001.

[3] S. Tao, J. Irvine, and J. Kilner, *Advanced Materials* **17** 1734–1737 2005.

[4] M. Hayashi, H. Uemura, K. Shimanoe, N. Miura, and N. Yamazoe, *Journal of The Electrochemical Society* **151** A158–A163 2004.

[5] K. Miyazaki, N. Sugimura, K. Matsuoka, Y. Iriyama, T. Abe, M. Matsuoka, and Z. Ogumi, *Journal of Power Sources* **178** 683 – 686 2008.

[6] F. Bidault, D. Brett, P. Middleton, and N. Brandon, *Journal of Power Sources* **187** 39 – 48 2009.

[7] J. Suntivich, H. A. Gasteiger, N. Yabuuchi, H. Nakanishi, J. B. Goodenough, and Y. Shao-Horn, *Nature Chemistry* **3** 546–550 2011.

[8] J. St-Pierre and D. P. Wilkinson, *AIChE Journal* **47** 1482–1486 2001.

[9] D. L. Trimm and Z. I. nsan, *Catalysis Reviews* **43** 31–84 2001.

[10] J. H. Park, S. Kim, and A. J. Bard, *Nano Letters* **6** 24–28 2006.

[11] M. K. Debe, *Nature* **486** 43–51 2012.

[12] J. R. Varcoe, R. C. T. Slade, and E. Lam How Yee, *Chem. Commun.* **0** 1428–1429 2006.

[13] J. R. Varcoe, R. C. T. Slade, E. Lam How Yee, S. D. Poynton, D. J. Driscoll, and D. C. Apperley, *Chemistry of Materials* **19** 2686–2693 2007.

[14] G. Couture, A. Alaaeddine, F. Boschet, and B. Ameduri, *Progress in Polymer Science* **36** 1521 – 1557 2011.

[15] E. Yeager, *Electrochimica Acta* **29** 1527 – 1537 1984.

[16] B. Blizanac, P. Ross, and N. Markovic, *Electrochimica Acta* **52** 2264 – 2271 2007.

[17] M. Bursell, M. Pirjamali, and Y. Kiros, *Electrochimica Acta* **47** 1651 – 1660 2002.

[18] D. W. Murphy, S. Sunshine, R. B. van Dover, R. J. Cava, B. Batlogg, S. M. Zahurak, and L. F. Schneemeyer, *Phys. Rev. Lett.* **58** 1888–1890 1987.

[19] N. Bonanos, K. Knight, and B. Ellis, *Solid State Ionics* **79** 161 – 170 1995.

[20] J.-S. Zhou, W. Archibald, and J. B. Goodenough, *Journal of Catalysis* **381** 770 – 772 1996.

[21] T. Ishihara, *Perovskite Oxide for Solid Oxide Fuel Cells*, 2009.

[22] L. da Conceicao, C. R. Silva, N. F. Ribeiro, and M. M. Souza, *Materials Characterization* **60** 1417 – 1423 2009.

[23] L. Ge, Z. Zhu, Z. Shao, S. Wang, and S. Liu, *Ceramics International* **35** 3201 – 3206 2009.

[24] W. D. K. D Brandon, *Microstructural Characterization of Materials*, 2008.

[25] E. O. Wollan and W. C. Koehler, *Phys. Rev.* **100** 545–563 1955.

[26] R. O'Hayre, *Fuel Cell Fundamentals*, 2005.

[27] J. Hafner, C. Wolverton, and G. Ceder, *MRS Bulletin* **31** 659–668 2006.

[28] R. A. Evarestov, E. A. Kotomin, Y. A. Mastrikov, D. Gryaznov, E. Heifets, and J. Maier, *Phys. Rev. B* **72** 214411 2005.

[29] D. Kramer and G. Ceder, *Chemistry of Materials* **21** 3799–3809 2009.

[30] D. B. Meadowcroft, *Nature* **226** 847–848 1970.

[31] J. Rodríguez-Carvajal, M. Hennion, F. Moussa, A. H. Moudden, L. Pinsard, and A. Revcolevschi, *Phys. Rev. B* **57** R3189–R3192 1998.

[32] A. Wold and R. J. Arnott, *Journal of Physics and Chemistry of Solids* **9** 176 – 180 1959.

[33] P. Norby, I. G. K. Andersen, E. K. Andersen, and N. H. Andersen, *Journal of Solid State Chemistry* **119** 191 – 196 1995.

[34] J. B. . Goodenough and J.-S. Zhou, *Journal of Materials Chemistry* **17** 2394–2405 2007.

[35] J. Volger, *Physica* **20** 49 – 66 1954.

[36] S. Jin, T. H. Tiefel, M. McCormack, R. A. Fastnacht, R. Ramesh, and L. H. Chen, *Science* **264** 413–415 1994.

[37] A.-M. Haghiri-Gosnet and J.-P. Renard, *Journal of Physics D: Applied Physics* **36** R127 2003.

[38] J. A. M. V. Roosmalen, E. H. P. Cordfunke, R. B. Helmholdt, and H. W. Zandbergen, *Journal of Solid State Chemistry* **110** 100 – 105 1994.

[39] H. Satoh, M. Takagi, K. ichi Kinukawa, and N. Kamegashira, *Thermochimica Acta* **299** 123 – 126 1997.

[40] C. Oliva and L. Forni, *Catalysis Communications* **1** 5 – 8 2000.

[41] D. S. Jung, S. K. Hong, and Y. C. Kang, *Journal of the Ceramic Society of Japan* **116** 141–145 2008.

[42] Y. Shimizu and T. Murata, *Journal of the American Ceramic Society* **80** 2702–2704 1997.

[43] K. Kitayama, *Journal of Solid State Chemistry* **153** 336 – 341 2000.

[44] B. F. Woodfield, M. L. Wilson, and J. M. Byers, *Phys. Rev. Lett.* **78** 3201–3204 1997.

[45] K. T. Jacob and M. Attaluri, *J. Mater. Chem.* **13** 934–942 2003.

[46] L. B. Pankratz, *U. S. Bureau of Mines Bulletin* **672** 509 1982.

[47] J. Suntivich, H. A. Gasteiger, N. Yabuuchi, and Y. Shao-Horn, *J. Electrochem. Soc.* **157** B1263–B1268 2010.

[48] J. Sunarso, A. A. J. Torriero, W. Zhou, P. C. Howlett, and M. Forsyth, *The Journal of Physical Chemistry C* **116** 5827–5834 2012.

[49] T. Poux, F. Napolskiy, T. Dintzer, G. Kranguven, S. Y. Istomin, G. Tsirlina, E. Antipov, and E. Savinova, *Catalysis Today* **189** 83 – 92 2012.

[50] A. Rolla, A. Sadkowski, J. Wild, and P. Zoltowski, *Journal of Power Sources* **5** 189 – 196 1980.

[51] M. Sato, M. Ohta, and M. Sakaguchi, *Electrochimica Acta* **35** 945 – 950 1990.

[52] R. Hammami, H. Batis, and C. Minot, *Surface Science* **603** 3057 – 3067 2009.

[53] J. M. D. Tascn and L. G. Tejuca, *J. Chem. Soc., Faraday Trans. 1* **77** 591–602 1981.

[54] K. J. May, C. E. Carlton, K. A. Stoerzinger, M. Risch, J. Suntivich, Y.-L. Lee, A. Grimaud, and Y. Shao-Horn, *The Journal of Physical Chemistry Letters* **3** 3264–3270 2012.

[55] J. Suntivich, K. J. May, H. A. Gasteiger, J. B. Goodenough, and Y. Shao-Horn, *Science* **334** 1383–1385 2011.

[56] K. A. Stoerzinger, M. Risch, J. Suntivich, W. M. Lu, J. Zhou, M. D. Biegalski, H. M. Christen, Ariando, T. Venkatesan, and Y. Shao-Horn, *Energy Environ. Sci.* **6** 1582–1588 2013.

[57] D. D. Sarma, N. Shanthi, S. R. Barman, N. Hamada, H. Sawada, and K. Terakura, *Phys. Rev. Lett.* **75** 1126–1129 1995.

[58] S. Satpathy, Z. S. Popović, and F. R. Vukajlović, *Phys. Rev. Lett.* **76** 960–963 1996.

[59] W. E. Pickett and D. J. Singh, *Phys. Rev. B* **53** 1146–1160 1996.

[60] T. Saitoh, A. E. Bocquet, T. Mizokawa, H. Namatame, A. Fujimori, M. Abbate, Y. Takeda, and M. Takano, *Phys. Rev. B* **51** 13942–13951 1995.

[61] Y.-S. Su, T. A. Kaplan, S. D. Mahanti, and J. F. Harrison, *Phys. Rev. B* **61** 1324–1329 2000.

[62] M. Nicastro and C. H. Patterson, *Phys. Rev. B* **65** 205111 2002.

[63] D. Muñoz, N. M. Harrison, and F. Illas, *Phys. Rev. B* **69** 085115 2004.

[64] W. Y. Hu, M. C. Qian, Q. Q. Zheng, H. Q. Lin, and H. K. Wong, *Phys. Rev. B* **61** 1223–1231 2000.

[65] F. Cora, M. Alfredsson, G. Mallia, D. S. Middlemiss, W. C. Mackrodt, R. Dovesi, and R. Orlando, *The Performance of Hybrid Density Functionals in Solid State Chemistry*, *Structure & Bonding*, volume 113, 2004.

[66] N. N. Kovaleva, A. V. Boris, C. Bernhard, A. Kulakov, A. Pimenov, A. M. Balbashov, G. Khaliullin, and B. Keimer, *Phys. Rev. Lett.* **93** 147204 2004.

[67] R. A. Evarestov, E. A. Kotomin, D. Fuks, J. Felsteiner, and J. Maier, *Applied Surface Science* **238** 457–463 2004.

[68] S. Piskunov, E. Heifets, T. Jacob, E. A. Kotomin, D. E. Ellis, and E. Spohr, *Phys. Rev. B* **78** 121406 2008.

[69] E. A. Kotomin, Y. Mastrikov, E. Heifets, R. Merkle, J. Fleig, J. Maier, A. Gordon, and J. Felsteiner, *ECS Transactions* **13** 301–306 2008.

[70] E. A. Kotomin, Y. Mastrikov, E. Heifets, and J. Maier, *Phys. Chem. Chem. Phys.* **10** 4644–4649 2008.

[71] Y. Mastrikov, E. Heifets, E. Kotomin, and J. Maier, *Surface Science* **603** 326 – 335 2009.

[72] S. Piskunov, E. Spohr, T. Jacob, E. A. Kotomin, and D. E. Ellis, *Phys. Rev. B* **76** 012410 2007.

[73] Y. Choi, D. S. Mebane, M. C. Lin, and M. Liu, *Chemistry of Materials* **19** 1690–1699 2007.

[74] Y. Choi, M. E. Lynch, M. C. Lin, and M. Liu, *The Journal of Physical Chemistry C* **113** 7290–7297 2009.

[75] Y. Wang and H.-P. Cheng, *The Journal of Physical Chemistry C* **117** 2106–2112 2013.

[76] Y.-L. Lee, J. Kleis, J. Rossmeisl, Y. Shao-Horn, and D. Morgan, *Energy Environ. Sci.* **4** 3966–3970 2011.

[77] A. Vojvodic and J. K. Nrskov, *Science* **334** 1355–1356 2011.

[78] F. Tang, M. Huang, W. Lu, and W. Yu, *Surface Science* **603** 949 – 954 2009.

[79] http://cci.lbl.gov/.

[80] http://www.cryst.ehu.es/.

[81] M. Sunding, K. Hadidi, S. Diplas, O. Lvvik, T. Norby, and A. Gunns, *Journal of Electron Spectroscopy and Related Phenomena* **184** 399 – 409 2011.

[82] N. Imanaka, T. Masui, and Y. Kato, *Journal of Solid State Chemistry* **178** 395 – 398 2005.

[83] V. Bannikov, I. Shein, and A. Ivanovskii, *Journal of Superconductivity and Novel Magnetism* **24** 1693–1696 2011.

[84] B. F. Woodfield, J. L. Shapiro, R. Stevens, J. Boerio-Goates, and M. L. Wilson, *Phys. Rev. B* **60** 7335–7340 1999.

[85] R. Tackett, G. Lawes, B. C. Melot, M. Grossman, E. S. Toberer, and R. Seshadri, *Phys. Rev. B* **76** 024409 2007.

[86] T. Suzuki and T. Katsufuji, *Journal of Physics: Conference Series* **150** 042195 2009.

[87] G. B. Jensen and O. V. Nielsen, *Journal of Physics C: Solid State Physics* **7** 409 1974.

[88] R. Norrestam, *Acta Chemica Scandinavica* **21** 2871–2884 1967.

[89] R. W. Grant, S. Geller, J. A. Cape, and G. P. Espinosa, *Phys. Rev.* **175** 686–695 1968.

[90] S. Geller, *Acta Crystallographica Section B* **27** 821–828 1971.

[91] M. Regulski, R. Przenioslo, I. Sosnowska, D. Hohlwein, and R. Schneider, *Journal of Alloys and Compounds* **362** 236 – 240 2004.

[92] S. Mukherjee, A. K. Pal, S. Bhattacharya, and J. Raittila, *Phys. Rev. B* **74** 104413 2006.

[93] J. E. Post and P. J. Heaney, *American Mineralogist* **89** 969–975 2004.

[94] P. R. B. Shirley Turner, *Nature* **304** 143–146 1983.

[95] A. Yoshimori, *Journal of the Physical Society of Japan* **14** 807–821 1959.

[96] Y. P. W. Bowden, F. Wang and C. Grey, 2000.

[97] M. W. Chase, *NIST-JANAF Thermochemical Tables (fourth ed.)*, 1998.

[98] I. Bahrin, *Thermochemical Data of Pure Substances (Third Edition)*, 1995.

[99] CRC, *Handbook of Chemistry & Physics 91st Edition*, 2010.

[100] A. N. Sophie Fritsch, *Journal of the American Ceramic Society* **79** 1761–1768 1996.

[101] S. L. Brock, N. Duan, Z. R. Tian, O. Giraldo, H. Zhou, and S. L. Suib, *Chemistry of Materials* **10** 2619–2628 1998.

[102] C. S. Brooks, *Journal of Catalysis* **8** 272 – 282 1967.

[103] M. Zaki, M. Hasan, L. Pasupulety, and K. Kumari, *Thermochimica Acta* **311** 97 – 103 1998.

[104] K. Ramesh, L. Chen, F. Chen, Y. Liu, Z. Wang, and Y.-F. Han, *Catalysis Today* **131** 477 – 482 2008.

[105] T. Yamashita and A. Vannice, *Journal of Catalysis* **161** 254 – 262 1996.

[106] T. Yamashita and A. Vannice, *Journal of Catalysis* **163** 158 – 168 1996.

[107] L. Mao, D. Zhang, T. Sotomura, K. Nakatsu, N. Koshiba, and T. Ohsaka, *Electrochimica Acta* **48** 1015 – 1021 2003.

[108] F. H. Lima, M. L. Calegaro, and E. A. Ticianelli, *Journal of Electroanalytical Chemistry* **590** 152 – 160 2006.

[109] M. D. Towler, N. L. Allan, N. M. Harrison, V. R. Saunders, W. C. Mackrodt, and E. Aprà, *Phys. Rev. B* **50** 5041–5054 1994.

[110] C. Franchini, V. Bayer, R. Podloucky, J. Paier, and G. Kresse, *Phys. Rev. B* **72** 045132 2005.

[111] C. Franchini, R. Podloucky, J. Paier, M. Marsman, and G. Kresse, *Phys. Rev. B* **75** 195128 2007.

[112] S. Massidda, A. Continenza, M. Posternak, and A. Baldereschi, *Phys. Rev. Lett.* **74** 2323–2326 1995.

[113] X. Feng, *Phys. Rev. B* **69** 155107 2004.

[114] D. Balachandran, D. Morgan, G. Ceder, and A. van de Walle, *Journal of Solid State Chemistry* **173** 462 – 475 2003.

[115] Ramandeep, T. Maitra, and T. Nautiyal, *AIP Conference Proceedings* **1447** 835–836 2012.

[116] Q. L. Chen and W. Y. Li, *Advanced Materials Research* **479** 81–87 2012.

[117] E. Cockayne, I. Levin, H. Wu, and A. Llobet, *Phys. Rev. B* **87** 184413 2013.

[118] M. Born and R. Oppenheimer, *Annalen der Physik* **389** 457–484 1927.

[119] N. M. Harrison, *NATO Advanced Study Institute Notes on DFT*, http://www.ch.ic.ac.uk/harrison/Teaching/teaching.html.

[120] K. Raghavachari and J. B. Anderson, *The Journal of Physical Chemistry* **100** 12960–12973 1996.

[121] C. Pisani, L. Maschio, S. Casassa, M. Halo, M. Schtz, and D. Usvyat, *Journal of Computational Chemistry* **29** 2113–2124 2008.

[122] S. Casassa, C. Zicovich-Wilson, and C. Pisani, *Theoretical Chemistry Accounts* **116** 726–733 2006.

[123] P. Hohenberg and W. Kohn, *Phys. Rev.* **136** B864–B871 1964.

[124] M. Levy, *Proceedings of the National Academy of Sciences of the United States of America* **76** pp. 6062–6065 1979.

[125] W. Kohn and L. J. Sham, *Phys. Rev.* **140** A1133–A1138 1965.

[126] F. Jensen, *Introduction to Computational Chemsitry*, 2007.

[127] E. Fermi, *Z. Phys* **48** 73 1928.

[128] P. A. M. Dirac, *Proc. Camb. Phil. Soc.* **26** 376 1930.

[129] C. Lee, W. Yang, and R. G. Parr, *Phys. Rev. B* **37** 785–789 1988.

[130] C. Adamo, M. Ernzerhof, and G. E. Scuseria, *The Journal of Chemical Physics* **112** 2643–2649 2000.

[131] S. Kurth, J. P. Perdew, and P. Blaha, *International journal of quantum chemistry* **75** 889–909 1999.

[132] R. P. A. Savin, F. Colonna, *International Journal of Quantum Chemistry* **93** 166–190 2003.

[133] A. D. Becke, *J. Chem. Phys.* **98** 5648 1993.

[134] R. Dovesi, B. Civalleri, R. Orlando, C. Roetti, and V. R. Saunders, *ChemInform* (2005).

[135] D. Pettifor, *Bonding and structure of molecules and solids*, 1995.

[136] H. J. Monkhorst and J. D. Pack, *Phys. Rev. B* **13** 5188–5192 1976.

[137] J. D. Pack and H. J. Monkhorst, *Phys. Rev. B* **16** 1748–1749 1977.

[138] R. Dovesi, V. R. Saunders, C. Roetti, R. Orlando, C. M. Zicovich-Wilson, F. Pascale, B. Civalleri, K. Doll, N. Harrison, I. J. Bush, P. D'Arco, and M. Llunell, CRYSTAL09 *User's Manual*, Torino, 2010.

[139] B. Civalleri, P. D'Arco, R. Orlando, V. Saunders, and R. Dovesi, *Chemical Physics Letters* **348** 131 – 138 2001.

[140] W. T. V. H. W. Press, S. A. Teukolsky and P. B. Flannery, *Numerical Recipes*, 1992.

[141] C. J. Cramer, *Essentials of Computational Chemistry: Theories and Models*, 2004.

[142] K. Terakura, T. Oguchi, A. R. Williams, and J. Kübler, *Phys. Rev. B* **30** 4734–4747 1984.

[143] Z.-X. Shen, R. S. List, D. S. Dessau, B. O. Wells, O. Jepsen, A. J. Arko, R. Barttlet, C. K. Shih, F. Parmigiani, J. C. Huang, and P. A. P. Lindberg, *Phys. Rev. B* **44** 3604–3626 1991.

[144] H. Sawada, Y. Morikawa, K. Terakura, and N. Hamada, *Phys. Rev. B* **56** 12154–12160 1997.

[145] G. Trimarchi and N. Binggeli, *Phys. Rev. B* **71** 035101 2005.

[146] V. I. Anisimov, J. Zaanen, and O. K. Andersen, *Phys. Rev. B* **44** 943–954 1991.

[147] V. I. Anisimov, I. V. Solovyev, M. A. Korotin, M. T. Czyżyk, and G. A. Sawatzky, *Phys. Rev. B* **48** 16929–16934 1993.

[148] J. Muscat, A. Wander, and N. Harrison, *Chemical Physics Letters* **342** 397 – 401 2001.

[149] G. Mallia and N. M. Harrison, *Phys. Rev. B* **75** 165201 2007.

[150] N. C. Wilson, S. P. Russo, J. Muscat, and N. M. Harrison, *Phys. Rev. B* **72** 024110 2005.

[151] G. C. De Fusco, B. Montanari, and N. M. Harrison, *Phys. Rev. B* **82** 220404 2010.

[152] G. C. De Fusco, L. Pisani, B. Montanari, and N. M. Harrison, *Phys. Rev. B* **79** 085201 2009.

[153] L. Liborio, G. Mallia, and N. Harrison, *Phys. Rev. B* **79** 245133 2009.

[154] C. L. Bailey, L. Liborio, G. Mallia, S. Tomić, and N. M. Harrison, *Phys. Rev. B* **81** 205214 2010.

[155] http://www.crystal.unito.it/Basis_Sets/Ptable.html.

[156] G. Mallia, R. Orlando, M. Llunell, and R. Dovesi. On the performance of various Hamiltonians in the study of crystalline compounds. The case of open shell systems. in *Computational Materials Science*, edited by C.R.A. Catlow and E.A. Kotomin, *NATO SCIENCE SERIES, III: Computer and Systems Sciences*, volume 187, 102–121. 2003.

[157] C. Pisani, R. Dovesi, and C. Roetti, *Hartree-Fock ab initio Treatment of Crystalline Systems*, *Lecture Notes in Chemistry*, volume 48, Springer Verlag, 1988.

[158] L. M. Liborio, C. L. Bailey, G. Mallia, S. Tomic, and N. M. Harrison, *Journal of Applied Physics* **109** 023519 2011.

[159] K. Johnston, M. R. Castell, A. T. Paxton, and M. W. Finnis, *Phys. Rev. B* **70** 085415 2004.

[160] http://webbook.nist.gov/chemistry/.

[161] http://cds.dl.ac.uk/icsd/.

[162] B. C. Hauback, H. Fjellvag, and N. Sakai, *Journal of Solid State Chemistry* **124** 43 – 51 1996.

[163] N. Hirosaki, S. Ogata, and C. Kocer, *Journal of Alloys and Compounds* **351** 31 – 34 2003.

[164] V. Baron, J. Gutzmer, H. Rundlof, and R. Tellgren, *American Mineralogist* **83** 786–793 1998.

[165] D. Taylor, *Transactions and Journal of the British Ceramic Society* **83** 5–9 1984.

[166] A. Bolzan, C. Fong, B. Kennedy, and C. Howard, *Australian Journal of Chemistry* **46** 939–944 1993.

[167] X.-F. Wang, Q.-X. Li, X.-Y. Chu, and F. S-H., *Chemical Journal of Chinese Universities* **28** 821–823 2007.

[168] C. R. Ross, D. C. Rubie, and E. Paris, *American Mineralogist* **75** 1249–1252 1990.

[169] E. A. Kotomin, R. A. Evarestov, Y. A. Mastrikov, and J. Maier, *Phys. Chem. Chem. Phys.* **7** 2346–2350 2005.

[170] E. S. Bozin, M. Schmidt, A. J. DeConinck, G. Paglia, J. F. Mitchell, T. Chatterji, P. G. Radaelli, T. Proffen, and S. J. L. Billinge, *Phys. Rev. Lett.* **98** 137203 2007.

[171] A. M. L. Lopes, V. S. Amaral, J. G. Correia, and J. P. Arajo, *Journal of Physics: Condensed Matter* **25** 385602 2013.

[172] M. Mikami and S. Nakamura, *Journal of Alloys and Compounds* **408-412** 687 – 692 2006.

[173] W. L. Roth, *Phys. Rev.* **110** 1333–1341 1958.

[174] H. Shaked, J. Faber, and R. L. Hitterman, *Phys. Rev. B* **38** 11901–11903 1988.

[175] L. Wang, T. Maxisch, and G. Ceder, *Phys. Rev. B* **73** 195107 2006.

[176] G. Vovk, X. Chen, and C. A. Mims, *The Journal of Physical Chemistry B* **109** 2445–2454 2005.

[177] I. Fullarton, J.-P. Jacobs, H. Benthem, J. Kilner, H. Brongersma, P. Scanlon, and B. Steele, *Ionics* **1** 51–58 1995.

[178] H. W. Nesbitt and D. Banerjee, *American Mineralogist* **83** 305–315 1998.

[179] R. F. Egerton, *Electron energy-loss spectroscopy in the electron microscope*, 1996.

[180] K. Kimoto, T. Asaka, T. Nagai, M. Saito, Y. Matsui, and K.Ishizuka, *Nature* **450** 702–704 2007.

[181] L. A. J. Garvie and A. J. Craven, *Physics and Chemistry of Minerals* **21** 191–206 1994.

[182] R. F. Egerton, *Electron energy-loss spectroscopy in the electron microscope (3rd Edition)*, 2011.

[183] D. B. Williams and C. B. Carter, *Transmission Electron Microscopy (2nd Edition)*, 2009.

[184] R. F. Egerton, *Reports on Progress in Physics* **72** 016502 2009.

[185] R. Egerton and M. Whelan, *Journal of Electron Spectroscopy and Related Phenomena* **3** 232 – 236 1974.

[186] R. D. Leapman, L. A. Grunes, and P. L. Fejes, *Phys. Rev. B* **26** 614–635 1982.

[187] H. Tan, S. Turner, E. Yücelen, J. Verbeeck, and G. Van Tendeloo, *Phys. Rev. Lett.* **107** 107602 2011.

[188] M. Haruta, H. Kurata, H. Komatsu, Y. Shimakawa, and S. Isoda, *Phys. Rev. B* **80** 165123 2009.

[189] R. Evarestov, E. Kotomin, E. Heifets, J. Maier, and G. Borstel, *Solid State Communications* **127** 367 – 371 2003.

[190] E. A. Ahmad, L. Liborio, D. Kramer, G. Mallia, A. R. Kucernak, and N. M. Harrison, *Phys. Rev. B* **84** 085137 2011.

[191] P. W. Tasker, *Journal of Physics C: Solid State Physics* **12** 4977 1979.

[192] L. Wang, F. Zhou, Y. S. Meng, and G. Ceder, *Phys. Rev. B* **76** 165435 2007.

[193] M. J. Akhtar, C. R. A. Catlow, B. Slater, A. M. Walker, and S. M. Woodley, *Chemistry of Materials* **18** 1552–1560 2006.

[194] G. Pilania and R. Ramprasad, *Surface Science* **604** 1889 – 1893 2010.

[195] Y. A. Mastrikov, R. Merkle, E. Heifets, E. A. Kotomin, and J. Maier, *The Journal of Physical Chemistry C* **114** 3017–3027 2010.

[196] J. Scaranto, G. Mallia, and N. Harrison, *Computational Materials Science* **50** 2080 – 2086 2011.

[197] D. A. Outka, J. Stöhr, W. Jark, P. Stevens, J. Solomon, and R. J. Madix, *Phys. Rev. B* **35** 4119–4122 1987.

[198] I. Papai, A. Goursot, F. Fajula, D. Plee, and J. Weber, *The Journal of Physical Chemistry* **99** 12925–12932 1995.

[199] M. Dolg, H. Stoll, A. Savin, and H. Preuss, *Theoretica chimica acta* **75** 173–194 1989.

[200] J. Yang and M. Dolg, *Theoretical Chemistry Accounts* **113** 212–224 2005.